Journal of Materials Chemistry A

ROYAL SOCIETY OF CHEMISTRY

REVIEW

View Article Online
View Journal | View Issue

Cite this: J. Mater. Chem. A, 2025, 13, 14540

$ZnMn_2O_4$ applications in batteries and supercapacitors: a comprehensive review

Joel Kingston Ramesh,†[a] Sasan Rostami,†[b] Jayaprakasan Rajesh,[a] R. Margrate Bhackiyavathi Princess,[d] Radhika Govindaraju,[e] Jinho Kim,[c] Rainer Adelung,[fg] Palanisamy Rajkumar *[c] and Mozaffar Abdollahifar *[fg]

Received 30th January 2025
Accepted 31st March 2025

DOI: 10.1039/d5ta00815h

rsc.li/materials-a

$ZnMn_2O_4$ (ZMO) has emerged as a promising material for energy storage applications due to its high theoretical capacity, low cost, and environmental friendliness. This review comprehensively explores the structure, synthesis methods, and performance of ZMO in various energy storage systems, including supercapacitors and batteries such as lithium-ion (LIBs), sodium-ion (SIBs) and zinc-ion (ZIBs) batteries, due to its exceptional electrochemical properties. The influence of various synthesis techniques on the structural and morphological features of ZMO, which directly impact its electrochemical performance will be discussed. The review also delves into the charge storage mechanism of ZMO in supercapacitors, examining the effects of morphology, composites, and doping on its performance. Additionally, the use of ZMO as an anode material for LIBs and SIBs and its potential as a cathode material in ZIBs are discussed. The review also addresses key challenges and proposes strategies to enhance performance including incorporating conductive materials, synergizing with other materials, and doping. An outlook on the current challenges, future directions, and potential pathways for performance enhancement is also presented.

[a]Department of Chemistry, Indian Institute of Technology Madras, Chennai, 600036, Tamil Nadu, India
[b]Department of Physics and Energy Engineering, Amirkabir University of Technology (Tehran Polytechnique), Tehran, Iran
[c]Department of Mechanical Engineering, Yeungnam University, Gyeongsan-si, Gyeongbukdo 38541, Republic of Korea. E-mail: rajkumar@yu.ac.kr
[d]Department of Chemistry, Lady Doak College, Tallakulam, Madurai, 625002, Tamil Nadu, India
[e]Department of Physics, Rajalakshmi Institute of Technology, Chennai, 600 124, Tamil Nadu, India
[f]Chair for Functional Nanomaterials, Department of Materials Science, Faculty of Engineering, Kiel University, Kaiserstr. 2, 24143, Kiel, Germany. E-mail: moza@tf.uni-kiel.de
[g]Kiel Nano, Surface and Interface Science (KiNSIS), Kiel University, Germany
† These authors have contributed equally to this work.

Joel Kingston Ramesh

Joel Kingston Ramesh completed his Bachelor of Science in Physics and Master of Science in Physics from The American College, Tamil Nadu, India. Joel is serving as a Project Associate at the Indian Institute of Technology Madras (IIT-Madras), where he contributed to research in materials science. He also worked as a Research Assistant at the Photovoltaic Laboratory at SSN Institute, Chennai (in 2021), and participated in a Summer Internship at the IIT-Madras (in 2019). His scientific research focuses on solar cells and energy storage materials, particularly Li-ion, Na-ion, Li–sulfur and solid-state batteries.

Sasan Rostami

Sasan Rostami received his Master's degree in Condensed Matter Physics from Amirkabir University of Technology in 2020, focusing on fabricating electrodes based on two-dimensional materials for lithium-ion batteries. After graduation, he continued his research at the same university, specializing in polymer-based solid-state batteries. In 2023, he began collaborating with Kiel University (Germany) on some joint publications. His research interests include synthesizing and modifying various materials and optimizing their structures, morphologies, and properties for use in battery anodes and cathodes.

1 Introduction

Electrochemical energy storage (EES) systems,[1] namely, batteries, supercapacitors, and fuel cells have emerged as the primary means of storing energy.[2] Electrode performance is vital for these systems, making electrode materials a key focus of global research and development initiatives.[3] Researchers are actively exploring new electrode materials with key characteristics, including low production cost, improved specific capacity, extended cycle life and environmentally benign properties. Pursuing such materials is fueled by the desire to enhance energy storage technologies, serve the increasing demand for efficient and sustainable energy storage, and pave the way for the widespread implementation of renewable energy sources. Achieving breakthroughs in electrode materials holds tremendous potential for revolutionizing energy storage and advancing various applications, ranging from portable electronics to electric vehicles and grid-scale energy storage.[4,5] By addressing the limitations of current electrode materials, researchers aim to usher in a new era of energy storage that is economically viable, environmentally friendly, and capable of meeting the evolving needs of our energy-intensive society.[6,7]

EES systems utilize a range of electrode materials, including transition metal oxides (TMOs),[8] carbon-based materials, conducting polymers, metal sulfides/selenides, metal nitrides/phosphides, metal–organic frameworks (MOFs), and hybrid composite materials. Among these materials, TMOs have garnered significant interest due to their diverse and tunable properties, contributing to the development of high-performance energy storage devices.[9,10] Composed of transition metal cations and oxygen anions, these compounds exhibit a wide range of structural motifs, electronic configurations, and redox activities; making them versatile candidates for various applications.[11] TMOs often exhibit variable oxidation states, allowing for redox reactions and high catalytic activity. This property makes them ideal catalysts in various chemical reactions, where they can enhance reaction rates.[12–15] Moreover, the redox behavior and stability of TMOs make them excellent candidates for energy storage and conversion devices, such as lithium (Li)-ion batteries (LIBs)[10] and fuel cells. To highlight

Radhika Govindaraju

Dr Govindaraju Radhika is an Assistant Professor at the Department of Physics at Rajalakshmi Institute of Technology, India. She earned her PhD from Alagappa University, Karaikudi, India. Her research focuses on creating electrocatalysts for advanced energy storage devices, such as batteries and supercapacitors.

Palanisamy Rajkumar

Dr Palanisamy Rajkumar is currently working as an International Research Professor in the Department of Mechanical Engineering, Yeungnam University, South Korea. He acquired his PhD degree at Alagappa University, Karaikudi, India. He has completed his post-doctoral research at Kunsan National University, South Korea. His research interests are focused on development of electrocatalysts for next-generation energy storage devices particularly batteries, supercapacitors, fuel cells and water splitting devices.

Rainer Adelung

Dr Rainer Adelung is a Professor and holder of the Chair of Functional Nanomaterials at the Department of Materials Science at the Faculty of Engineering at Kiel University (Germany). He specializes in various nanostructures, mainly in the synthesis and design of porous materials. Applications range from energy technology such as batteries and supercapacitors to sensor devices, antiviral agents and advanced adhesion technology in engineering.

Mozaffar Abdollahifar

Dr Mozaffar Abdollahifar received his doctorate in chemical engineering, focused on energy storage materials, from National Taiwan University (NTU) in 2018. Before becoming a battery group leader at Kiel University (Germany), he worked as a scientist for several years at NTU and then at the Battery LabFactory Braunschweig (BLB, TU Braunschweig, Germany). He is interested in developing supercapacitors and battery materials for Li, Na and sulfur chemistries, anode-free batteries, and electrode engineering, as well as recycling end-of-life batteries.

a few examples, lithium cobalt oxide ($LiCoO_2$) serves as the most successful commercial cathode material in LIBs, providing high energy density and exceptional cycling stability.[16] Similarly, TMOs such as MnO_2, Mn_2O_3, and Mn_3O_4 are well-studied materials for supercapacitors.[17–19] However, the main issues preventing the commercialization of supercapacitors based on Mn are their low electrical conductivity (10^{-7}–10^{-8} S cm^{-2}), poor cyclability, and inferior rate capability.[19] By creating composites of manganese-based materials with various conducting materials such as graphene, activated carbon, carbon nanotubes, and polymers, numerous attempts have been made to overcome these problems. Apart from this, substituting one manganese (Mn) cation from a tetrahedral or octahedral location in the Mn oxide spinel structures with other metal cations can further improve the electrochemical performance of Mn_3O_4.[20] These Mn oxide substituted metal cations may function as a buffer matrix to absorb strain and stress brought on by prolonged cycling. Therefore, it will be advantageous to substitute one Mn in Mn_3O_4 with cations such as nickel (Ni), zinc (Zn), cobalt (Co), *etc*.[21]

Mn-based ternary metal oxides (*e.g.*, $ZnMn_2O_4$ (ZMO), $LiMn_2O_4$, $NiMn_2O_4$, $MnCo_2O_4$, $CuMn_2O_4$, and $FeMn_2O_4$) have attracted significant attention for diverse applications such as catalysis, gas sensing, photodetection, and energy storage.[20,22–24] For supercapacitors, mixed TMOs are particularly promising due to their enhanced redox activity and high electrical conductivity which contribute to superior capacitive performance.[25] According to the Shanghai Metals Market (SMM), by December 2024, the market prices for Mn, Zn, Ni, and Co will be approximately 2000, 2800, 9000, and 60 000 USD per metric ton, respectively.[26] It is clear that Mn and Zn are much more affordable than Co and Ni. From a cost-performance perspective, the combination of Mn and Zn in ZMO presents a compelling option for supercapacitor and battery applications. Building upon its cost-effectiveness and promising properties, among various ternary metal oxides, ZMO stands out due to its unique combination of high theoretical capacity, structural stability, and cost-effectiveness. Its spinel crystal structure provides robust mechanical integrity, which helps accommodate volume expansion during cycling,[20] a critical challenge for many transition metal oxides. Additionally, ZMO benefits from the synergistic redox activity of both Mn and Zn; offering enhanced charge storage capability.[25] In LIBs and sodium-ion batteries (SIBs), ZMO operates through a conversion–intercalation mechanism, enabling high lithium/sodium storage capacity. As a Zn-ion battery (ZIB) cathode, its ability to reversibly intercalate Zn^{2+} ions in aqueous electrolytes ensures stable cycling performance. Furthermore, ZMO exhibits relatively high electronic conductivity compared to other manganese-based oxides, facilitating improved charge transport.[25] These attributes make ZMO a highly versatile electrode material, capable of delivering high capacity, long cycle life, and improved rate performance across multiple energy storage systems.

Given the promising attributes of ZMO highlighted above, this review will explore the structure, properties, synthesis methods, and energy storage, including supercapacitor and battery applications of ZMO in detail. In the supercapacitor section, we will discuss the charge storage mechanism, and effects of morphology, composites and doping on ZMO performance, while in the battery section, we will focus on ZMO as an anode material for LIBs and SIBs, as well as a cathode material in ZIBs. Finally, the review will present an outlook on the current challenges and future directions in the field of ZMO-based electrode materials for energy storage applications. We will discuss potential pathways for performance enhancement, integration with other materials, and the future prospects of ZMO in emerging energy storage technologies.

2 Evolution of ZMO synthesis and applications in energy storage

Fig. 1 provides a comprehensive overview of the historical development and current trends in ZMO synthesis and its applications in energy storage devices. This figure is divided into three sections: Fig. 1(a) highlights the rapid growth in ZMO research in recent years, as evidenced by the increasing number of publications (from a few papers before 2000 to over 1100 published reports in 2023 and 2024 alone). Fig. 1(b) illustrates the current distribution of ZMO applications, highlighting the dominance of LIBs which account for 55% of the total. Supercapacitors and SIBs represent smaller portions, with 16% and a minor share, respectively. Fig. 1(c) traces the evolution of ZMO synthesis methods, starting from the first report in 1965.[27] It showcases the rise of hydrothermal (HT) synthesis as the primary method (Fig. 1(d)) by 2007.[28] Alongside this, the applications of ZMO expanded from fundamental structural studies to photocatalysis,[29] semiconductors,[30] and ultimately energy storage.[31,32]

Fig. 1(d) details the specific synthesis techniques, highlighting the major contribution of HT, which is employed for various applications. Furthermore, recent research explores ZMO with anionic S-doping and oxygen vacancies for ZIBs.[33,34] Overall, Fig. 1 demonstrates a clear trend towards diversification in both ZMO synthesis methods and applications. Although LIBs remain the dominant application, the growing interest in utilizing ZMO for supercapacitors, SIBs and ZIBs is driving the development of new synthesis approaches and material modifications to optimize performance in these emerging energy storage technologies.

The diverse applications of ZMO in energy storage stem from its unique structural characteristics, which are explored in the following section.

3 ZMO structure and properties

Spinel compounds, represented by the general formula AB_2O_4, form a notable category of mixed metal oxides. In these structures, the divalent cation (A^{2+}) can include Mn, Ni, Zn, Co, iron (Fe), or similar elements, while the trivalent cation (B^{3+}) often includes Mn, Co, Fe, or others. A spinel unit cell consists of 56 ions: 24 metal ions and 32 oxygen ions, corresponding to a general formula of $A_8B_{16}O_{32}$, which is equivalent to 8 AB_2O_4

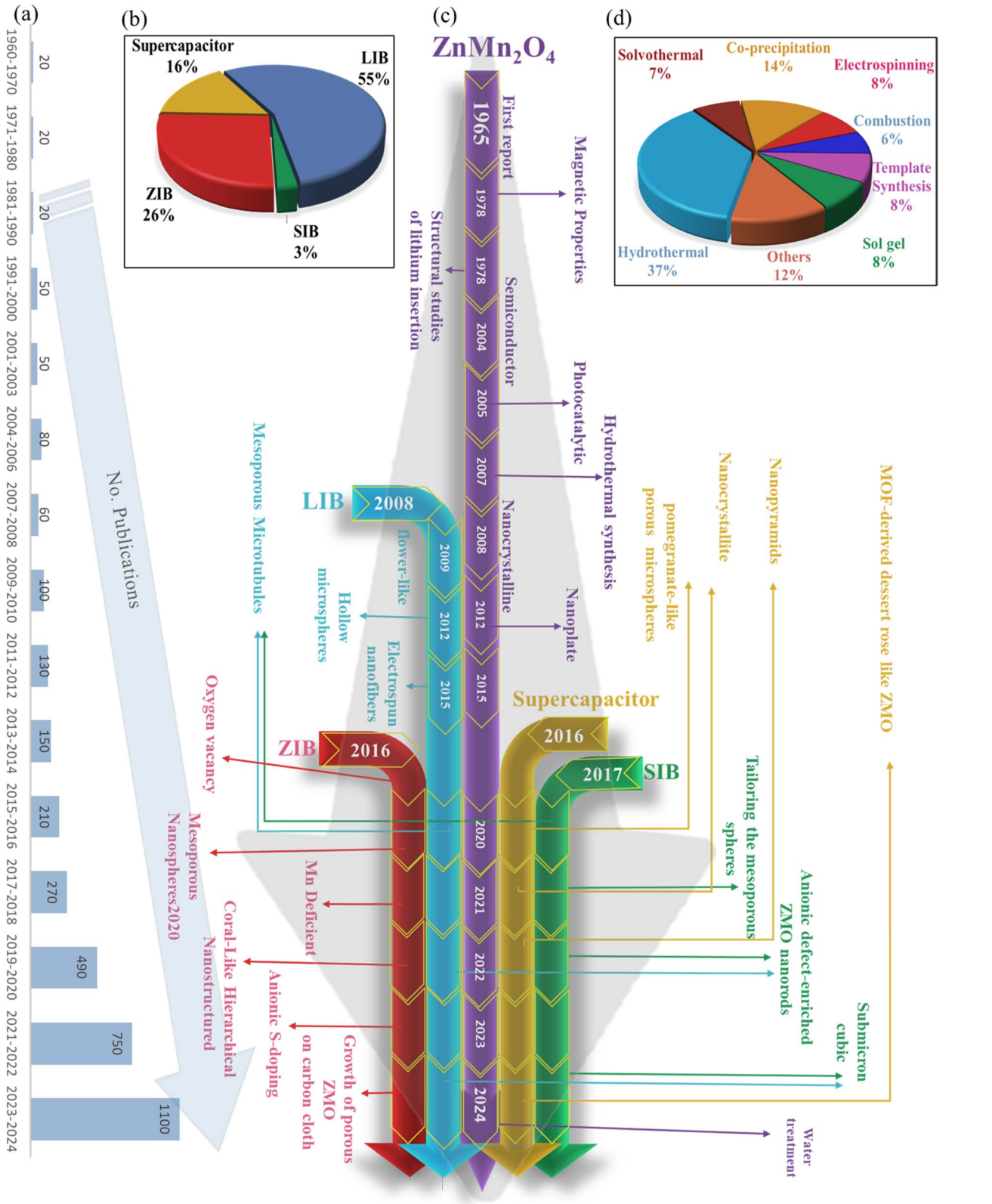

Fig. 1 Overview of ZMO research and applications: (a) number of publications *vs.* year from 1960 to 2024 (obtained from Google Scholar using the keyword "$ZnMn_2O_4$"); (b) distribution of ZMO applications across energy storage systems, showing the percentage contribution to supercapacitors, lithium-ion batteries (LIBs), sodium-ion batteries (SIBs), and zinc-ion batteries (ZIBs); (c) timeline highlighting the development of ZMO, including advancements in morphological evolution, and applications in energy storage devices; (d) distribution of synthesis methods for ZMO, illustrating the percentage contribution of various techniques to its fabrication.

units. Spinel ZMO possesses a tetragonal structure with the bivalent Zn^{2+} occupying the tetrahedral sites and the trivalent Mn^{3+} occupying the octahedral sites in the spinel structure with space group $I4_1/amd$ (Fig. 2(a)). Oxygen ions create two types of vacancies in the structure: a tetrahedral vacancy with a [ZnO_4] unit and an octahedral vacancy with a [MnO_6] unit; the octahedrally coordinated Mn^{3+} exhibits a strong Jahn–Teller distortion effect.

The degree of inversion in ZMO spinel structures can vary, described by using the formula $(Zn_{1-x}Mn_x)(Zn_xMn_{2-x})O_4$, where $0 \leq x \leq 1$. This parameter (x) defines the extent of inversion, which depends on factors such as particle size, morphology, and synthesis method. In a normal spinel, Zn occupies the A sites and Mn occupies the B sites, while in an inverse spinel, half of the Mn occupies the A sites and all Zn resides in the octahedral B sites. The partially inversed structure is described using the x-parameter to indicate the occupancy of

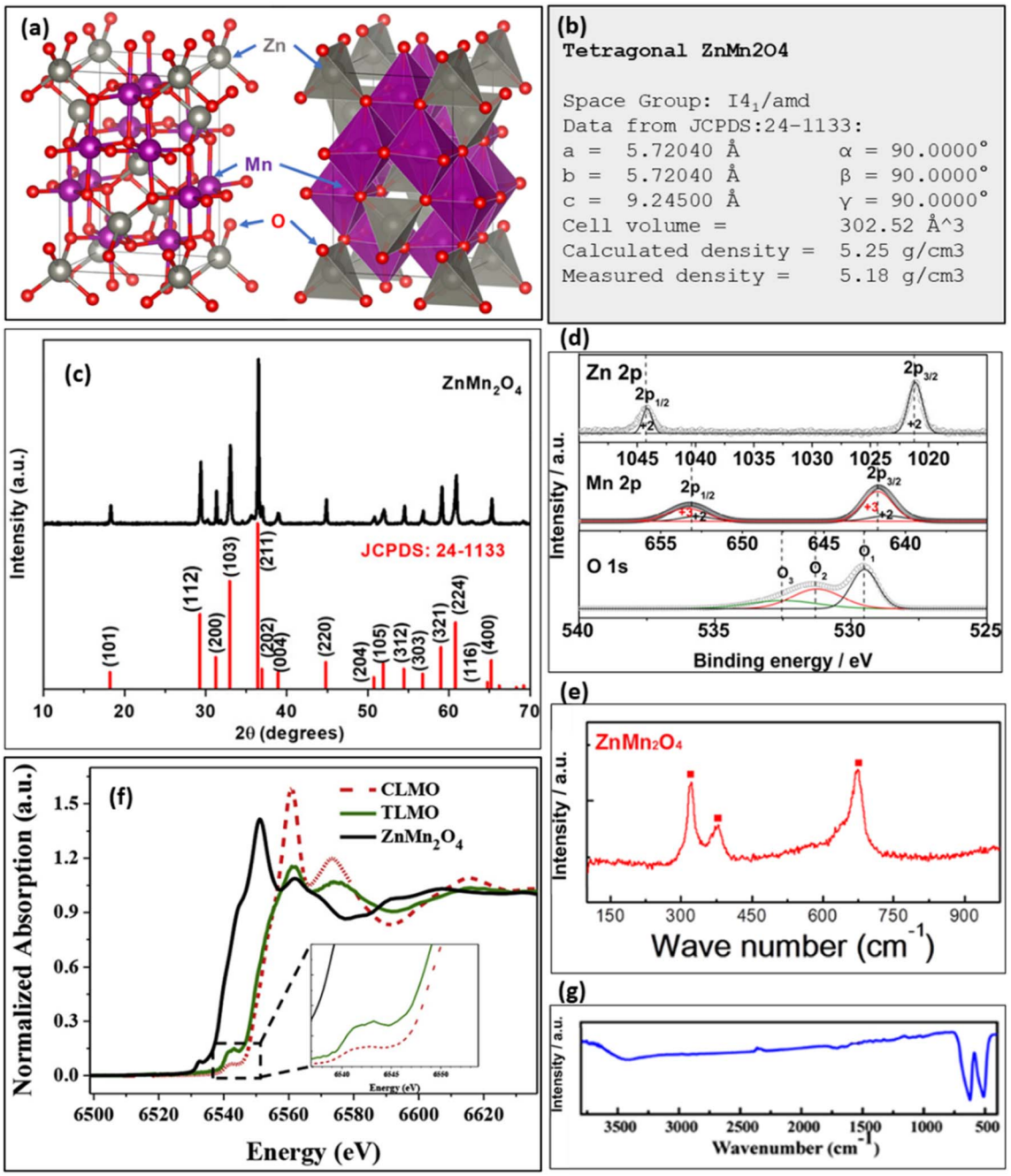

Fig. 2 ZMO characterization: (a) illustration of the crystal structure, (b) crystal structure details based on JCPDS No. 24-1133, and (c) XRD pattern with the reference JCPDS No. 24-1133. Reproduced from ref. 35 with permission from ACS, copyright 2023. (d) XPS spectra showing Zn 2p, Mn 2p, and O 1s peaks. Reproduced from ref. 36 with permission from ACS, copyright 2020. (e) Raman spectrum. Reproduced from ref. 37 with permission from ACS, copyright 2013. (f) XANES spectra of ZMO and $LiMn_2O_4$ with tetragonal (TLMO) and cubic (CLMO) structures. Reproduced from ref. 38 with permission from Elsevier, copyright 2019. (g) FTIR spectra. Reproduced from ref. 39 with permission from ACS, copyright 2018.

Mn on A sites.[40–42] Three JCPDS reference patterns are typically used for ZMO (24-1133, 01-071-2499, and 01-077-0470). As a reference, the data for JCPDS No. 24-1133 are shown in Fig. 2(b). Additionally, characteristic tetragonal ZMO features are illustrated with XRD patterns, XPS, FTIR, XANES, and Raman spectra in Fig. 2(c–g). Spinel ZMO exhibits intriguing electronic, magnetic, and transport properties, making it highly suitable for a wide range of applications, particularly in sensors and energy storage. These compelling properties have drawn considerable attention from the scientific community.

The interaction between metal cations in ZMO influences the electronic structure and redox behavior, enabling multiple redox reactions and increased charge storage capacity when used as an energy storage material.[43] Furthermore, the lattice distortion induced by incorporating two metal ions modifies ion diffusion pathways and influences the electrochemical kinetics, ultimately impacting the material's performance as an electrode in energy storage devices.[44]

The synthesis of bimetallic TMOs necessitates precise control over the composition, stoichiometry, and crystal structure to achieve desired properties. Various techniques, such as solid-state reactions, hydrothermal (HT), solvothermal (ST), sol–gel, and chemical vapor deposition (CVD) have been employed to fabricate tailored ternary oxides. These synthesis methods allow the manipulation of metal–metal interactions and the creation of heterostructures, resulting in improved properties for a particular application. In the following section, we discuss the influence of synthesis methods and corresponding parameters (*e.g.*, calcination temperature and surfactant) on the structural and morphological properties of ZMO.

4 Methods for ZMO fabrication

In this section, we introduce various synthesis methods utilized for ZMO fabrication for supercapacitor and battery applications. Based on reported studies, the HT and ST methods are predominantly employed due to their ability to provide better control over particle size, morphology, and crystallinity. Other techniques, such as co-precipitation (PC), sol–gel, and microwave-assisted synthesis, are also used. These methods enable precise control over the structural and morphological features of ZMO, which directly impact its electrochemical performance. For example, calcination temperature, reaction time, and surfactant selection are critical parameters that influence the final properties of ZMO. The following section details the influence of these synthesis techniques and parameters on the material's performance.

4.1 Hydrothermal (HT) and solvothermal (ST) synthesis

HT/ST synthesis methods are one-step processes that offer several advantages, such as environmental friendliness, effective solution dispersion, and the ability to operate under high pressure. These methods are particularly appealing due to their mild operating conditions (typically under 200 °C), and they can be cost-effective compared to other solution-based synthesis techniques. When water is used as the solvent, the process is referred to as HT, while the use of other solvents (like ethanol or methanol) classifies it as ST. Autoclaves, commonly used in this synthesis, have applications in fields such as microbiology, geothermal studies, and interdisciplinary scientific research.[45–47] These methods offer scalability for industrial production, enabling control over reaction stoichiometry, low aggregation, and producing highly pure powders.[48,49] HT/ST synthesis also allows for the precise manipulation of size distribution, shape, morphology, and chemical reactions, giving researchers the flexibility to tailor metal oxide particles for specific applications by controlling precursor composition and reaction conditions, along with the use of seed templates.[50–52]

A variety of morphologies of ZMO are achievable *via* HT/ST synthesis such as nanoparticles, nanorods, nanowires, nanosheets, nanofibers, hollow microspheres, nanoplates, flake-shaped, loaf-like structures and hierarchical structures. All these morphologies with varying surface areas, pore width distribution, pore volume, and hierarchy of the porous system directly impact the electrochemical device performance. For example, porosity not only increases the surface area for electrode–electrolyte reactions, but also alleviates the mechanical stress by accommodating the volume variation from the repeated cycling.[53]

4.1.1 Hydrothermal (HT) synthesis. Before delving into more complex HT synthesis routes, we will first examine a simple example of HT synthesis for obtaining nanostructured ZMO. Park *et al.*[54] synthesized ZMO by heating an autoclave containing a vigorously stirred precursor solution consisting of $KMnO_4$, $KMnO_4$, and $Zn(NO_3)_2$. The chemical reaction inside the autoclave with the precursor solution can be described as follows:

$$MnSO_4 + 2KMnO_4 \rightarrow 3MnO_2 + K_2SO_4 + O_2 \quad (1)$$

$$Zn(NO_3)_2 \rightarrow ZnO + NO_2 + NO + O_2 \quad (2)$$

$$MnO_2 + NO \rightarrow MnO + NO_2 \quad (3)$$

$$2ZnO + 2MnO + O_2 \rightarrow 2ZnMnO_3 \quad (4)$$

$$ZnMnO_3 + MnO \rightarrow ZnMn_2O_4 \quad (5)$$

Another common precursor other than $KMnO_4$ for Mn in the HT/ST route is Mn nitrate. Usually, the precursor metal nitrate solution decomposes upon heating, reacting with oxygen present in the system to form metal oxides and other byproducts such as nitrogen oxides. Ren *et al.*[55] uniquely synthesized ZMO with rugby ball morphology by adding NH_4F (shaping the material) as an additive to the precursor solution before heating the autoclave. NH_4F controls the release of carbonate ions, influencing how the material forms. When heated, NH_4F played a major role in how the material adhered to the substrate. By changing factors such as surfactants and additives, they obtained a variety of structures and composites through the HT process. For instance, Zhang *et al.*[56] synthesized porous ZMO nanowires by using a different alkaline agent. This agent

reacted with zinc and manganese ions to form complex compounds, which then formed long-chain polymers. These polymers self-assembled into nanowires, which were then heated to create porous ZMO nanowires. However, the resulting material had a low surface area, 15.8 $m^2 g^{-1}$. Zhu *et al.*[56] showed how different surfactants could lead to different shapes even when using the same starting materials and process. They tested this with several surfactants. With cetyltrimethylammonium bromide (CTAB), they obtained a honeycomb-like structure made of densely packed nanoparticles. With PEG, they observed porous microspheres with a rough surface. With polysorbate-80, they observed flower-like microspheres with a loose texture made of nanosheets.

HT treatment is a versatile technique, effective not only for creating pure metal oxides but also for producing composites. By adding materials such as graphene, carbon nanotubes (CNTs), reduced graphene oxide (rGO) sheets, or other components to the initial solution, researchers can synthesize a variety of ZMO-based composites. For instance, to improve ZMO's conductivity, Le *et al.*[57] combined it with rGO and a conductive polymer using an HT method. This created an aerogel with a 3D structure where ZMO nanoparticles were dispersed within the graphene oxide sheets. The added polymer coated the surface, enhancing the material's properties.

Guan *et al.*[58] synthesized a sandwich-like ZMO composite by using high temperatures to turn a glucose polymer into carbon nanosheets that encase ZMO nanoparticles. This unique composite features a porous carbon outer layer. Chen *et al.*[59] developed a method for creating porous ZMO/carbon microspheres using leftover microalgae. They coated the microalgae with manganese oxide and heated it to create a porous carbon template. This template was then used to create the final ZMO/carbon spheres. Other researchers have used various biomass sources such as egg whites and peanut shells to create similar composites. For example, Lin *et al.*[60] used milk as a carbon source. They added milk to the precursor solution and applied heat, creating a carbon matrix with embedded ZMO nanoparticles.

Other efforts for synthesizing modified ZMO were conducted by various researchers using HT methods. Wang *et al.*[61] synthesized Cd-doped ZMO microspheres at 200 °C for 18 hours, resulting in uniform spherical structures with an average diameter of approximately 2 μm. Bera *et al.*[62] developed honeycomb-like ZMO@$Ni(OH)_2$ core–shell structures, featuring nanosheets and interconnected honeycomb walls that formed a hierarchical architecture. Rosaiah *et al.*[63] prepared ZMO/rGO composites by combining HT treatment with subsequent annealing. Through precise control of synthesis parameters and calcination temperatures, they achieved needle-like surface architectures on ZMO/rGO microspheres. The inclusion of RGO enhanced the surface area and contributed to the formation of porous, interconnected structures. These examples illustrate the versatility of HT synthesis in producing diverse and tailored morphologies for ZMO-based materials. Jiu *et al.*[64] recently synthesized hierarchical mesoporous ZMO@$Mo_6S_{9.5}$ microflowers using a two-step hydrothermal-calcination process. This method facilitated the growth of ultrathin $Mo_6S_{9.5}$ nanosheets on ZMO microspheres, forming a three-dimensional architecture. The hierarchical structure was characterized by its interconnected nanosheets, which provided a porous framework and enhanced morphological features suitable for various applications.

4.1.2 Solvothermal (ST) synthesis. In a conventional ST synthesis, the cations Mn^{2+} and Zn^{2+} interact with carbonate ions (CO_3^{2-}) in an ethylene glycol (EG) solvent at high temperatures. The solubility products $ZnCO_3$ and $MnCO_3$ lead to precipitation due to their analogous crystal structures, forming $Zn_xMn_xCO_3$. To reduce the surface energy, the $Zn_xMn_xCO_3$

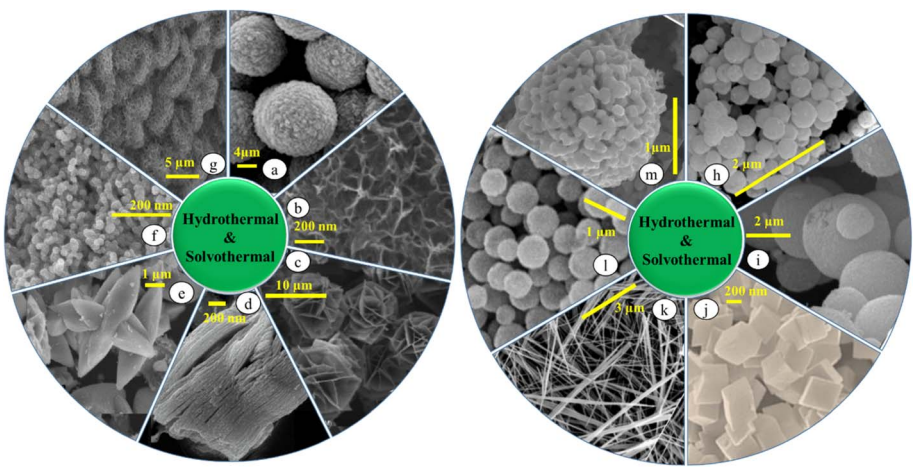

Fig. 3 ZMO morphologies produced by HT/ST synthesis (conditions for every morphology are reported in Table 1): (a) reproduced from ref. 72 with permission from Elsevier, copyright 2015, (b) reproduced from ref. 73 with permission from Elsevier, copyright 2022, (c) reproduced from ref. 74, (d) reproduced from ref. 75 with permission from Elsevier, copyright 2020, (e) reproduced from ref. 76 with permission from Elsevier, copyright 2021, (f) reproduced from ref. 70 with permission from Elsevier, copyright 2018, (g) reproduced from ref. 55 with permission from Elsevier, copyright 2018, (h) reproduced from ref. 77 with permission from Wiley Online Library, copyright 2022, (i) reproduced from ref. 78 with permission from Elsevier, copyright 2021, (j) reproduced from ref. 79 with permission from Elsevier, copyright 2019, (k) reproduced from ref. 53 with permission from Elsevier, copyright 2015, (l) reproduced from ref. 39 with permission from ACS, copyright 2018, and (m) reproduced from ref. 65 with permission from Elsevier, copyright 2014.

particles undergo aggregation during the subsequent calcination process, resulting in the formation of microspherical morphologies.[65] Xu *et al.*[39] synthesized a triple-shelled ZMO structure by adding salicylic acid before the ST treatment. This caused the material to shrink inwards during heating, forming multiple shells. They found that a slower heating rate allowed more time for the inner layers to detach, creating additional shells. Similarly, Yuan *et al.*[66] produced mesoporous microspheres with a hierarchical structure. By heating the mixture twice, they created hollow spheres. However, heating it only once resulted in a "ball-in-ball" structure.[67] Researchers often use PVP in the HT synthesis of ZMO to create hollow microspheres. However, Rong *et al.*[68] used CTAB to create non-hollow microspheres. Various other ZMO nanostructures, like nanocubes[69] and interconnected nano-peanut-like structures,[70] have also been synthesized using this method under different conditions. Zhang *et al.*[71] investigated how the choice of solvent significantly affects the morphology of ZMO prepared through a ST approach followed by calcination. Their study revealed that when ethylene glycol was used as the solvent, it facilitated the formation of a unique pomegranate-like ZMO structure. This morphology consisted of micron-scale spheres made up of closely packed nanoparticles, likely due to the high viscosity of ethylene glycol, which limited particle mobility and encouraged compact aggregation during the growth process. Conversely, using water as the solvent resulted in a more uniform microspherical ZMO morphology, with larger, smoother particles and less-defined secondary structures. The lower viscosity of water allowed for more unrestricted particle migration and growth, producing these distinct differences in the final structure. Fig. 3 presents the resulting ZMO morphologies obtained under various conditions by HT and ST methods, and the details are provided in Table 1.

4.2 Co-precipitation (CP)

CP is a chemical synthesis technique where nucleation, growth, coarsening, and agglomeration processes occur simultaneously. It leads to the formation of insoluble species under high supersaturation conditions. The process involves nucleation, resulting in the formation of numerous small particles, and secondary processes such as Ostwald ripening and aggregation that significantly impact the final product's size, morphology, and properties. Thus, this facile method finds applications in synthesizing metal oxides, chalcogenides, and nanoparticles for various applications including EES. Compared to HT/ST techniques, CP offers a simpler, quicker process, requiring no high-pressure or high-temperature equipment, and providing decent control over particle size and composition, thus making it more suitable for large-scale production.

In a typical CP procedure of ZMO, a metal precursor solution is mixed with a solvent (ethanol/water) and a stabilizing agent (*e.g.*, oxalic acid), forming metal precipitates ($TC_2O_4 \cdot xH_2O$, where T = Zn, Mn). After the solvents evaporate, the precipitates are heated to high temperatures in air to obtain ZMO. For instance, Soundharrajan *et al.*[80] synthesized ZMO microrods using Mn^{2+} as an additive, following the same procedure with an increased concentration of the Mn precursor. Zhang *et al.*[81] controlled the morphology of ZMO using the same CP method, altering only the stabilizing agents. They found that CTAB, *n*-hexane, and cyclohexane produced large microspheres, small microspheres, and hexahedral morphologies, respectively. In another study, Zhang *et al.*[82] synthesized ZMO microspheres by mixing metal nitrates with sodium bicarbonate, forming metal carbonate precipitates. Heating these precipitates caused them to decompose from the inside out, creating hollow microspheres. The study found that higher temperatures (800 °C) destroyed

Table 1 Summary of ZMO morphologies and synthesis conditions produced by HT/ST

Caption in Fig. 3	Synthesis method	Precursors	*T* (°C)	Duration	Morphology	Ref.
(a)	HT	$MnCl_2$, $ZnCl_2$, and urea	200	24 h + calcination	Nanoparticles	72
(b)	HT	$KMnO_4$ and $Zn(NO_3)_2 \cdot 6H_2O$	160	2 h	Nanosheets	73
(c)	HT	$Zn(CH_3COO)_2 \cdot 2H_2O$, $Mn(NO_3)_2 \cdot 4H_2O$, and $FeCl_3 \cdot 6H_2O$	100	12 h	Nanoflakes	74
(d)	HT	MXene, $Zn(CH_3COO)_2$, $Mn(CH_3COO)_2$, ethanol, and ammonia	180	12 h	Nanosheets	75
(e)	HT	$Zn(CH_3COO)_2$ and $Mn(CH_3COO)_2$	180	24 h	Nanoflowers	76
(f)	HT	CTAB, $Zn(acac)_2$ and $Mn(acac)_2$	180	13 h + 3 h	Nano-peanuts	70
(g)	ST	$Zn(NO_3)_2 \cdot 6H_2O$, $Mn(NO_3)_2 \cdot 4H_2O$, NH_4F, and urea	120	5 h + 2 h calcination	Hierarchical porous rugby-ball	55
(h)	ST	$Mn(CH_3COO)_2 \cdot 4H_2O$, $Zn(CH_3COO)_2 \cdot 2H_2O$, and PVP	180	8 h + calcination	Microspheres	77
(i)	HT	$Zn(NO_3)_2 \cdot 6H_2O$ and $Mn(NO_3)_2$	160	9 h + 2 h calcination	Nanoparticles	78
(j)	ST	$Zn(CH_3COO)_2 \cdot 2H_2O$, $Mn(CH_3COO)_2 \cdot 4H_2O$, HMTA, and NH_4F	160	12 h + 3 h calcination	Nanocubes	79
(k)	HT	$ZnCl_2$, $MnCl_2 \cdot 2H_2O$, and triacetic acid	180	24 h + 2 h calcination	Nanowires	53
(l)	ST	$Zn(CH_3COO)_2 \cdot 2H_2O$, $Mn(CH_3COO)_2 \cdot 4H_2O$, salicylic acid, and PVP	160	14 h + 12 h calcination	Hollow microspheres	39
(m)	ST	$MnCl_2 \cdot 4H_2O$, $ZnCl_2$, and urea	200	24 h + 2 h calcination	Microspheres	65

the microsphere structure, while lower temperatures (400 °C) resulted in a dense material lacking porosity. The ideal temperature (600 °C) produced porous, hollow microspheres.

Besides creating carbon-based ZMO composites, doping with metal atoms such as tin (Sn) is another way to improve ZMO's conductivity and electrochemical properties for better energy storage performance. Chen *et al.*[83] created Sn-doped ZMO microspheres using a CP method. By adding tin oxide to the initial mixture and then heating it, they produced porous microspheres with increased surface area and larger pores compared to the undoped version. They could also increase the amount of tin to create heavily doped ZMO. Chen *et al.*[84] further improved the material by adding carbon to their Sn-doped ZMO. They used a combination of CP and HT methods, adding glucose during the HT step to create an amorphous carbon layer on the porous microspheres. This carbon coating significantly boosted performance, especially at high current density. The versatility of CP in synthesizing diverse ZMO structures was further emphasized by Zhou *et al.*,[85] who successfully fabricated hollow microrods with consistent particle sizes and high porosity. These hollow structures formed due to CO_2 release during metal oxalate decomposition, creating voids that increase the material's surface area. Surfactants such as mmol sodium citrate (SDS) promoted the organization of precursors into rod-like structures, with the degree of hollowness and uniformity depending on SDS concentration and reaction parameters. Calcination at 700 °C preserved the hollow architecture and ensured high crystallinity, while higher temperatures led to grain coarsening and structural collapse. These results demonstrate CP's adaptability in tailoring ZMO nanostructures for various applications.

4.3 Combustion method

The combustion method for metal oxide synthesis offers several advantages. First, it is a simple and cost-effective technique, requiring minimal equipment and operating at atmospheric pressure. The rapid and self-sustaining nature of the combustion reaction enables fast synthesis with high yields, resulting in shorter reaction times and increased productivity. Additionally, the combustion method often yields nanoparticles with a narrow size distribution and high phase purity, thanks to the homogeneous nucleation and growth facilitated by the exothermic reaction. The method can be easily scaled up for large-scale production and allows for control over particle size and composition, providing flexibility for tailoring properties to specific applications. Furthermore, the combustion method is energy-efficient, utilizing the exothermic reaction for heat generation. These combined advantages make the combustion method an attractive choice for metal oxide nanoparticle synthesis.[86]

Huang *et al.*[87] used a combustion method with different fuels to create hierarchical porous ZMO. They found that using sucrose as fuel resulted in pure ZMO nanoparticles. Sucrose acts as both a fuel and a complexing agent, reacting with metal nitrates to form a gel. During combustion, the organic components decompose, leaving behind hierarchical porous ZMO with macropores and mesopores. The combustion reaction can be written as follows:

$$Zn(NO_3)_2 + 2Mn(NO_3)_2 + C_{12}H_{22}O_{11} + 5O_2 = ZnMn_2O_4 + 12CO_2 + 11H_2O + 3N_2 \quad (6)$$

Kommu *et al.* synthesized rGO/ZMO using a similar procedure with the use of sucrose as the fuel.[88] Furthermore, creating

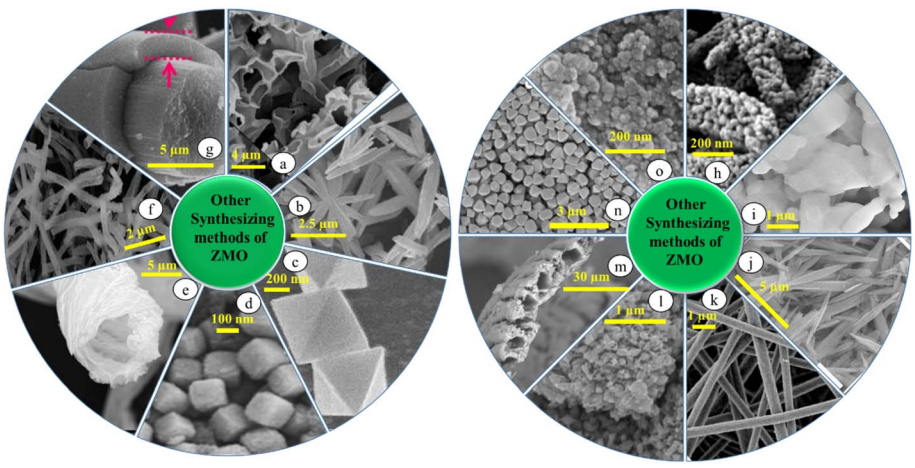

Fig. 4 Overview of ZMO morphologies and their synthesis methods (conditions for every morphology are reported in Table 2): (a) reproduced from ref. 102 with permission from Elsevier, copyright 2015, (b) reproduced from ref. 80 with permission from Elsevier, copyright 2020, (c) reproduced from ref. 61 with permission from Wiley Online Library, copyright 2021, (d) reproduced from ref. 103 with permission from Elsevier, copyright 2024, (e) reproduced from ref. 95 with permission from ACS, copyright 2018, (f) reproduced from ref. 104 with permission from Elsevier, copyright 2021, (g) reproduced from ref. 34 with permission from Elsevier, copyright 2019, (h) reproduced from ref. 105 with permission from Elsevier, copyright 2021, (i) reproduced from ref. 62 with permission from Elsevier, copyright 2022, (j) reproduced from ref. 106 with permission from Elsevier, copyright 2017, (k) reproduced from ref. 32 with permission from Elsevier, copyright 2015, (l) reproduced from ref. 107 with permission from ACS, copyright 2021, (m) reproduced from ref. 108 with permission from Elsevier, copyright 2022, (n) reproduced from ref. 109 with permission from Wiley Online Library, copyright 2022, and (o) reproduced from ref. 110 with permission from ACS, copyright 2016.

carbon composites is also very facile using the combustion technique. Sim *et al.*[89] used pineapple peel as a carbon source for a ZMO/C composite and achieved a high specific surface area material (976.12 $m^2 g^{-1}$). Sim *et al.*[90] synthesized a mesoporous carbon/ZMO composite by utilizing green waste as a sustainable carbon source. The resulting material exhibited a high surface area of about 800 $m^2 g^{-1}$, along with promising electrochemical performance. The observed improvements in specific capacitance were due to the synergistic interaction between the carbon matrix, which provided abundant active sites, and ZMO, which enhanced electrical conductivity. Hasan *et al.* synthesized Ni substituted ZMO through combustion and found that the grain size depends on the amount of Ni substitution. With high amounts of Ni in ZMO, larger non-uniform size grains were formed with an average size of 250 nm.[91]

Controlling the pore structure in combustion synthesis is challenging due to the rapid, high-temperature nature of the process. Abdollahifar *et al.*[92] tackled this by using PEG, which acts as both a pore-structuring agent and a source of carbon. This resulted in carbon-coated ZMO with well-defined nanocrystallites and improved electronic conductivity.

4.4 Other synthesis methods

Electrospinning is a versatile and cost-effective method for creating one-dimensional ZMO nanowires with high aspect ratios. This technique allows for control over diameter, surface area, and porosity. Joshi *et al.*[93] used electrospinning to create a binder-free ZMO/carbon nanofiber with improved mechanical stability and electrode–electrolyte contact. Similarly, Radhamani *et al.*[94] synthesized Mn_2O_3/ZMO nanofibers by varying the compositions and diameters (50 to 250 nm) *via* electrospinning.

Recently, biomorphic materials, which use biological templates, are gaining popularity due to their simple synthesis process. Luo *et al.*[95] created ZMO microtubules using cotton as a template. By immersing cotton in a metal precursor solution and then heating it, they were able to replicate the cotton's structure, creating mesoporous ZMO tubes. This resulted in a high surface area material with an average pore size of 5 nm. Additionally, several noteworthy ZMO morphologies have been developed for energy storage applications, including, the aerogel, MOF-derived, flower-like, nanopyramids, MXene-based composite and nanocages.[96–101] Fig. 4 presents a selection of ZMO morphologies synthesized using various methods, except for the HT and ST methods, and the details are provided in Table 2.

Table 3 provides a summary of various synthesis methods employed in the fabrication of ZMO, categorized by their underlying principles. For each method, a specific example with precursors, conditions, and resulting morphology is included. The advantages and disadvantages of each method are compared, considering factors such as cost, complexity, scalability, and control over morphology. In the following section, we explore how synthesized ZMO with varying morphologies performs in supercapacitor and battery applications. Additionally, Fig. 5 shows a polygon radar chart that compares different synthesis techniques according to important metrics including crystallinity, specific surface area, morphology controllability, equipment complexity, and reaction time. This visual representation facilitates an easy assessment of each method's strengths and limitations.

5 Supercapacitor application of ZMO

ZMO has emerged as a highly promising material for supercapacitor applications, garnering significant attention from researchers and resulting in an extensive body of literature as summarized in Table 4 at the end of this section. The exceptional performance of ZMO in supercapacitors can be attributed to several key properties: its spinel structure with voids that facilitate ion accommodation, its bi-metallic nature that increases the number of active sites, its pseudocapacitive behavior in neutral electrolytes, depending on the morphology and its specific surface area. The electrochemical performance of ZMO is notably influenced by various factors, including

Table 2 Overview of ZMO morphologies using various synthesis methods

Caption in Fig. 4	Synthesis method	Morphology	Ref.
(a)	Template method	Honeycomb	102
(b)	Co-precipitation	Microrods	80
(c)	Cation exchange	Hollow octahedra	61
(d)	Microemulsion	Submicron cubic	103
(e)	Biomorphic	Microtubules	95
(f)	Electrospinning	Hollow nanofibers	104
(g)	Electrodeposition	Fiber-like	34
(h)	Coprecipitation + calcination	3D skeleton structure nanorods	105
(i)	Sol–gel	Nano block-like	62
(j)	Co-precipitation	1D nanostructures	106
(k)	Electrospinning + calcination	Nanofibers	32
(l)	Low-temperature synthesis	Particle-like morphology	107
(m)	Carbon gel-combustion + hard template	Hollow porous panpipe-like	108
(n)	*In situ* electrochemical	Quantum dots	109
(o)	Precipitation	Nanoparticles	110

Table 3 Evaluation of the strengths and weaknesses of various ZMO fabrication techniques

Synthesis method	Advantages	Drawbacks
Hydrothermal (HT)	- One-step synthesis, allowing for high purity and low aggregation - Mild operating conditions (<200 °C) - Scalability to industrial demands - Good solution dispersion and control over reaction stoichiometry - Variety of morphologies achievable (*e.g.*, nanoparticles, nanowires, and hollow microspheres)	- Requires high-pressure equipment (autoclave) - Relatively longer reaction times - Complex optimization of conditions may be required - May have limited scalability
Solvothermal (ST)	-Similar to HT but allows for more versatile solvents (*e.g.*, ethanol and methanol) - Good control over morphology and surface area - Fast synthesis with simultaneous formation of solid solutions	- Higher temperatures may be required - Potential environmental concerns based on solvents used
Co-precipitation (CP)	- Simple and cost-effective and requires no high-temperature equipment - Faster reactions compared to HT/ST methods - Good scalability for large-scale production - Allows for precise control over particle size and composition	- Low crystallinity, often requires post-synthesis treatment - Limited control over morphology
Combustion	- Simple and cost-effective with minimal equipment requirements - High phase purity and narrow size distribution - Scalable for large-scale production	- Rapid synthesis can make controlling morphology challenging - Limited ability to control particle size
Electrospinning	- High aspect ratio nanofibers, enhancing electrode performance - Versatile method for producing a wide range of materials	- Requires specialized equipment for electrospinning - Process complexity and potential difficulties in scaling up
Biomorphic synthesis	- Simple synthesis with natural templates leading to unique morphologies - High surface area and porosity due to structure replication	- Limited to specific organic templates - The process may be slow and dependent on template availability

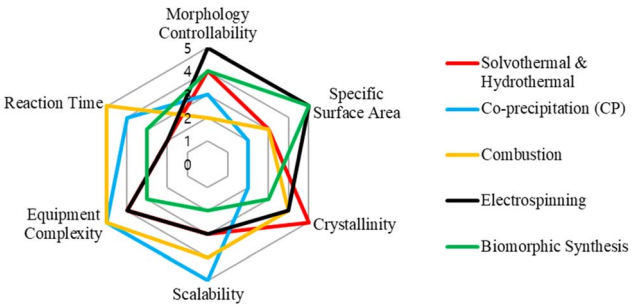

Fig. 5 Polygon radar chart comparing various synthesis methods based on key parameters, including morphology controllability, specific surface area, crystallinity, equipment complexity, and reaction time, which are extracted and explained in Table 3.

shape/morphology, phase purity, and surface area. Several innovative approaches have been employed to enhance device performance, including designing materials with porous nano-architectures to shorten ion-diffusion paths, fabricating nano-composites to leverage synergistic effects, doping to improve electrical conductivity, and synthesizing novel structures to enhance shell porosity and surface area. Based on the literature, ZMO is mainly synthesized using HT methods and tested in two types of electrolytes: alkaline (mainly KOH) and neutral (mainly Na_2SO_4). Pure ZMO materials exhibit capacitances ranging from 150 to 1000 F g^{-1}, but when combined with carbon composites or doped, capacitances can even reach up to 1800 F g^{-1}. The electrode–electrolyte interface plays a crucial role in governing electrochemical reactions, which in pseudocapacitor materials can occur through surface adsorption/desorption, metal cation (de)intercalation, and faradaic redox reactions.

The reaction mechanisms of ZMO in a KOH electrolyte can be described as follows:[125]

$$(ZnMn_2O_4)_{surface} + K^+ + e^- = [KZnMn_2O_4]_{surface} \quad (7)$$

$$(ZnMn_2O_4) + K^+ + e^- = [ZnMn_2O_4]K \quad (8)$$

The electrolyte also influences the reaction mechanism, while in the case of ZMO, reversible conversion reactions occur when ZMO interacts with hydroxide ions. The conversion reaction mechanisms of ZMO in an alkaline electrolyte (*e.g.*, KOH) can be expressed as follows:[79]

$$ZnMn_2O_4 + OH^- + H_2O \leftrightarrow ZnOOH + 2MnOOH + e^- \quad (9)$$

Table 4 Electrochemical characterization of ZMO in supercapacitors

Method	Morphology	Electrolyte	Capacitance (F g^{-1})	Capacity retention (cycles)	Ref.
Hydrothermal	Nanocubes	2 M KOH	776 at 5 mV s^{-1}	91% (5000)	69
	Microspheres	2 M KOH	155 at 2 mV s^{-1}	99% (1100)	72
	Cd-doped ZMO	2 M KOH	364 at 2 mV s^{-1}	—	111
	Sn doped C/ZMO microspheres	1 M KOH	1010 at 1 A g^{-1}	83% (2000)	84
	Composite with Mn_2O_4	2 M KOH	380 at 0.5 A g^{-1}	92% (2000)	76
	Microspheres/$ZnFe_2O_4$ composite	3 M KOH	1024 mF at 10 mA cm^{-2}	95% (3000)	74
	Composite with rGO	3 M KOH	628 at 1 A g^{-1}	95% (10 000)	63
	ZnO@ZMO/rGO	6 M KOH	276 mF at 0.5 mA cm^{-2}	88% (10 000)	54
	Composite with $Ni(OH)_2$	1 M KOH	2577 at 1 A g^{-1}	90% (10 000)	112
	Nanoparticles	0.5 M KCL	675 at 5 mV s^{-1}	61% (1000)	113
	Composite with Zn-birnessite	1 M Na_2SO_4	1903 mF at 3 mA cm^{-2}	93% (16 000)	73
	Ni coated ZMO	1 M Na_2SO_4	193 at 5 mV s^{-1}	98% (1200)	114
	ZMO aerogel with rGO	1 M Na_2SO_4	297 at 0.2 A g^{-1}	93% (5000)	57
	Microspheres	0.5 M Na_2SO_4	191 at 5 mV s^{-1}	98% (1000)	56
	Composite with MWCNTs	1 M Na_2SO_4	103 at 1 mV s^{-1}	56% (1000)	115
Solvothermal	Co doped ZMO nanocubes	1 M KOH	1196 at 1 A g^{-1}	80% (4000)	79
Co-precipitation	Composite with SnO_2	6 M KOH	658 at 1 A g^{-1}	—	116
	Pomengranate-like	1 M KOH	447 at 1 A g^{-1}	52% (800)	117
	Nanoparticles	2 M KOH	545 at 1 A g^{-1}	—	118
	Plate-like	1 M Na_2SO_4	1093 at 1 A g^{-1}	96% (5000)	119
	Sn doped ZMO microspheres	1 M KOH	530 at 1 A g^{-1}	77% (2000)	83
Elec activation	Composite with CNTs	2 M KOH	443.9 at 1 A g^{-1}	88% (10 000)	120
Combustion	Composite with carbon	6 M KOH	119 at 0.3 A g^{-1}	97% (5000)	89
	Composite with carbon	6 M KOH	122.94 at 0.3 A g^{-1}	90% (5000)	90
Auto-combustion	Composite with rGO	1 M LiOH	783 at 5 mV s^{-1}	75% (10)	88
Electrospinning	Composite with carbon	6 M KOH	1080 at 1 A g^{-1}	92% (10 000)	93
	1D hallow nanofibers	1 M KOH	1026 at 1 A g^{-1}	100% (5000)	104
	Composite Mn_2O_3	1 M Na_2SO_4	360 at 0.1 A g^{-1}	98% (3000)	94
	Nanofibers	1 M Na_2SO_4	240 at 1 A g^{-1}	99% (2000)	121
Sol–gel	Composite with $MgFe_2O_4$	6 M KOH	450 at 10 mV s^{-1}	100% (1000)	122
Electrodeposition	Nanosheets	0.5 M Na_2SO_4	457 at 1 A g^{-1}	92% (4000)	123
	Composite with Mn_3O_4	1 M Na_2SO_4	321 at 1 mV s^{-1}	93% (2000)	124
MOF-derived	Composite with carbon nanorods	1 M Na_2SO_4	589 at 1 A g^{-1}	98% (5000)	71

$$MnOOH + OH^- \leftrightarrow MnO_2 + H_2O + e^- \quad (10)$$

Similarly, the reaction mechanisms of ZMO in neutral electrolytes (*e.g.*, Na_2SO_4) can be described as follows:[80]

$$(ZnMn_2O_4)_{surface} + Na^+ + e^- = [NaZnMn_2O_4]_{surface} \quad (11)$$

$$ZnMn_2O_4 + Na^+ + e^- = [ZnMn_2O_4]Na \quad (12)$$

In the following sections, we will investigate the effect of these two types of electrolytes on the electrochemical performance of ZMO.

5.1 ZMO in KOH electrolyte

5.1.1 Early work and challenges. Sahoo *et al.*[125] were the first to investigate ZMO for supercapacitors. Their ZMO had a near-spherical morphology (50 nm average particle size) and a porous structure, with a specific surface area of 2.6 m^2 g^{-1}. Despite the low surface area, the interconnected mesoporous structure facilitated ion diffusion, resulting in a specific capacitance of about 160 F g^{-1} at 3 mV s^{-1}. The cyclic voltammetry (CV) curve showed pseudocapacitive behavior, attributed to K^+ ion adsorption/desorption and (de)intercalation. Galvanostatic charge–discharge (GCD) tests confirmed this behavior. ZMO exhibited good cycling stability over 500 cycles with 100% coulombic efficiency. This first ZMO supercapacitor achieved an energy density of 18 W h kg^{-1} and a power density of 185 W kg^{-1}. Recently, Guo *et al.*[72] were the first to synthesize ZMO microspheres (average size 10 μm) on a Ti sheet, carbon cloth, and nickel foam using HT synthesis. ZMO on nickel foam showed the highest capacitance (about 155 F g^{-1} at 2 mV s^{-1}) and low contact resistance (0.2 Ω) due to improved adhesion, enhancing charge transfer kinetics.

However, distinguishing between electric double-layer capacitance (EDLC) and pseudocapacitance can be challenging. While both exhibit a linear dependence of stored charge on the potential window width, their charge storage mechanisms differ. Their CV profiles can appear similar with minor variations. Also, an EDLC electrode with non-linearity in the CV profile (blunt and slanted CV profile) due to high ESR and EPR can exactly depict a typical pseudocapacitance CV profile.[126] Therefore, it is advisable to verify other typical pseudocapacitance signatures and conduct quantitative kinetics analysis (calculation of b by formula $i(V) = av^b$),[92] to check whether the material exhibits EDLC ($b = 1$) or

pseudocapacitance (b nearly 1) behavior.[127,128] Additionally, there are also reports[79,117] which display the ZMO CV curve with a battery-type signature of a distinct redox peak. This peak rises from the non-capacitive faradaic process (eqn (9) and (10)) between the ZMO and the electrolyte (KOH), which does not come under pseudocapacitance behavior, but can be classified as hybrid supercapacitors if paired with a carbon electrode.

5.1.2 ZMO/carbon composites. Most pseudocapacitive materials always possess low conductivity, which limits the rate capability of the electrode at high current densities. Additionally, the pseudocapacitive process has comparatively sluggish kinetics compared to EDLC, leading to lower power density. Combining materials with different charge storage mechanisms can synergistically enhance the performance of supercapacitor devices. In this regard, Shen *et al.*[120] synthesized a composite of ZMO/CNT with abundant oxygen vacancies by using spent zinc–carbon battery powder as the raw material. Without any reduction process, the oxygen vacancies were generated by tuning Mn^{2+}/Mn^{3+} *via* the electrochemical activation method, which increased the electronic conductivity of the material and resulted in a specific capacitance of 443 F g^{-1} at 1 A g^{-1}. Additionally, the oxygen-deficient ZMO/CNT composite electrode displayed a prominent cycling performance by retaining 96.7% of its initial capacitance after 10 000 cycles at 1 A g^{-1}. Similarly, Rosaiah *et al.*[63] monitored and tuned the synthesized parameters to obtain a ZMO–rGO composite with a special spike-like morphology, achieving a maximum specific capacitance of 628 F g^{-1} at a current density of 1 A g^{-1}. Upon subjecting the composite electrode to 10 000 charge/discharge cycles at 1 A g^{-1}, it retained 95.2% of its initial capacitance.

However, the cost of CNTs, multi-walled CNTs (MWCNTs), graphene, and rGO is comparatively high compared to that of other conducting carbon materials. However, there has been significant interest in utilizing organic waste as a source of conductive carbon phases in composites for energy storage applications. Inspired by this approach, Sim *et al.*[89] created a porous zinc manganese oxide/carbon (ZMO/C) composite from pineapple peel using a combustion technique. The composite had a high surface area (976 m^2 g^{-1}) but a relatively low specific capacitance (104.89 F g^{-1} at 300 mA g^{-1}). However, it showed excellent capacity retention (97% after 5000 cycles) and rate capability due to its unique pore structure. Analysis revealed that the capacitance was mainly (62%) due to diffusion-controlled processes, with the remaining 38% was attributed to surface-induced capacitive behavior from the added carbon. In another study, Sim *et al.*[90] synthesized a ZMO/C composite using the combustion method, yielding a specific capacitance of 123 F g^{-1} at 0.3 A g^{-1} in 6 M KOH electrolyte. The low capacitance in both cases may be due to the presence of poorly conductive amorphous carbon. Adding more carbon content to the composite can increase the electronic conductivity of the composite, but higher weight percentages can affect the specific capacitance of the composite due to carbon's inherent low specific capacitance.

To address the challenge of optimizing carbon content in the composite, Guan *et al.*[58] synthesized the ZMO/C composite through HT, with a carbon content of 7.8% which can barely decrease the capacitance of ZMO. The intensity ratio of graphitized carbon to disordered carbon peaks (I_g/I_d) of ZMO/C from the Raman spectra is found to be nearly 1, indicating the formation of well-graphitized carbon in the composite. This addresses the poor electrical conductivity of disordered carbon *via* the combustion route. In addition to the above attributes of conducting carbon phases, a high surface area of 343.2 m^2 g^{-1} and the unique morphology of ZMO encapsulated in sandwich-like carbon nanosheets resulted in an impeccable capacitance value of 1786 F g^{-1} at 1 A g^{-1}, yielding 95% capacity retention.

ZMO/C nanofiber composites were synthesized by Yun *et al.* *via* electrospinning.[104] The capacitance value for the given nanofiber composite was 1026 F g^{-1} at 1 A g^{-1} using 1 M KOH as the electrolyte. Typically, KOH concentrations for electrolytes range from 1 to 6 M. The electrolyte concentration plays a crucial role in influencing electrochemical parameters, as an increase in concentration results in a higher number of ions available for (de)intercalation or (de)adsorption at the surface and electrode–electrolyte interface, thereby enhancing both diffusion and capacitive contributions. However, surpassing an optimal concentration may lead to reduced ionic resistance leading to higher solution resistance (R_s). The specific conductivity increased from 0.33 to 0.67 S cm^{-1} as KOH concentration increased from 1.5 to 6 M, followed by a slight decrease to 0.61 S cm^{-1} at 9 M.[129] Therefore, most of the cases listed in Table 4 do not exceed 6 M for KOH.

Joshi *et al.*[93] fabricated a flexible supercapacitor using zinc–manganese oxide coated carbon nanofibers. The composite nanofibers were synthesized using terephthalic acid, which improved fiber flexibility and ion diffusion, and sodium dodecyl sulfate, which ensured uniform ZnO distribution on the nanofiber surface during annealing. This surface modification with ZnO increased the electrochemical activity of the composite. An optimal zinc/manganese acetate ratio of 0.75 resulted in high specific capacitances: 1080 F g^{-1} and 817 F g^{-1} at current densities of 1 A g^{-1} and 10 A g^{-1} within a 1.6 V potential window. Furthermore, the device demonstrated excellent cycling stability, retaining 92% capacitance after 10 000 charge–discharge cycles. Bending tests confirmed the structural integrity and flexibility of the freestanding carbon nanofiber electrodes, showing minimal changes in the CV curve even at significant bending angles.

5.1.3 Doped ZMO. While incorporating carbon phases has shown significant potential in increasing electrochemical performance, doping offers an intriguing approach to augment electrochemical functionality. Doping modifies the electronic structure of the material, leading to improved properties. Khaja Hussain *et al.*[79] synthesized Co-doped ZMO nanocubes *via* the ST route, achieving a high specific capacitance of 1196 F g^{-1} at 1 A g^{-1}, significantly higher than the 267 F g^{-1} observed for undoped ZMO (Fig. 6). Although the Co^{2+} ions can incorporate and replace the Zn^{2+} ions due to a similar ionic radius, the inclusion of a larger concentration of Co^{2+} ions (*e.g.*, 7 mol%) will result in lattice structure distortion. It is also worth noting a significant difference in R_{ct} between pristine ZMO and Co-doped ZMO with optimal doping concentrations (5 mol%) of

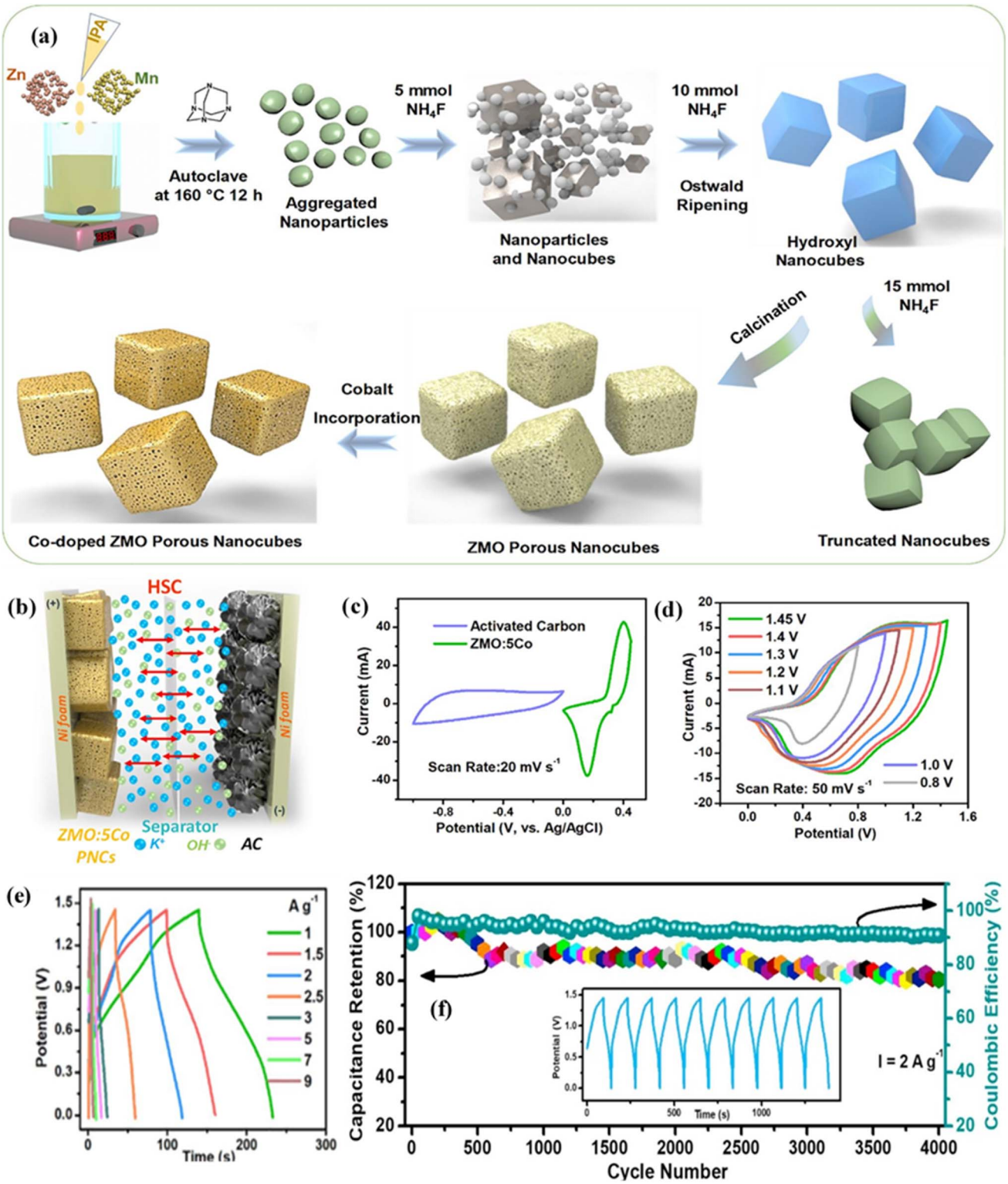

Fig. 6 Performance and application of ZMO and Co-doped ZMO PNC-based HSC devices. (a) Illustration of the synthesis process for ZMO and Co-doped ZMO PNCs; (b) diagram of the HSC device setup; (c) CV profiles of the ZMO:5Co PNCs and AC electrodes; (d) CV curves and (e) GCD curves of the HSC device recorded at various scan rates and current densities within the 0–1.45 V potential range. (f) Long-term cycling stability of the HSC device. Reproduced from ref. 79 with permission from Elsevier, copyright 2019.

6.51 and 1.21 ohms, respectively. However, exceeding this optimal doping concentration increased R_{ct} due to impurity ion scattering.

Wang *et al.*[111] synthesized Cd-doped ZMO, achieving a specific capacitance of 364 F g^{-1} at 2 mV s^{-1}. This lower capacitance compared to that of Co-doped ZMO can be

attributed to the nature of the Cd dopant. Unlike Co, Cd does not significantly enhance electrical conductivity or contribute to the charge storage mechanism. The larger size of Cd ions compared to Zn ions increases the lattice constant, reducing the formation of high-density defects. However, Cd doping also results in a smaller grain size and increased grain boundaries. This increase in grain boundaries, evidenced by a larger semicircle in the electrochemical impedance spectroscopy (EIS) data, leads to a higher R_{ct} exceeding 20 Ω. Also, Chen *et al.*[84] interestingly combined the advantage of doping and incorporating carbon phases by synthesizing Sn-doped ZMO *via* the CP, followed by carbon coating over Sn-doped ZMO *via* the HT synthesis. Sn doping served to increase both the electrical conductivity and the surface area of ZMO, providing more active sites for electrochemical reactions. Furthermore, the synthesis process created a shell around the ZMO microspheres, which, in addition to the outer carbon coating, helped to buffer volume expansion during cycling. This combination of Sn doping, carbon coating, and a protective shell resulted in a high specific capacitance of 580 F g^{-1} at 5 A g^{-1} and excellent cycling stability.

5.1.4 ZMO composites with other metal oxides. Instead of doping, which replaces the metal cation within the structure, adding separate phases to the active material can enhance overall electrochemical performance. Sannasi *et al.*[76] synthesized a ZMO/Mn_2O_3 nanostructured composite which reacted with KOH similar to Co-doped ZMO to store extra capacitance through a faradaic reaction. Though the ZMO/Mn_2O_3 composite underwent a 2-way faradaic reaction (eqn (3) and (4)), the highest specific capacitance achieved was 173 F g^{-1} at 1 A g^{-1}. The relatively low capacitance compared to that of other composites can be attributed to the lack of a synergistic effect between the active material and the additive phases.

To showcase an example of the synergistic effect in ZMO composites, Heiba *et al.*[122] synthesized a $(1 - x)$ZMO/(x) $MgFe_2O_4$ composite using sol–gel, with different ratios of $x = 0$, 0.1, 0.5, 0.9, and 1. Among the different ratios of x, the highest capacitance of 502 F g^{-1} at 1 A g^{-1} was obtained for the sample 0.1ZMO/0.9$MgFe_2O_4$ due to the synergy between the ZMO and $MgFe_2O_4$ components, which surpassed the individual components of the composite. They also investigated the dielectric characteristics and AC conductivity of the composites in detail. With lower ZMO in the composite, the dielectric constant increases and the AC conductivity increased for the 0.1ZMO/0.9$MgFe_2O_4$ sample due to the small polaron hopping mechanism, in contrast to the correlated barrier hopping mechanism exhibited by the other samples.

In a similar vein, Sivaguru *et al.*[130] synthesized nanocomposites where irregular sheet-like ZMO and cube-like morphology of $Cu_{1.5}Mn_{1.5}O_4$ coalesce to establish a heterostructure that amplifies active sites and facilitates ion transport. It also demonstrated a battery-type charge storage mechanism, with significant inner capacity derived from ion intercalation, and its reversibility is confirmed by R^2 values approaching unity for both oxidation and reduction peaks. This resulted in a specific capacitance of 468 F g^{-1} at 0.5 A g^{-1} and 84% capacity retention after 20 000 cycles.

Other researchers have explored various ZMO composites for enhanced supercapacitor performance. For example, Pearline *et al.*[116] synthesized a ZMO/SnO_2 composite with a high specific capacitance of 658 F g^{-1} at 1 A g^{-1} in a 6 M KOH electrolyte. Park *et al.*[54] developed a flexible composite of ZnO nanospheres, ZMO nanorods, and rGO, achieving 276.3 mF cm^{-2} at 0.5 mA cm^{-2} with good energy and power densities and excellent cycling stability. Bera *et al.*[112] created a ZMO/$Ni(OH)_2$ composite with a remarkable specific capacitance of 2577 F g^{-1} at 1 A g^{-1}, attributed to the increased surface area, synergistic effects, and unique core–shell morphology. This composite also demonstrated excellent capacitance retention (94.8% after 3000 cycles). Furthermore, a flexible asymmetric supercapacitor (ASC) device fabricated using this ZMO/$Ni(OH)_2$ composite and activated carbon (AC) electrodes with a PVA-KOH electrolyte achieved a specific capacitance of 138 F g^{-1} at 0.5 A g^{-1} and a high energy density of 43 W h kg^{-1}.

5.2 ZMO in neutral electrolytes

5.2.1 Influence of morphology and synthesis conditions. Several studies have investigated the impact of neutral electrolytes on the electrochemical performance of ZMO for supercapacitor applications. For instance, Bhagwan *et al.*[121] synthesized one-dimensional nanofibers *via* electrospinning, taking advantage of the increased interfacial area and interconnected particle network inherent in this morphology. The 1D nanofibers also offer the benefit of reduced surface energy, which minimizes active material aggregation and unwanted side reactions with the electrolyte. Their study focused on the electrical properties of the ZMO nanofibers, reporting an improved conductivity of 2×10^{-7} S cm^{-2} and a high Na^+ ion diffusion coefficient of 3.48×10^{-11} cm^2 s^{-1}. These efficient ionic pathways contributed to the impressive performance of the final supercapacitor device, which achieved an energy density of 25 W h kg^{-1} at a high-power density of 2.5 kW kg^{-1}.

Zhu *et al.*[56] studied the morphology impact on supercapacitor performance and found that a simple microsphere morphology showed better specific capacitance compared to honeycomb and flower-like morphologies. The honeycomb, microsphere and flower-like morphologies exhibited a bandgap of 2.29 eV, 2.23 eV, and 2.18 eV respectively. These differences in the bandgap were attributed to structural components and the abundance of defects in agglomerated nanoparticles. The porous microsphere morphology sample exhibited a specific capacitance of 191 F g^{-1} with an impeccable capacity retention of 98.8% after 1000 cycles.

With the use of deep eutectic solvents for the synthesis of metal oxides by functioning as both a precursor and a template, ZMO was synthesized by Samage *et al.*[131] The interactions occurring between hydrogen bond acceptors and donors are modifiable through the introduction of water to terminate the reaction. This capability permits the rapid synthesis of ZMO in a mere 1 minute, thereby establishing it as a more expedient, efficient, and economically viable approach for the production of ZMO. Nevertheless, extending the reaction duration to 10 minutes yielded superior performance, with the resultant

asymmetric supercapacitor attaining a specific capacitance of 331 F g^{-1} at 0.2 A g^{-1}, alongside an energy density of 74.5 W h kg^{-1} and a power density of 5.4 kW kg^{-1} measured at 4 A g^{-1}. Furthermore, the device retained 80% of its initial capacitance after enduring 30 000 charge–discharge cycles at 6 A g^{-1}.

Barkhordari *et al.*[123] studied the role of calcination temperature in ZMO properties which affects the performance of the electrode material. They synthesized ZMO *via* cathodic electrodeposition, followed by calcination at different temperatures (250, 450, and 650 °C). Increasing the calcination temperature led to higher crystallinity, as evidenced by XRD patterns, which typically improves conductivity. However, the 650 °C sample showed limited protonation reactions, hindering efficient ionic transport. Furthermore, increasing the calcination temperature decreased the surface area. The 450 °C sample achieved the best balance between crystallinity and surface area, resulting in the highest specific capacitance (456.8 F g^{-1} at 1 A g^{-1}) and good cycling stability (92.5% capacitance retention after 4000 cycles). In a related study, Gao *et al.*[119] maintained the same calcination temperature (450 °C) but varied the calcination time (6 h and 12 h). Both samples exhibited a plate-like morphology, but the 12 h calcination produced a larger crystallite size and a lower surface area. The 6 h calcined ZMO, with its higher surface area, achieved a specific capacitance of 1093 F g^{-1} at 1 A g^{-1}, and excellent cyclability (96.1% after 5000 cycles). This highlights the importance of optimizing both calcination temperature and time to achieve the desired ZMO properties for supercapacitor applications.

5.2.2 ZMO/carbon composites. Researchers have also explored incorporating carbon phases into ZMO to enhance its conductivity and electrochemical performance in neutral electrolytes. For example, Abdollahifar *et al.*[92] developed a ZMO/carbon composite that exhibited exceptional cycling stability, with no capacitance fading after 10 000 cycles and over 99% coulombic efficiency in 1.7 M Na_2SO_4. However, the composite had a specific capacitance of 150 F g^{-1} at 2 mV s^{-1}. This high stability but relatively low capacitance can be attributed to the dominant surface capacitive contributions in the composite,

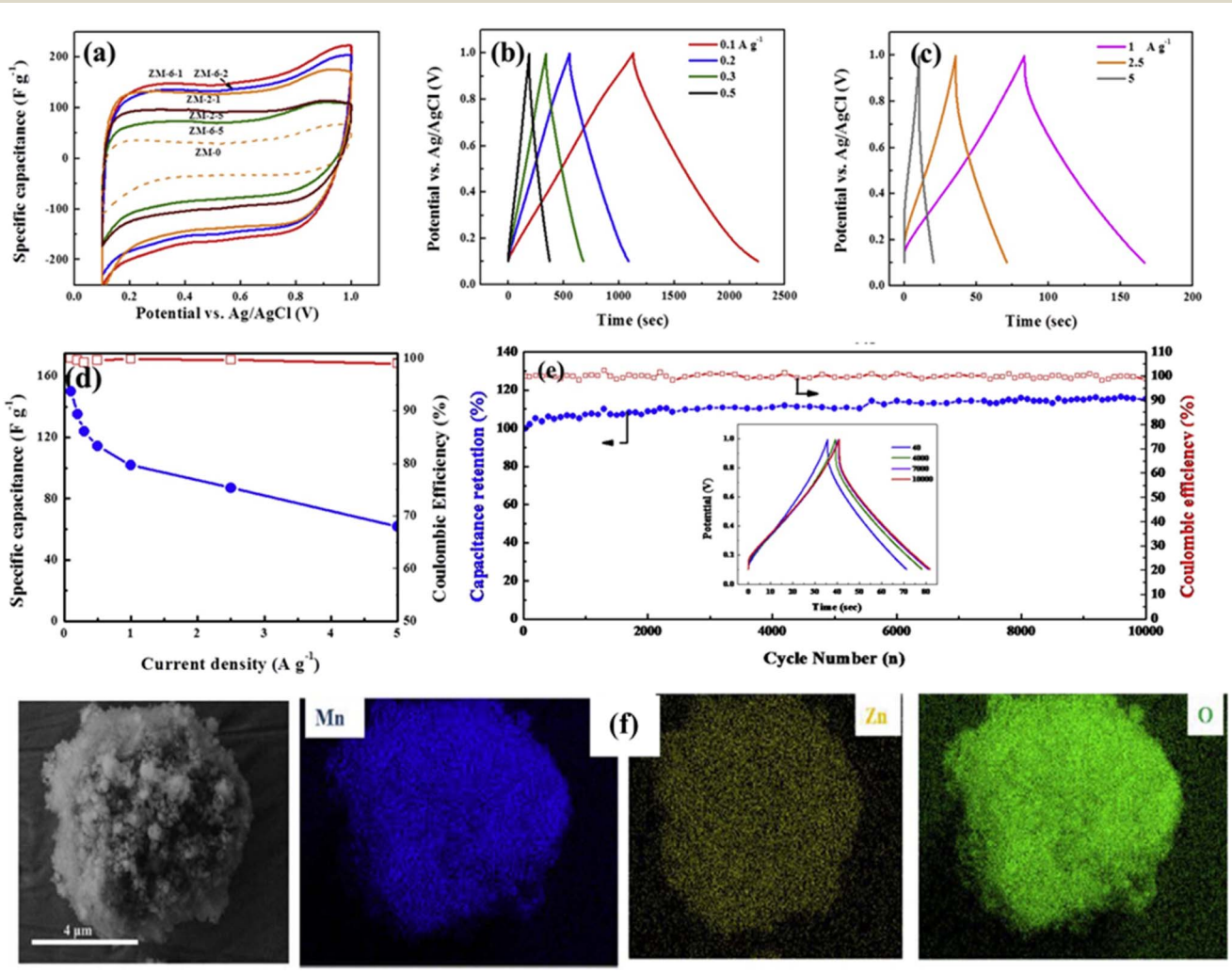

Fig. 7 Electrochemical characteristics and structural analysis of ZMO-6-1; (a) CV profiles of the synthesized samples at a scan rate of 2 mV s^{-1}; (b and c) GCD curves recorded at various current densities; (d) dependence of coulombic efficiency and specific capacitance on current density; (e) long-term cycling performance and coulombic efficiency over 10 000 cycles at 2.5 A g^{-1}, with insets showing GCD profiles at the 40th, 4000th, 7000th, and 10 000th cycles. (f) SEM image and elemental mapping showcasing its structural features and elemental composition. Reproduced from ref. 92 with permission from Elsevier, copyright 2018.

which were quantified as 76% at 1 mV s^{-1} and 89% at 5 mV s^{-1} through kinetic analysis (Fig. 7). A similar trend was observed in the aerogel-based ZMO/rGO studied by Le *et al.*[57] which demonstrated a lower specific capacitance of 108 F g^{-1} at 0.2 A g^{-1} in 1 M Na_2SO_4, but achieved a capacity retention of 93.27% after 5000 charge–discharge cycles. The lower specific capacitance compared to that of bare ZMO in some studies might be due to a lack of synergy between the carbon and ZMO phases.

In contrast, Zhu *et al.*[132] reported the highest specific capacitance for ZMO/C composites in neutral electrolytes, achieving 589 F g^{-1} at 1 A g^{-1}. They synthesized ZMO/carbon nanorods by pyrolysis of Zn–Mn MOF, which resulted in uniform dispersion of ZMO on the carbon matrix. This composite also exhibited good rate capability, retaining a specific capacitance of 278 F g^{-1} at 20 A g^{-1}, and outstanding cycling stability, with 98.1% retention after 2000 cycles at 10 A g^{-1}. The observed increase in capacitance after the first 500

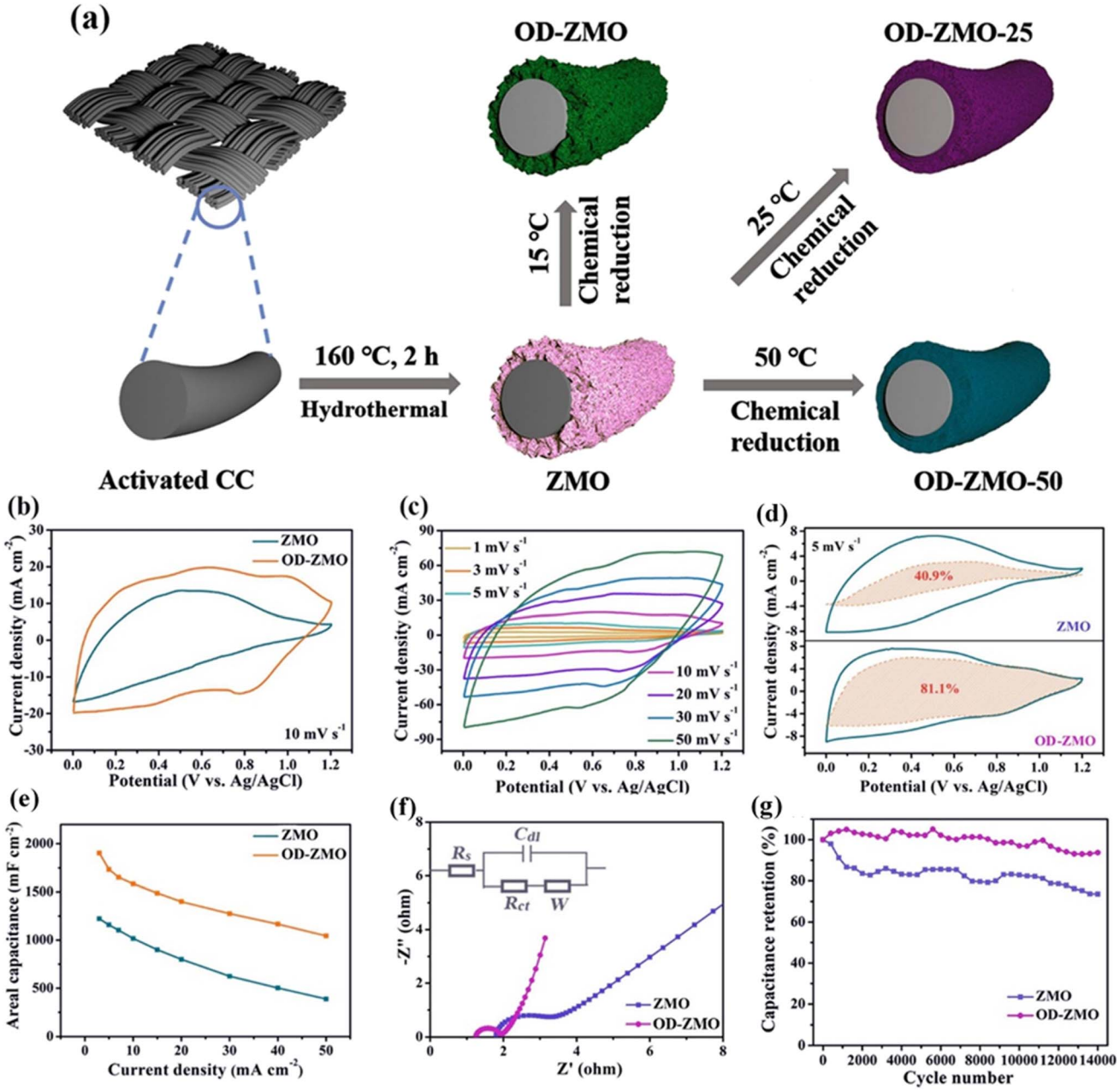

Fig. 8 Fabrication process and electrochemical properties of the OD-ZMO electrode: (a) diagram depicting the synthesis steps of the OD-ZMO electrode; (b) CV curves of the OD-ZMO electrode across different potential ranges at 20 mV s^{-1}; (c) CV curves comparing ZMO and OD-ZMO electrodes at 10 mV s^{-1}; (d) analysis of the capacitive charge contribution (indicated by the orange region) at 5 mV s^{-1}; (e) areal capacitance values obtained at current densities from 3 to 50 mA cm^{-2}; (f) Nyquist plots with an equivalent circuit model highlighting R_s (series resistance), R_{ct} (charge transfer resistance), W (Warburg impedance), and C_{dl} (double-layer capacitance); (g) cycling stability results recorded at 50 mA cm^{-2}. Reproduced from ref. 73 with permission from Elsevier, copyright 2022.

cycles was attributed to an activation effect. Compared to bare ZMO, the ZMO/C hybrid material showed significant improvements in specific capacitance, cyclability, and charge transfer resistance, highlighting the synergistic effect of the homogeneous ZMO distribution on the carbon matrix.

5.2.3 ZMO-based hybrid composites and modified ZMO. Combining ZMO with other metal oxides to create hybrid composites with enhanced electrochemical properties has also been explored. In hybrid composites, the ratio of components plays a crucial role in achieving optimal synergy. For instance, Zhao *et al.*[133] achieved excellent results with a ZMO/MnOOH composite using a 55 : 45 ratio while Radhamani *et al.*[94] synthesized a Mn_2O_3/ZMO nanofiber composite (99 : 1), achieving a maximum specific capacitance of 360 F g^{-1} at 0.1 A g^{-1}. The addition of just 1 wt% ZMO increased the electronic conductivity of the composite, and the synergy between the two materials enhanced the rate capability of the electrode. Likewise, Ameri *et al.*[124] addressed the bottleneck of low electrical conductivity in Mn_3O_4, one of the most stable forms of manganese oxide, by synthesizing a Mn_3O_4/ZMO composite using ZMO nanorods *via* cathodic electrodeposition. In addition to cation intercalation and de-intercalation into the voids of the ZMO crystal structure, a different process involving Na^+ ions and Mn_3O_4 occurs in Na_2SO_4 electrolyte. This composite, with its unique combination of charge storage mechanisms, achieved a high specific capacitance of 321 F g^{-1} at 1 mV s^{-1}, significantly higher than that of bare Mn_3O_4 (~248 F g^{-1}). This improvement was attributed to the lower R_{ct} (0.76 Ω) of the composite compared to bare ZMO (2.57 Ω). The composite also exhibited excellent cycling stability, retaining 93% of its initial capacity after 2000 cycles. Beyond compositing, Li *et al.*[114] modified ZMO by coating it with Ni. This coating altered the ZMO structure, enhancing its surface area and pore structure, and increased cationic ion penetration, leading to improved electrochemical reactions with the electrolyte. The resulting Ni-coated ZMO electrode demonstrated a high specific capacitance of 193 F g^{-1} in 1 M $NaSO_4$ at 200 mV s^{-1} and excellent cycling stability, maintaining 98.8% of its initial capacitance after 1200 cycles. Lyu *et al.*[73] synthesized a Zn-birnessite@spinel ZMO nanocrystal composite using a HT process followed by chemical reduction. They observed an interesting phase transformation mechanism from Zn-birnessite to spinel ZMO, driven by the formation of oxygen vacancies and Mn ion migration. These oxygen vacancies, confirmed by EPR analysis, led to a lower bandgap (1.06 eV for bare ZMO *vs.* 1.54 eV for the composite) and enhanced electrical conductivity, as evidenced by a low charge transfer resistance of 0.63 Ω. The oxygen vacancy-rich ZMO also exhibited a higher capacitive contribution (71.6%) compared to pure ZMO (28.4%), attributed to the increased electrochemically active surface area. These advantages resulted in a high areal capacitance of 1903 mF cm^{-2} at 3 mA cm^{-2} and excellent cycling stability (93.7% capacitance retention after 16 000 cycles). Furthermore, a flexible asymmetric supercapacitor assembled using this oxygen-deficient ZMO cathode and a V_2O_5 anode achieved a high operating voltage of 2.4 V and delivered an energy density of 6.24 mW h cm^{-3} (Fig. 8).

For real-world supercapacitor applications, Chen *et al.*[134] implemented a high-performance thermally charging supercapacitor, designed to integrate efficient thermoelectric conversion with exceptional electrochemical storage, tailored for wearable electronics. ZMO@$Ti_3C_2T_x$ MXene composite electrodes were synthesized with porous ZMO nanosheets, which play a crucial role in preventing the common issue of MXene restacking and increase the interlayer gap of $Ti_3C_2T_x$ MXene, hence inhibiting the collapse or aggregation of its layered structure. This integration complements interlayer space, facilitates ion diffusion paths, and promotes structural stability, hence optimizing charge transport and energy storage. The electrodes incorporate proton-donating groups (–OH) that enhance H^+ ion mobility, hence increasing electrochemical double-layer capacitance. The interaction between the electrode and electrolyte materials yielded a specific capacitance of 326.5 F g^{-1} at 1.0 A g^{-1}, with a retention of 94.2% after 5000 charge–discharge cycles. Also, the device attained a maximum energy density of 10.4 W h kg^{-1} and a power density of 1324 W kg^{-1}.

This section has explored the diverse applications of ZMO in supercapacitors, highlighting how morphology, composites, and doping influence performance. We discussed various ZMO morphologies and their performance in KOH and Na_2SO_4 electrolytes. The benefits of carbon-based composites and doping strategies were also examined, emphasizing the importance of synergistic interactions between ZMO and the composite material. Table 5 summarizes the electrochemical performance of ZMO supercapacitors across different electrolyte systems (KOH and Na_2SO_4) based on reclassified data from Table 4. The data indicate that KOH electrolytes generally enable higher peak capacitance values (120–2600 F g^{-1}) in ZMO supercapacitors, likely due to favorable alkaline conditions and the effectiveness of doping and conductive composites (*e.g.*, with $Ni(OH)_2$ and carbon). Na_2SO_4 systems demonstrate a moderate capacitance range (100–1100 F g^{-1}) but offer good overall performance with a potential emphasis on stability and cost-effectiveness. Strategies for Na_2SO_4 often involve morphology control and stable carbon composites, and these systems exhibit a wide range of cycle stability (1000–16 000 cycles). Overall, electrolyte choice significantly impacts ZMO

Table 5 Electrolyte-type dependent performance summary of ZMO supercapacitors from Table 4

Electrolyte type	Capacitance range (F g^{-1})	Typical capacitance test conditions (scan rate/current density)	Capacity retention range (%)	Typical capacity retention cycles
KOH	~120–2600	10 mV s^{-1}/0.3 A g^{-1}	52–100%	800–10 000
Na_2SO_4	~100–1100	1–5 mV s^{-1}/0.1–1 A g^{-1}	56–99%	1000–16 000

supercapacitor performance. KOH appears advantageous for maximizing capacitance, while Na_2SO_4 provides a balance of good performance and potentially enhanced stability. Further research should explore the mechanisms behind these differences and address unit inconsistencies in the original data.

6 Battery applications of ZMO

This section provides a comprehensive overview of ZMO's applications in three battery systems (LIBs, SIBs and ZIBs), highlighting recent advancements and addressing the challenges that hinder its widespread adoption. We will explore the diverse strategies employed to overcome these limitations, such as morphology control, compositing with conductive materials, and electrolyte optimization.

6.1 ZMO in LIBs

In the past few decades, there has been notable progress in LIB technology, enabling its widespread application in various devices ranging from portable electronics to electric vehicles. The high energy density and favorable cycle life of LIBs have garnered significant attention, driving further exploration of this technology. Graphite[135] remains the primary choice for anode materials in commercial batteries due to its cost efficiency, stability, and extended cycle longevity. Nonetheless, the limited theoretical capacity of graphite at 372 mA h g^{-1} emphasizes the necessity for alternative anode materials, such as silicon/graphite (carbon)[136–139] composites, as well as some alloy and conversion (typically TMOs) anodes.[140,141] Among TMOs, spinel ZMO is a promising anode material for LIBs due

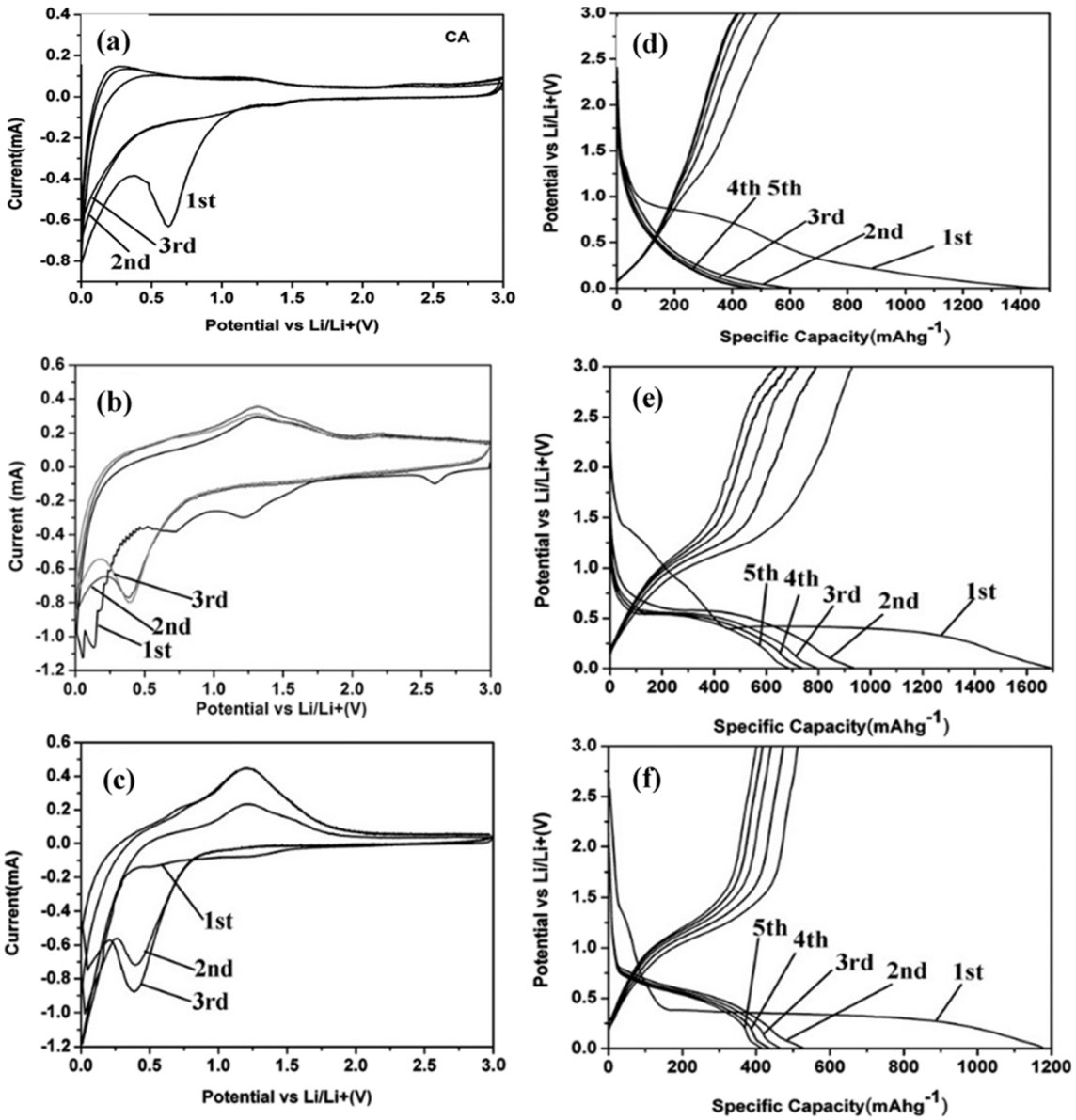

Fig. 9 CV curves of the first three cycles for (a) CA, (b) the 50% ZMO/CA hybrid, and (c) pure ZMO samples at a scan rate of 0.1 mV s^{-1} in the voltage range of 0.01–3.0 V. Initial charge–discharge curves of (d) CA, (e) the 50% ZMO/CA hybrid, and (f) pure ZMO samples at a current density of 100 mA g^{-1}. Reproduced from ref. 98 with permission from Wiley Online Library, copyright 2014.

to its high theoretical capacity (897 mA h g^{-1}), abundance, environmental friendliness, and low working voltage. ZMO's lithium storage mechanism involves both conversion and alloying reactions during lithiation.[142] Initially, a conversion reaction occurs as ZMO reacts with incoming Li, forming metallic nanograins dispersed in a Li_2O matrix (eqn (13)). Subsequently, Li alloying takes place with the Zn nanograins (eqn (14)), contributing to the overall Li storage. In addition to the alloying mechanism, Zn and Mn also react with Li_2O to form MnO and ZnO (eqn (15) and (16)).[82,142]

$$ZnMn_2O_4 + 8Li^+ + 8e^- \rightarrow Zn + 2Mn + 4Li_2O \quad (13)$$

$$Zn + Li^+ + e^- \rightarrow LiZn \quad (14)$$

$$2Mn + 2LiO_2 \rightarrow 2MnO + 4Li^+ + 4e^- \quad (15)$$

$$Zn + LiO_2 \rightarrow ZnO + 2Li^+ + 2e^- \quad (16)$$

Despite the several advantages of ZMO, there are few inherent flaws which retard the practical application or commercialization. Poor electronic conductivity of ZMO ($\sim 2.0 \times 10^{-7}$ S cm^{-1})[143] is considered a common problem for both battery and supercapacitor applications. To resolve this problem, various conductive materials such as conductive polymers, CNTs, graphene, and MXenes are composited with ZMO to enhance the conductive channel for electron transfer. Another major problem with ZMO based anodes is the drastic volumetric change during cycling, which, along with poor kinetics, induces pulverization and progressive aggregation of the active material, leading to capacity fading and reduced rate capability.[35,70] To alleviate this problem, fabricating novel nano- or porous structures can act as a buffer to absorb the stress induced by the volume change. Additionally, synthesizing porous structures with different morphologies can increase the contact area between the active material and electrolyte, thereby improving overall device performance. In the following paragraphs, we will discuss the progress made with ZMO as an anode material for LIBs.

6.1.1 Structure design of ZMO

6.1.1.1 Nanocrystalline ZMO. To enhance the performance of ZMO as an anode material, researchers have explored various nanostructured forms. Yang *et al.*[31] synthesized nanocrystalline ZMO using a polymer-pyrolysis method, achieving well-crystallized nanoparticles with optimal interaction with the current collector. This nanocrystalline ZMO exhibited a high initial discharge capacity of 1302 mA h g^{-1}, exceeding the theoretical value. After 50 cycles, the capacity was still a respectable 569 mA h g^{-1}, outperforming similar materials. This enhanced performance was attributed to the stable interaction between the LiZn–Zn–ZnO and Mn–MnO composites formed during cycling, which mitigated volume changes. While the reversible capacity was lower than that of $ZnCo_2O_4$ (900 mA h g^{-1}), ZMO offered advantages at average discharge and charge voltages (0.5 V and 1.2 V, respectively).

Yin and colleagues[98] synthesized spinel ZMO nanocrystals incorporated into a three-dimensional porous carbon aerogel (CA) using a solution immersion chemical approach. This hybrid structure, prepared with various ZMO incorporation ratios (15, 35, 50, and 75 wt%), takes advantage of the high surface area and extensive porosity of the CA, combined with the high electrochemical properties of ZMO, to create a highly conductive 3D network. The optimized 50% ZMO/CA composite demonstrated enhanced electrochemical performance, significantly exceeding the capacities of both pure ZMO and pure CA materials. This improvement is primarily due to the synergistic interaction between the ZMO nanocrystals and the porous CA matrix, which effectively mitigates volume changes during charge–discharge cycles, enhances electrical conductivity, facilitates ion diffusion, and reduces charge-transfer resistance (Fig. 9).

6.1.1.2 Porous and hollow ZMO architectures. The electrochemical performance of the cell is strongly influenced by the structural features of the electrodes. Lithium-ion diffusion channels, electrolyte wettability, and rate of the electrochemical reactions can be controlled by careful engineering of the materials. Recognizing the importance of morphology in influencing electrochemical performance, Zhang *et al.*[67] developed ZMO microspheres with a unique "ball-in-ball" hollow architecture that enhanced their performance as an anode material in LIBs. This structure achieved a high initial charge capacity (662 mA h g^{-1}) and excellent coulombic efficiency (nearly 100% after several cycles). The enhanced performance was attributed to the small nanoparticle size, facilitating Li^+ diffusion, and the hollow structure, which acted as an electrolyte reservoir. The "ball-in-ball" design also provided structural integrity, mitigating strain during cycling. Interestingly, the capacity increased to 750 mA h g^{-1} after 120 cycles, suggesting an activation process typical of transition metal oxides.

Luo *et al.*[95] synthesized mesoporous ZMO microtubules using cotton fiber templates; but their performance was limited by the high calcination temperature. Zhang *et al.*[82] confirmed the detrimental effects of high calcination temperatures on ZMO morphology and surface area. They optimized the synthesis process, achieving a ZMO variant (ZMO-600) with a high capacity of 999 mA h g^{-1} and excellent capacity retention (99.2% after 50 cycles). This improved performance was attributed to a novel redox mechanism involving reversible Mn^{2+}/Mn^{3+} conversion, interfacial storage, and a unique 3D porous core–shell structure that facilitated lithium-ion diffusion and accommodated volume changes of Mn. Additionally, part of the improved capacity can be attributed to an interfacial storage mechanism. Furthermore, the enhanced stability is linked to the unique 3D porous core–shell structure of the material, which facilitates lithium-ion diffusion and enables effective volume accommodation during cycling, thereby reducing structural degradation. Xu *et al.*[39] controlled the morphology of ZMO with double or triple-shelled hallow microspheres by simply varying the annealing ramp rate. These studies highlight the critical influence of calcination temperature and the annealing ramp rate on the resulting ZMO morphology and electrochemical properties. Wang *et al.*[65] also recognized the importance of morphology, developing porous ZMO microspheres through a solution-based method followed by

calcination. This interconnected porous architecture enhanced lithium storage, achieving a specific capacity of 800 mA h g^{-1} after 300 cycles. The improved performance was attributed to efficient charge transfer, reduced pulverization, and better accommodation of volume changes during cycling.

6.1.1.3 Defect engineering and doping. Introducing anion defects, such as oxygen vacancies, in transition metal oxides can significantly enhance their electrochemical activity. Oxygen vacancies reduce the bandgap and amplify the pseudocapacitive effect, boosting energy storage capabilities. Cheng *et al.*[105] developed oxygen vacancy-enriched ZMO nanorods (OZMO) that demonstrated a high reversible capacity of 1566 mA h g^{-1} after 50 cycles at 0.1 A g^{-1} when used as an anode in LIBs. OZMO also exhibited outstanding cycling performance (380 mA h g^{-1} after 1000 cycles at 10 A g^{-1}) and favorable environmental adaptability, maintaining high capacities at both −5 °C and 55 °C (Fig. 10). Du *et al.*[43] further explored the concept of anionic vacancies in ZMOs derived from MOFs. They

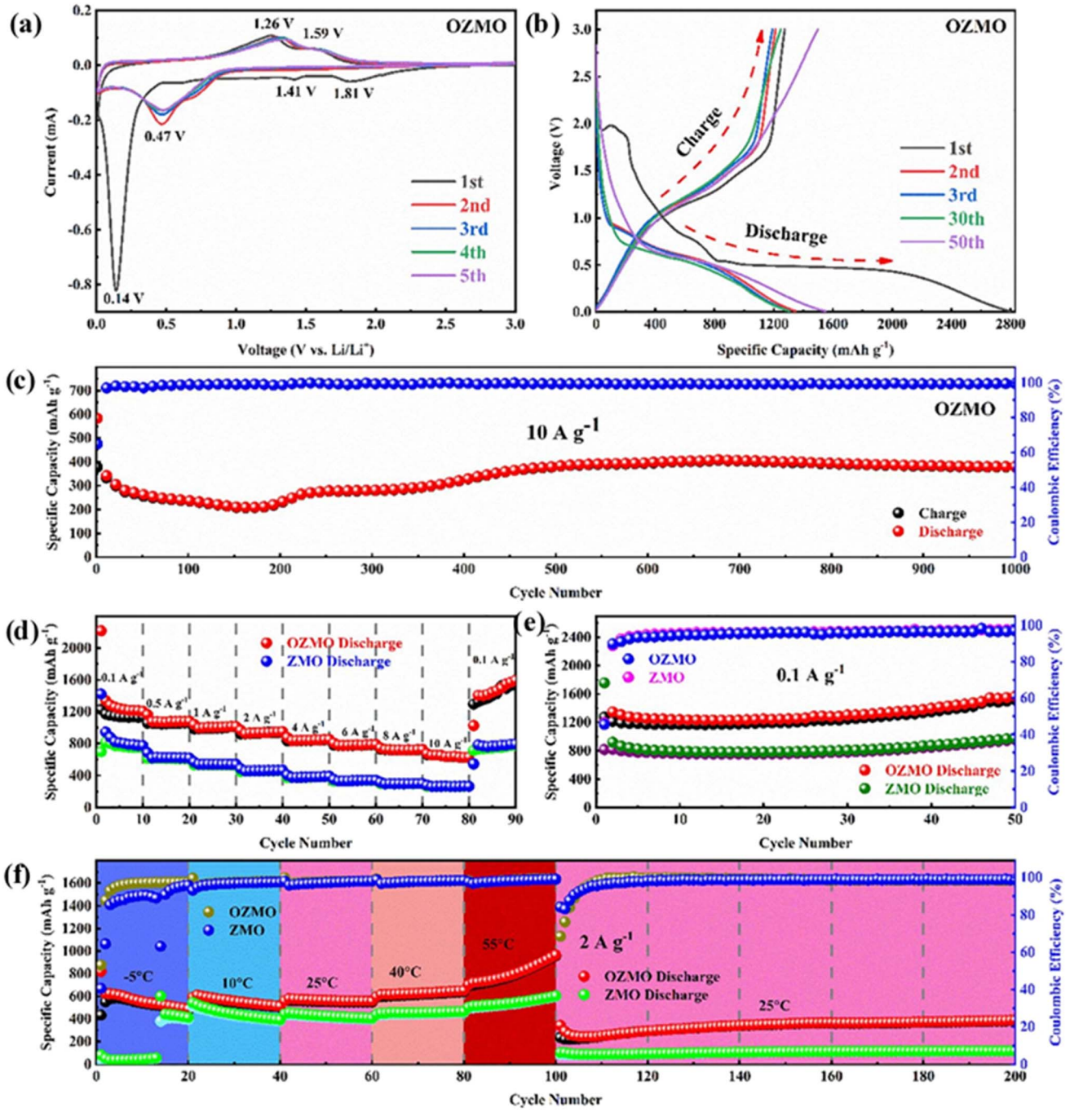

Fig. 10 (a) CV of OZMO at a scan rate of 0.2 mV s^{-1}; (b) GCD profile of the OZMO electrodes at 0.1 A g^{-1}; (c) cycling stability of OZMO at 10 A g^{-1}; (d) rate performance of the OZMO and ZMO electrodes at 0.1–10 A g^{-1}; (e) cycling stability of the OZMO and ZMO electrodes at 0.1 A g^{-1}; (f) high/low-temperature performance at 2 A g^{-1}. Reproduced from ref. 105 with permission from Elsevier, copyright 2021.

synthesized three types of ZMOs with varying initial charge capacities and coulombic efficiencies. The relatively low initial coulombic efficiencies were attributed to SEI formation and incomplete ZMO oxidation. However, the specific capacity improved in subsequent cycles due to self-optimization of the active materials, the formation of a polymer gel-like film, and increased electrolyte wetting.

Combining ZMO with other active materials can create hybrid nanostructures with improved electrochemical performance. Jiu *et al.*[64] introduced $Mo_6S_{9.5}$ ultra-thin nanosheets on the outer layer of ZMO spheres, forming ZMO@$Mo_6S_{9.5}$ hierarchical mesoporous micro-flowers (HMMs). These HMMs exhibited high initial discharge and charge capacities (1203 and 846 mA h g^{-1}, respectively) and a reversible capacity of 731 mA h g^{-1} after high-current cycling. This good performance was attributed to the 3D hierarchical architecture and the synergistic interaction between $Mo_6S_{9.5}$ and ZMO.

6.1.2 Composite design of ZMO. To address the inherent low electronic conductivity of ZMO, researchers have investigated compositing it with conductive carbon materials. This approach enhances electrical contact, prevents exfoliation from the current collector, and improves the overall conductivity and morphological stability of ZMO. A uniform dispersion of ZMO on carbon matrices also reduces agglomeration, which is particularly important at high charge/discharge rates. However, beyond improving electronic conductivity, the choice of carbon material plays a crucial role in influencing the initial coulombic efficiency (ICE) and solid electrolyte interphase (SEI) formation, both of which significantly impact the long-term performance of ZMO-based anodes. A high ICE is essential for maximizing the energy density of full cells, as low ICE leads to the irreversible consumption of active Li ions in the first cycle. Carbonaceous materials with high surface areas or abundant defects tend to form thick SEI layers, leading to excessive electrolyte decomposition and alkali-ion loss, thereby reducing the ICE. Hence, optimizing the pore structure, heteroatom doping, and surface functionalization of carbon materials in ZMO composites is critical for mitigating these effects.[144]

Yuan *et al.*[145] developed core–shell ZMO@CNT coaxial nanocables as an innovative anode material for LIBs. The 3D CNT network provided a flexible buffer to accommodate volume changes in ZMO during cycling, hindered ZMO nanosheet aggregation, and improved electron transport. These coaxial nanocables demonstrated a high initial discharge capacity (1033 mA h g^{-1}) and maintained a significant capacity of 652 mA h g^{-1} after 100 cycles.

Xiong *et al.*[146] proposed a facile two-step synthesis approach to address the challenges associated with ZMO anodes, specifically targeting improvements in capacity, rate capability, and cycling stability. Their method involved a polyol process followed by thermal annealing, resulting in a unique 2D architecture where ZMO nanoparticles were uniformly integrated onto rGO sheets. This structure significantly enhanced the electrochemical performance, achieving a specific capacity of approximately 650 mA h g^{-1} over 1500 cycles at a high current density of 2000 mA g^{-1}. This improved performance was attributed to the synergistic combination of ZMO and rGO. The 2D architecture increased the electrochemically active surface area, facilitating lithium-ion intercalation and deintercalation. It also shortened Li^+ diffusion pathways, improving charge and discharge rates. The flexible rGO sheets provided structural support for the ZMO nanoparticles, accommodating volume changes during cycling. Furthermore, thermal annealing enhanced crystallinity and stability.

Zhang *et al.*[147] addressed the limitations of ZMO by using CMK-3, a conductive carbon source, to create a ZMO@CMK-3 hybrid with a high surface area (129 m^2 g^{-1}). This composite exhibited a high reversible capacity (997 mA h g^{-1} at 100 mA g^{-1} after 100 cycles), good rate capability, and exceptional cycling performance (94% capacity retention over 1600 cycles). The robust structural integrity of the composite, with its rod-like morphology and mesoporous structure, contributed to its excellent cycling stability. The growing interest in biomass as an advanced energy material has led to the development of biotemplate techniques for creating controlled nano- and microstructures. Natural materials offer unique advantages due to their intricate hierarchical morphologies and porous structures. In this context, Chen *et al.*[59] developed a ZMO/carbon composite using residual broken microalgae as a cost-effective carbon source. The resulting composite, with its hierarchical porous architecture and nanocapsule-like structure, demonstrated remarkable electrochemical performance, including high reversible capacity and excellent capacity retention, even at high current densities. This was attributed to the synergistic effects of carbon and a novel binder derived from sea algae. Similar to the low-cost carbon source approach, Lin *et al.*[60] synthesized a ZMO/carbon composite with milk as a carbon source. The milk-derived carbon was co-doped with heteroatoms (N, P, B, Ni, and S), enhancing conductivity and increasing the density of the carbon material. This co-doping strategy synergistically improved the capacity, cycling performance, and mechanical properties of the composite. The ZMO/milk-derived carbon hybrid achieved a high reversible capacity (1352 mA h g^{-1} after 400 cycles) and sustained long-term cyclability. These studies highlight the potential of utilizing natural resources and harnessing their synergistic effects to develop high-performance battery materials.

Besides carbon composites, carbon coatings have proven to be an effective strategy for enhancing the electrochemical performance of ZMO anodes by improving conductivity and stabilizing the electrode structure. A study on carbon-coated ZMO demonstrated that the carbon layer suppresses electrode polarization, reduces capacity fluctuations, and enhances rate capability. The coating prevents excessive SEI growth and phase transitions, particularly stabilizing the MnO phase and mitigating the formation of unwanted Mn_3O_4,[148] which contributes to long-term cycling stability. Besides carbon, metal oxide coatings like Al_2O_3 have also been explored for ZMO, offering further protection against electrolyte decomposition and HF-induced corrosion, as well as improved SEI stability.[149] Various coating materials, including TiO_2, ZnO, and Li_3PO_4, have been successfully applied to different anodes, demonstrating the potential to mitigate structural degradation and enhance Li-ion transport. Exploring new coating strategies

tailored for ZMO anodes could further optimize their performance, paving the way for more durable and high-capacity lithium-ion batteries.[150]

6.1.3 Electrolyte design and optimization. While much research has focused on ZMO synthesis and morphology control, understanding the impact of electrolyte formulations on ZMO's electrochemical behavior is also crucial. Kumar *et al.*[35] explored ZMO performance with different electrolyte combinations, finding that lithium bis(trifluoromethanesulfonyl)imide (LiTFSI) in ethylene carbonate and dimethyl carbonate (EC-DMC) yielded the highest initial capacity (649 mA h g^{-1}) and best cycling stability. This highlights the importance of efficient ion desolvation for rapid charge-transfer reactions in conversion-type materials like ZMO. LiTFSI and ether-based electrolytes are typically preferred when ion–solvent co-intercalation is desired, owing to strong ion–solvent interactions. Efficient desolvation of ions is crucial for rapid charge-transfer reactions at the electrode–electrolyte interface, particularly in conversion-type materials such as ZMO.

Despite the progress in ZMO research, a notable study by Zhang *et al.*[81] demonstrated exceptional performance with porous ZMO with a core–shell microsphere morphology. This material achieved a remarkably high specific capacity of 1600 mA h g^{-1} after 100 cycles and excellent rate performance, maintaining a capacity of 1208 mA h g^{-1} after 250 cycles at 500 mA g^{-1}. This exceeded the theoretical capacity, likely due to the partially reversible $Mn^{2+} \leftrightarrow Mn^{3+}$ redox process and interfacial lithium storage within the SEI layer.[82,146] While the mechanism for this capacity increase has been identified, further research is needed to understand the specific factors related to ZMO morphology and electrolyte that favor this mechanism. Table 6 presents a summary of electrochemical characterization data for ZMO used as an anode material in LIBs, drawn from selected reports. Although ZMO offers promising characteristics as an anode material for LIBs, it also presents certain challenges. Table 7 summarizes these challenges and the modification strategies employed to overcome them, highlighting the resulting benefits.

Table 6 Electrochemical characterization of ZMO anodes in LIBs from selected reports

Synthesis	Morphology	Specific capacity (mA h g^{-1})	Capacity retention (cycles)	Ref.
Solvothermal	Ball-in-ball	1094 at 0.1 A g^{-1}	70% (250) at 0.5 A g^{-1}	77
	Microspheres	800 at 0.5 A g^{-1}	~44% (300) at 0.5 A g^{-1}	65
	Pomogranate-like	596 at 1 A g^{-1}	~91% (100) at 2 A g^{-1}	78
	Multi-shell hollow	537 at 0.4 A g^{-1}	~100% (150) at 0.4 A g^{-1}	39
Hydrothermal	Hollow spheres	1207 at 0.78 A g^{-1}	78% (565) at 0.78 A g^{-1}	66
	Nanowires	869 at 0.5 A g^{-1}	~84% (50) at 0.5 A g^{-1}	53
	Microspheres	723 at 0.4 A g^{-1}	~84% (350) at 0.4 A g^{-1}	68
	Peanut-like	812 at 0.1 A g^{-1}	~90% (200) at 0.1 A g^{-1}	70
	Hierarchical porous rugby-balls	1584 at 0.1 A g^{-1}	41.3% (100) at 0.1 A g^{-1}	55
	Porous rod-like structure	702 at 1.58 A g^{-1}	~70% (1000) at 1.568 A g^{-1}	151
	Hierarchical mesoporous microflowers	731 at 0.1 A g^{-1}	~100% (100) at 0.1 A g^{-1}	64
	Nanosheets@carbon nanotubes	1033 at 1.2 A g^{-1}	~55% (100) at 1.224 A g^{-1}	145
	Sphere-like shape in a porous carbon matrix	399 at 1 A g^{-1}	60% (400) at 0.1 A g^{-1}	60
Sol–gel	Nanoparticles	874 at 0.1 A g^{-1}	67% (100) at 1 A g^{-1}	35
	Nanoblocks	110 at 1 A g^{-1}	~33% (40) at 0.1 A g^{-1}	62
Polyol	ZMO–graphene	800 at 0.5 A g^{-1}	81% (1500) at 2 A g^{-1}	146
	Ball-in-ball	683 at 0.6 A g^{-1}	~83% (120) at 0.4 A g^{-1}	67
Coprecipitation	Microspheres	999 at 0.1 A g^{-1}	99.2% (50) at 0.1 A g^{-1}	82
	Hollow microrods	379 at 1 A g^{-1}	133% (302) at 0.5 A g^{-1}	85
	Nanorods	270 at 0.1 A g^{-1}	75% (200) at 0.2 A g^{-1}	106
	O deficient nanorods	1566 at 0.1 A g^{-1}	~100% (50) at 0.1 A g^{-1}	105
	Nanoparticles	638 at 1 A g^{-1}	~61% (300) at 1 A g^{-1}	35
Solution immersion	ZMO@carbon aerogel	833 at 0.1 A g^{-1}	~88% (50) at 0.1 A g^{-1}	98
Micro emulsion	Microspheres	870 at 0.1 A g^{-1}	158% (250) at 0.5 A g^{-1}	81
Carbongel combustion and hard template	Hollow porous panpipe	458.7 at 1 A g^{-1}	70% (500) at 0.5 A g^{-1}	108
Electrospun	Nanofibers	428 at 1 A g^{-1}	47.3% (60) at 0.05 A g^{-1}	32
Microwave	Micro-rhombus	1057 at 1 A g^{-1}	~30% (40) at 0.1 A g^{-1}	152
Reactive template	Tubular array	1198 at 0.1 A g^{-1}	~66% (100) at 0.1 A g^{-1}	37
Template synthesis	Porous 3D interconnected carbon framework	760 at 0.1 A g^{-1}	~55% (550) at 1 A g^{-1}	102
	2D-on-3D architecture	693 at 2 A g^{-1}	94% (1600) at 2 A g^{-1}	147
Biotemplating method	Microspheres	1450 at 0.2 A g^{-1}	750% (250) at 1 A g^{-1}	59
Polymer pyrolysis	Nanocystals	766 at 0.1 A g^{-1}	~75% (50) at 0.1 A g^{-1}	31
Biomorphic route	Microbelt	738 at 0.2 A g^{-1}	~95% (300) at 2 A g^{-1}	95

Table 7 Strategies to overcome challenges in ZMO anodes for LIBs

Challenge	Modification strategy	Key benefits
Low electrical conductivity	- Composite with conductive materials (CNTs, graphene, *etc.*)	- Enhanced charge transfer
	- Derived carbon with heteroatom co-doping	- Improved rate capability
	- Oxygen vacancy engineering	- Increased capacity
Volume changes during cycling	- Nanostructured ZMO	- Accommodate volume expansion/contraction
	- Porous/hollow architectures ("ball-in-ball," microtubules, core–shell, *etc.*)	- Maintain structural integrity
	- Control of calcination temperature and the annealing ramp rate	- Improve cycling stability
Electrolyte limitations	- Optimize Li-based electrolytes (LiTFSI in EC-DMC)	- Enhance ion desolvation - Improve ionic conductivity - Improve cycling stability

6.2 ZMO in SIBs

SIBs have emerged as a potential alternative to LIBs, particularly for large-scale energy storage applications such as grids, due to the abundance and low cost of sodium. However, the larger ionic radius of Na ions (0.102 nm, about 50% larger than that of Li-ions) makes it challenging to use commonly used anode materials of LIBs with SIB anodes. ZMO has also been widely studied in SIBs due to its environmental friendliness, energy efficiency, and low cost. Although fewer studies have explored its application in SIBs, some progress has been made in this area. The reaction mechanism of ZMO with Na in SIBs based on the study by Chandra Sekhar *et al.*[153] is as follows:

$$ZnMn_2O_4 + 8Na^+ + 8e^- \rightarrow 2Mn + Zn + 4Na_2O \quad (17)$$

$$2Mn + 2Na_2O \leftrightarrow 2MnO + 4Na^+ + 4e^- \quad (18)$$

$$Zn + Na_2O \rightarrow ZnO + 2Na^+ + 2e^- \quad (19)$$

The following reaction mechanism could also be valid for ZMO as a cathode in SIBs:[154]

$$ZnMn_2O_4 + Na^+ + e^- \rightarrow NaZnMn_2O_4 \quad (20)$$

$$NaZnMn_2O_4 + Na^+ + e^- \rightarrow ZnO + 2MnO + Na_2O \quad (21)$$

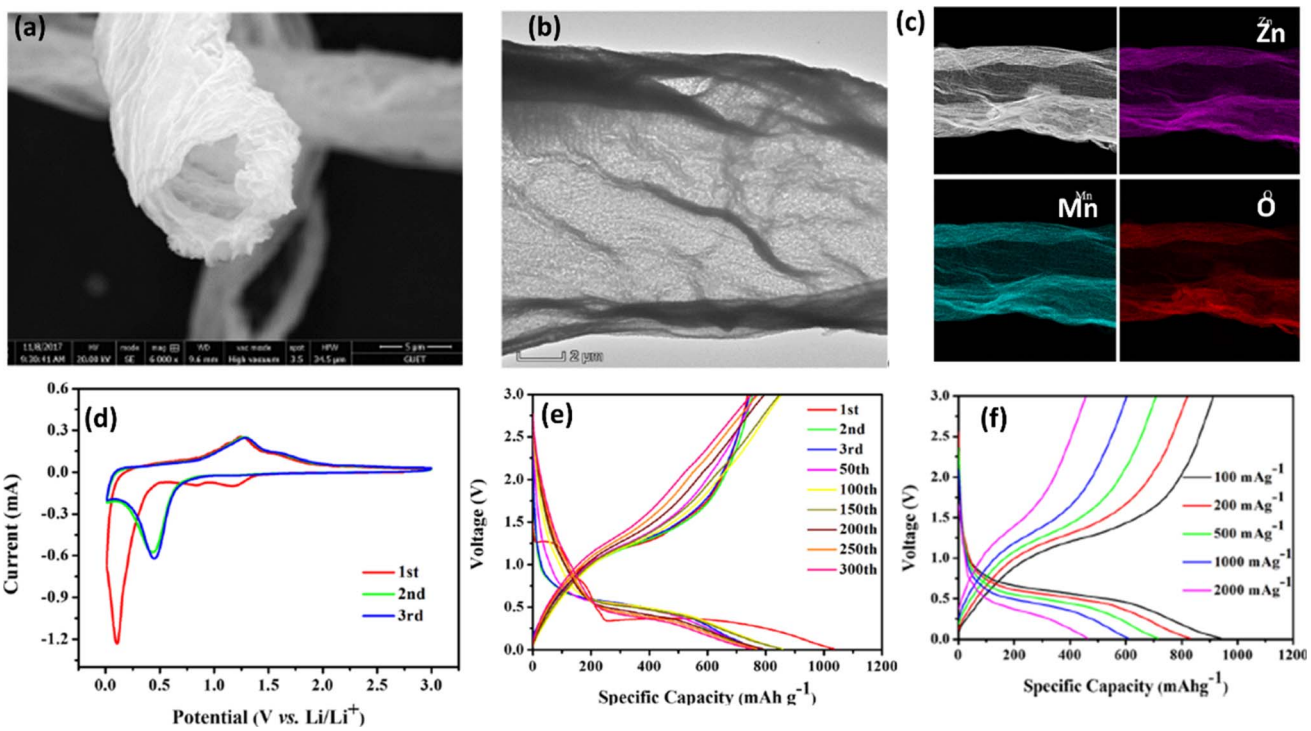

Fig. 11 ZMO microtubules (ZMO-MTs): (a) SEM image, (b) HR-TEM image, (c) elemental mapping, (d) CV curves at a scan rate of 0.1 mV s^{-1} within the voltage range of 0.01–3.0 V, (e) GCD profiles after different cycles, and (f) GCD profiles at various current densities ranging from 100 to 2000 mA g^{-1}. Reproduced from ref. 95 with permission from ACS, copyright 2018.

$$ZnO + xNa^+ + xe^- \leftrightarrow (1 - x)\,ZnO + xZn + xNa_2O \quad (1 > x > 0) \quad (22)$$

$$2MnO + yNa^+ + ye^- \leftrightarrow Mn_2O_3 + yNa_2O \quad (1 > y > 0) \quad (23)$$

Chandra Sekhar *et al.*[153] conducted the first study of ZMO as an anode for SIBs in 2017. A composite of ZMO and a nitrogen-doped graphene sheet anode was used in a half cell, exhibiting a high capacity of 170 mA h g^{-1} over 1000 cycles, with a rate capability of up to 10 A g^{-1}. The superior electrochemical performance was due to the synergistic effect produced by the presence of ZMO nanoparticles decorated with the sheets of nitrogen-doped graphene, the higher electrode conductivity, as well as maintained structural integrity and accommodated volume changes during cycling. Then, in 2020, Luo *et al.*[95] fabricated ZMO microtubules (ZMO-MTs) with an inner diameter of 8.5 μm and wall thickness of 1.5 μm, using a biomorphic approach. These microtubules were used as anodes for both SIBs and LIBs. ZMO-MT demonstrated a discharge capacity of 102 mA h g^{-1} after 300 cycles at 100 mA g^{-1} and a rate capability of 58 mA h g^{-1} at 2 A g^{-1} (Fig. 11). The exceptional electrochemical performance of ZMO-MT can be attributed to its distinctive one-dimensional mesoporous microtubular architecture. This architecture provides a large contact area between the electrolyte and electrode, as well as a short diffusion distance for both ions and electrons. As a result, it buffers the volume variation that arises from repeated cycling. In the context of LIBs, ZMO-MT demonstrated a capacity of 750 mA h g^{-1} after 300 cycles at 200 mA g^{-1}.

Defect engineering in transition metal oxides, particularly through the creation of oxygen vacancies, has emerged as a promising strategy to enhance the performance of SIBs. These vacancies, created by selectively removing oxygen atoms from the crystal lattice, enhance the material's electronic conductivity, provide additional sites for ion storage, and reduce the energy barriers for ion diffusion.[155–158] Cheng *et al.*[105] demonstrated this approach by synthesizing oxygen vacancy-enriched ZMO nanorods *via* a coprecipitation and chemical reduction process. By narrowing the bandgap, oxygen vacancies increase electrical conductivity and facilitate faster charge transfer. They also contribute to a more porous structure with a larger surface area, which improves the interaction between the electrolyte and the electrode, shortens diffusion distances for ions, and accommodates the volume changes that occur during sodium-ion insertion and extraction. These structural and electronic modifications also encourage a pseudocapacitive behavior, enabling the material to store more sodium ions and maintain stable performance over extended cycling. In another study on mitigating the volume changes and enhancing the conductivity of ZMO, Yu *et al.*[103] developed a composite material by anchoring submicron cubic ZMO onto a porous carbon framework derived from jute biomass through a mixed solvent thermal method. The three-dimensional porous structure of the jute-derived carbon significantly contributed to improving the composite's performance by enhancing its electronic conductivity. Additionally, this structure helped mitigate the mechanical stress caused by the volume changes of ZMO during Na^+ cycling. The interconnected pores within the carbon framework not only facilitated efficient ion diffusion but also increased the number of available sites for ion storage. Additionally, the composite's hierarchical design allowed for uniform particle dispersion, mitigating aggregation and preserving the structural integrity of the anode. These synergistic features enabled this composite to maintain a capacity of 244 mA h g^{-1} after 1500 cycles at a current density of 1 A g^{-1}. Further improvements were achieved by Muruganantham *et al.*,[154] who developed porous ZMO microspheres using a PVP-assisted ST method. The inclusion of PVP facilitated the formation of uniform microspheres with enhanced porosity, which not only promoted efficient Na^+ ion diffusion but also helped mitigate the volume changes during cycling. This porous microstructure, coupled with the reversible redox transitions between Mn^{3+}/Mn^{2+} and Zn^{2+} reduction, contributed significantly to the material's stable electrochemical performance. The controlled nanostructure design of these microspheres enhanced charge transfer and facilitated capacity retention over extended cycles, highlighting the critical role of structural engineering in improving the sodium-ion storage capabilities of ZMO anodes. Table 8 summarizes electrochemical characterization data for ZMO as an anode material in SIBs, based on selected studies.

6.3 ZMO in ZIBs

A study by Sousa *et al.*[159] used computer simulations to investigate ZMO as a potential material for batteries. They compared ZMO to a similar material used in LIBs, lithium manganese oxide (TLMO). While ZMO showed promise, the simulations revealed some drawbacks. Specifically, ZMO shrinks significantly when zinc ions are removed, suggesting it might not hold up well on repeated use. Also, ZMO lacks stable intermediate phases during the charge–discharge cycle, unlike TLMO. This could limit how much energy it can store. Despite these limitations, ZMO has other properties that make it attractive for energy storage. It could be useful in supercapacitors or SIBs, where the stability issues might be less important. However, to

Table 8 Electrochemical characterization of ZMO in SIBs from selected reports

Method	Morphology	Specific capacity (mA h g^{-1})	Capacity retention (cycles)	Ref.
Hydrothermal	Nanoflakes	425 at 0.05 A g^{-1}	68% (150) at 0.05 A g^{-1}	153
PVP-assisted solvothermal	Mesoporous	112 at 0.2 A g^{-1}	—	154
Biomorphic approach	Mesoporous microtubules	~58 at 2 A g^{-1}	88% (300) at 0.2 A g^{-1}	95
Coprecipitation/chemical reduction	Nanorods	266 at 0.1 A g^{-1}	81% (200) at 0.2 A g^{-1}	105
Microemulsion	Submicron cubic	392 at 0.1 A g^{-1}	81% (150) at 1 A g^{-1}	103

make ZMO a viable option for ZIBs, further research is needed to improve its stability.

Rechargeable ZIBs are considered to be promising next-generation batteries because metallic Zn is stable in water and can undergo a reversible stripping/plating reaction in mild acidic aqueous electrolytes allowing for the use of metallic Zn as the anode in ZIBs.[160] In addition, Zn has the merits of high natural abundance, low redox potential (−0.76 V *vs.* the standard hydrogen electrode), and high theoretical specific capacity (820 mA h g^{-1}). Unfortunately, compared with the large theoretical specific capacity of the zinc negative electrode, the reported capacity of positive electrode materials is still low, and the cycling stability also needs to be further improved. Considering the success of $LiMn_2O_4$ as one of the main lithium cathode materials and the close ionic radius of Zn^{2+} and Li^+ (0.06 *vs.* 0.059 nm), ZMO is a plausible candidate for a cathode material in aqueous ZIBs. Extensive research has been conducted on ZMO and it has shown promise as a positive material for ZIBs due to its low cost, a high average working potential of 1.35 V,[80] large theoretical capacity (224 mA h g^{-1}), and high redox potential (Fig. 12).[161] Throughout the charging process, Zn ions are gradually removed from the tetrahedral positions of the ZMO cathode. This causes the oxidation of Mn^{3+} to Mn^{4+} and results in the formation of MnO_2, which then releases two electrons. In contrast, during the discharge process, Zn ions are present on the surface of the zinc anode and capture two electrons. This results in a reversible reaction during the (dis) charging processes, respectively. To summarize, the corresponding electrochemical reactions occur as follows:[162]

$$\text{Cathode: } ZnMn_2O_4 \leftrightarrow Zn_{1-x}Mn_2O_4 + 2xe^- + xZn^{2+} \quad (24)$$

$$\text{Anode: } xZn^{2+} + 2xe^- \leftrightarrow xZn \quad (25)$$

$$\text{Full cell (overall): } ZnMn_2O_4 \leftrightarrow Zn_{1-x}Mn_2O_4 + xZn \quad (26)$$

Despite the promising advantages of ZMO as a cathode material, several challenges hinder its practical

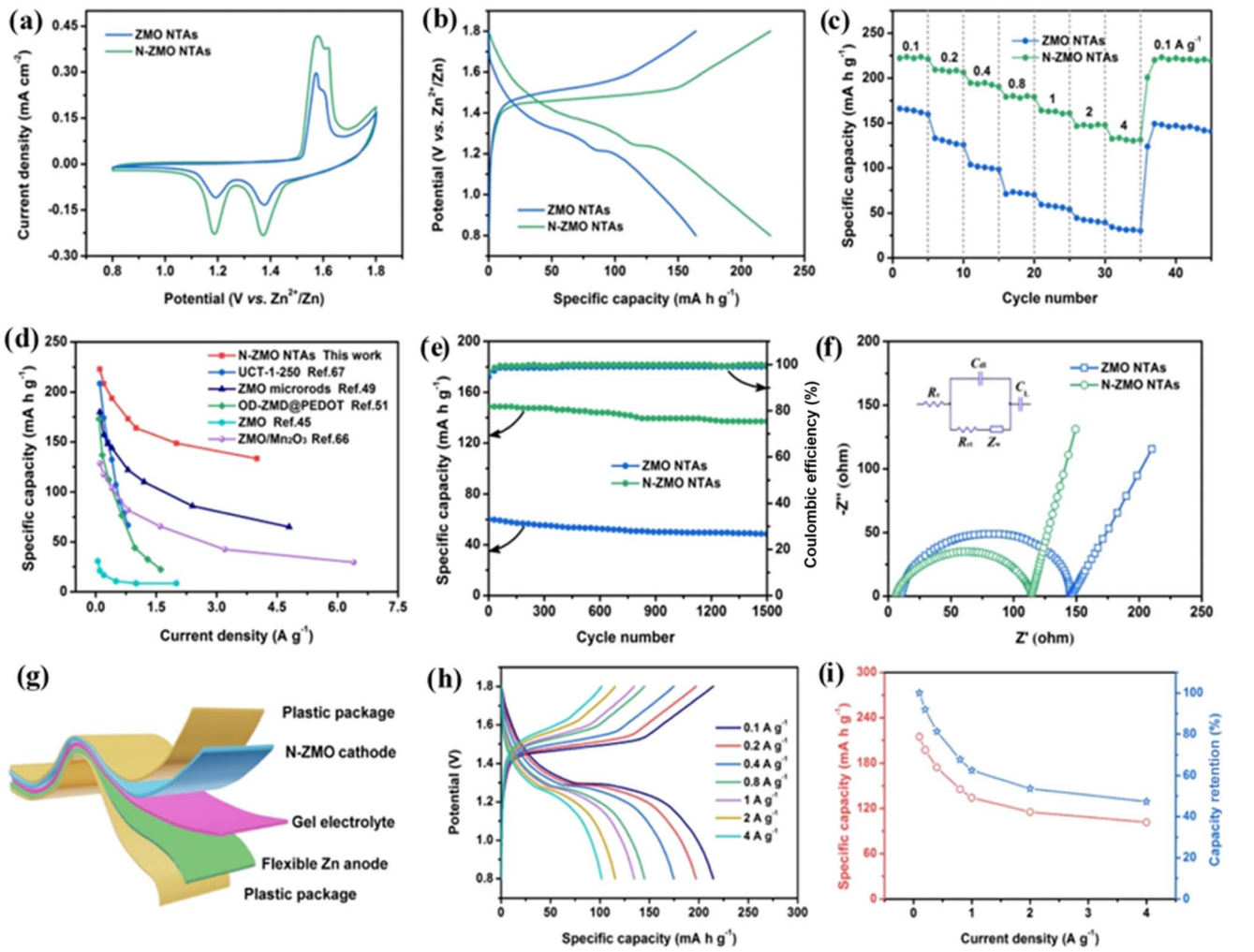

Fig. 12 Electrochemical performance of ZMO NTAs and N-ZMO NTAs: (a) CV results; (b) GCD curves; (c) evaluation of rate capability; (d) capacity performance comparison with previously reported ZMO cathodes; (e) cycling durability; (f) Nyquist impedance plots of ZMO and N-ZMO NTA electrodes. Electrochemical analysis of the quasi-solid-state N-ZMO//Zn full cell device: (g) schematic representation; (h) charge–discharge curves; (i) rate performance assessment. Reproduced from ref. 162 with permission from Elsevier, copyright 2021.

implementation. Firstly, irreversible structural transformations and Mn^{3+} disproportionation reactions induce capacity degradation during cycling. Secondly, strong electrostatic interactions between the host crystal and Zn ions limit the realization of high-capacity ZIBs. Thirdly, the inherently low electrical conductivity of ZMO ($\sim 1.0 \times 10^{-5}$ S cm^{-1}) restricts cycle life, particularly at high rates. Finally, limited active site accessibility and significant volume changes impede rate performance and

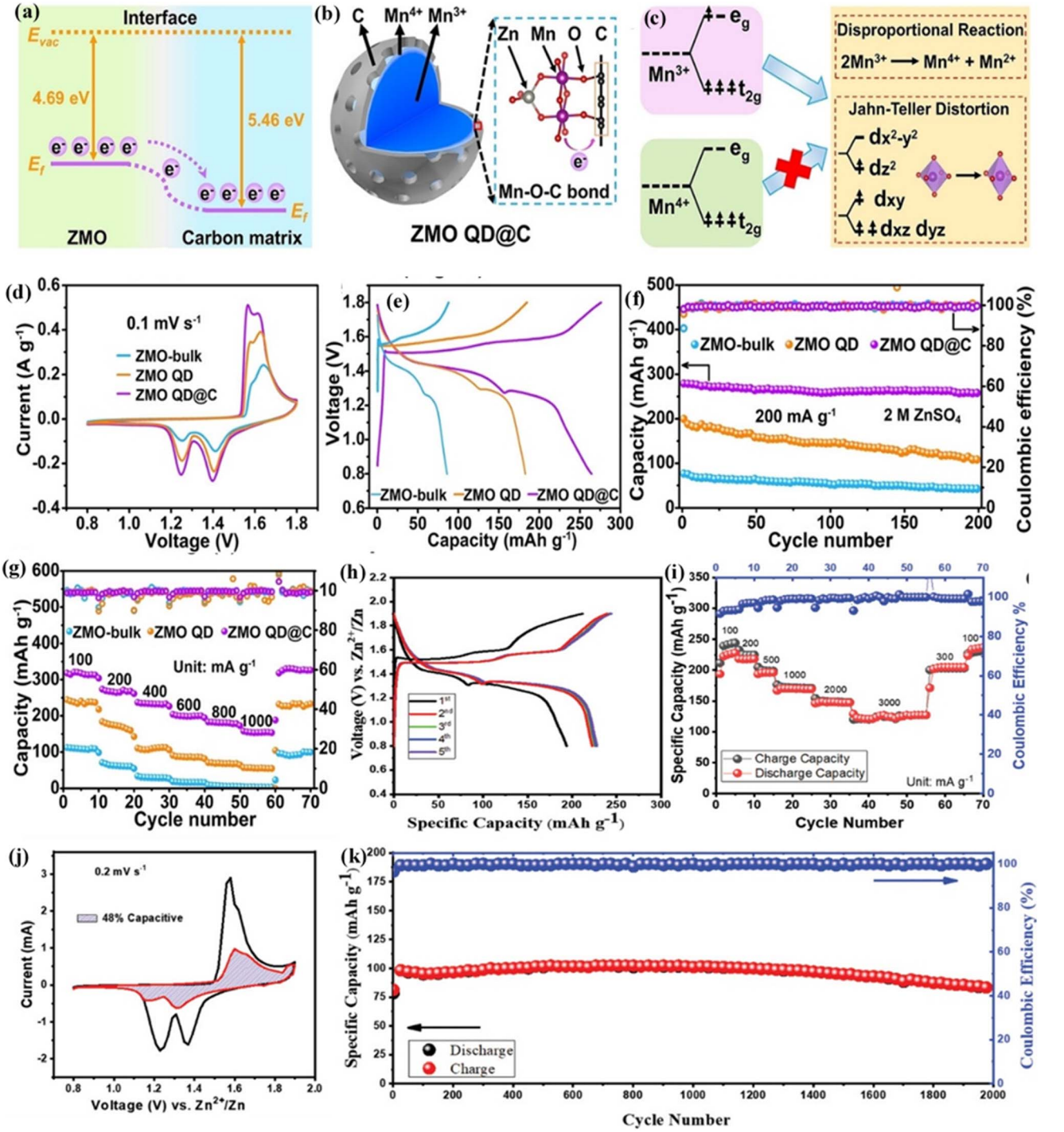

Fig. 13 (a) Illustration of charge-transfer mechanisms at the interface between ZMO and the carbon matrix in ZMO QD@C; (b) analysis of the Mn valence state distribution in ZMO QD@C; (c) depiction of the structural stability mechanism in ZMO QD@C; (d) CV curves recorded at a scan rate of 0.1 mV s^{-1}; (e) charge–discharge profiles at a current density of 200 mA g^{-1}; (f) cycling performance at 200 mA g^{-1}; (g) rate performance. Reproduced from ref. 109 with permission from Wiley Online Library, copyright 2022. Electrochemical evaluation of the ZnO–MnO@C electrode: (h) charge–discharge curves at 100 mA g^{-1} within the voltage range of 0.8–1.9 V; (i) rate performance at various current densities; (j) capacitive contribution integrated within the CV curve; (k) cycling performance at a high current density of 1000 mA g^{-1}. Reproduced from ref. 164 with permission from Wiley Online Library, copyright 2021.

long-term stability, resulting in suboptimal ZMO//Zn battery performance. Consequently, research efforts are focused on developing novel ZMO-based cathodes with enhanced intrinsic conductivity and structural stability. The following sections provide a comprehensive review of advancements in both aqueous and organic ZIBs.

6.3.1 Aqueous electrolytes

6.3.1.1 Mn dissolution and conductive additives. The primary cause of capacity fading in ZMO is the disproportionation reaction of Mn^{3+}, driven by its unstable orbital configuration, which induces Jahn–Teller distortion and promotes its dissolution in the aqueous electrolyte. This reaction predominantly transpires at the electrode/electrolyte contact and is represented by using the following eqn (27):

$$2Mn^{3+} + 3H_2O \rightarrow Mn^{2+}(aq) + MnO_2(s) + 4H^+ \quad (27)$$

In this process, Mn^{3+} is converted into Mn^{2+} and Mn^{4+}, with Mn^{2+} diffusing into the electrolyte and Mn^{4+} precipitating as MnO_2 on the electrode surface.[163]

There are proven methods for suppressing Mn dissolution including the use of highly concentrated colloidal electrolytes, the strategic inclusion of preinserted cations, and carbon protective layer coating for Mn-based cathodes.[107] In particular, the use of Mn^{2+} as an electrolyte additive has been an effective way to prolong cycle life. Soundharrajan *et al.*[80] added 0.1 M $MnSO_4$ in 1 M $ZnSO_4$ electrolyte, which suppressed the release of Mn^{2+} from Mn^{3+} disproportion reactions by providing a dynamic equilibrium between the Mn^{2+} suspension and the following oxidation of Mn^{2+} in the electrolyte. Although there are many reports that use $MnSO_4$ as an electrolyte additive, Deng *et al.* implied that the use of $MnSO_4$ overestimates the performance of the Mn oxide-based cathode, and Mn oxide will undergo phase transformation, as Mn^{2+} can be electro-oxidized into active MnO_x during the charge operations. The Jahn–Teller effect and Mn^{3+} disproportionation in Mn oxide cathodes often cause irreversible structural changes and Mn^{2+} dissolution, compromising cycling stability. Deng *et al.*[109] introduced ZMO quantum dots into a porous carbon framework, forming Mn–O–C bonds at the interface. These bonds effectively suppress the Jahn–Teller effect and Mn dissolution, leading to enhanced electrochemical performance (Fig. 13(a–g)). Islam *et al.*[164] also investigated the structural changes during electrochemical studies through *in situ* XRD analysis and observed that there is a new phase formation of $ZnMn_3O_7 \cdot 3H_2O$ from the reaction of the Mn^{2+} additive and $Zn_4(OH)_6SO_4 \cdot xH_2O$ during the charging process. The remaining Mn^{2+} ions deposit as MnO_x on the electrode surface. Thus, in addition to the intercalation of Zn^{2+}, a combination of both conversion and deposition of Mn^{2+} increases the capacitance of the cell (Fig. 13(h–k)).

To improve the stability of ZMO, a prevalent strategy is to substitute Mn^{3+} with other elements to eradicate its dissolving source. Dopants such as Fe^{2+}, Mg^{2+}, or Cu^{2+}, incorporated into the ZMO structure, convert Mn^{3+} into Mn^{4+} to uphold charge neutrality, thereby diminishing Mn dissolution.[165–167] Hawari *et al.*[168] added an iron (Fe) precursor during synthesis and obtained the $Zn_{0.5}Mn_{0.5}Fe_2O_4$ phase within ZMO forming heterostructures which had a similar effect of mitigating the disproportionation reaction of Mn^{3+}. Kang *et al.*[163] illustrated the efficacy of this method by synthesizing $ZnMn_{2-x}Ni_xO_4$ samples (x = 0, 0.5, 1.0, and 1.5), noting a transition from a tetragonal to cubic spinel structure for all Ni doping concentrations. Following 100 activation cycles, the ICP measurements of the Zn anode indicated that Ni concentration negatively correlates with Mn deposition, implying that elevated Ni levels markedly diminish Mn accumulation. Ni-doped ZMO surpassed the theoretical capacity of ZMO (224 mA h g^{-1}) and attained 277–278 mA h g^{-1}. Furthermore, Ni-doped ZMO retained 80% of its capacity after 1000 cycles.

CNTs, as carbon conductive materials, offer numerous advantages, including a large surface area, high electrical conductivity, and efficient electrolyte channels. Chen *et al.*[169] utilized these properties by compositing CNTs with ZMO/C hollow microspheres as a cathode material for ZIBs. In addition to the rate performance, cyclability was also improved due to the hollow mesoporous microsphere structure's ability to buffer volume expansion caused by Zn ion (de)intercalation. Similarly, Gao *et al.*[143] synthesized 20 nm ZMO particles on CNTs which again increased the cyclability and rate performance. Along with the CNTs' advantages, the smaller particle size contributed to a shorter ion diffusion path and the strong interface interaction of Mn–O–C buffers the structural degradation. There are additional reports on using graphene and porous carbon with ZMO for increasing the electrical conductivity of the cathode.[170] Instead of using costly conductive agents, Li *et al.*[171] came up with a one-step solution combustion method to directly grow porous ZMO on carbon cloth, creating binder-free porous electrodes. The resulting electrodes demonstrated fast electrochemical kinetics, with an impressive 1st discharge-specific capacity of 281 mA h g^{-1} at 100 mA g^{-1}, making them ideal for rapid charge/discharge applications.

6.3.1.2 Electrolyte optimization and cation-deficient structures. Although the inclusion of Mn^{2+} does not affect the solubility of $ZnSO_4$, Soundharrajan *et al.* reported that Mn^{2+} enhances capacity through the electro-deposition and dissolution of MnO_x on the electrode surface, enabling the subsequent insertion and de-insertion of Zn-ions from the deposited MnO_x.[80] In addition to the primary charge storage mechanism involving reversible Zn^{2+} intercalation/deintercalation within the ZMO spinel structure itself,[33,107,171] which contains Mn in mixed oxidation states, a surface phase of MnO_x is formed through the electro-deposition of Mn^{2+} from the electrolyte.[80] Studies have provided direct evidence for Zn^{2+} insertion into the ZMO lattice through techniques such as XRD and XPS.[107,171] While proton insertion in ZMO cathodes might be overlooked in some studies, reversible proton insertion into the electrodeposited MnO_x layer could contribute to additional capacity.[172] It's plausible that both Zn^{2+} intercalation in ZMO and proton insertion in MnO_x contribute to the overall charge storage. Mn^{2+} plays a key role in the mildly acidic electrolyte by stabilizing the Mn oxidation states, suppressing Mn dissolution, and facilitating Zn^{2+} intercalation, potentially both directly into ZMO and indirectly through the MnO_x deposition/dissolution cycle.[80,173] Furthermore, acidity can improve

electrochemical reversibility by facilitating proton-assisted intercalation/de-intercalation of ions into the cathode. Under mildly acidic conditions, protons aid charge compensation, reducing polarization and improving reaction kinetics.[173] The presence of H^+ ions can also contribute to the formation of a stable MnO_x layer, enhancing redox activity and supporting long-term structural stability.[80,173] However, excess acidity can accelerate H_2 evolution and induce parasitic reactions at the anode, leading to Zn corrosion and a decline in coulombic efficiency.[173] Maintaining an optimal pH balance is therefore essential for ZMO cathodes, as it ensures efficient Zn^{2+} storage within the ZMO structure and potentially the MnO_x layer, mitigates Mn dissolution, and supports long-term cycling stability.[172,173]

Strong acidic electrolytes cause H_2 evolution, while alkaline KOH electrolytes exhibit high polarization, limiting cyclability. Mild acidic solutions with zinc salts ($ZnCl_2$, $Zn(NO_3)_2$, $ZnSO_4$ and $Zn(CF_3SO_3)_2$) were investigated. $ZnCl_2$ and $Zn(NO_3)_2$ electrolytes suffer from Cl^- and NO^{3-} instability. Although both $ZnSO_4$, and $Zn(CF_3SO_3)_2$ have wide electrochemical stability windows, $Zn(CF_3SO_3)_2$ demonstrated superior performance with a high current response, low overpotential, and enhanced stability at high currents in stripping/plating experiments. This indicates improved reversibility and faster Zn deposition/dissolution kinetics with $Zn(CF_3SO_3)_2$. Liu and colleagues[174] investigated the impact of different valence ions (*e.g.*, Na^+, Mg^{2+}, and Al^{3+}) as electrolyte additives to impede zinc corrosion and dendrite growth. The presence of Na^+ ions was found to effectively restrict zinc dendrite growth due to its high adsorption energy of approximately −0.39 eV, prolonging the duration of zinc dendrite formation to 500 h. Furthermore, they also applied a polyaniline (PANI) coating on ZMO cathode materials, resulting in a narrow band gap of around 0.097 eV, thereby enhancing the kinetics of charge transfer.

The ideal spinel structure presents challenges for ZIB cathodes due to poor Zn^{2+} diffusion caused by electrostatic repulsion within the lattice.[175] To enhance diffusion, cation-deficient structures are employed, reducing repulsion and providing vacancy-mediated transport pathways.[110,143,164] This strategy has been shown to improve Zn^{2+} ion diffusion in spinel structures. Galvanostatic intermittent titration technique (GITT) analysis revealed that Zn^{2+} ion diffusion coefficients in Mn-deficient

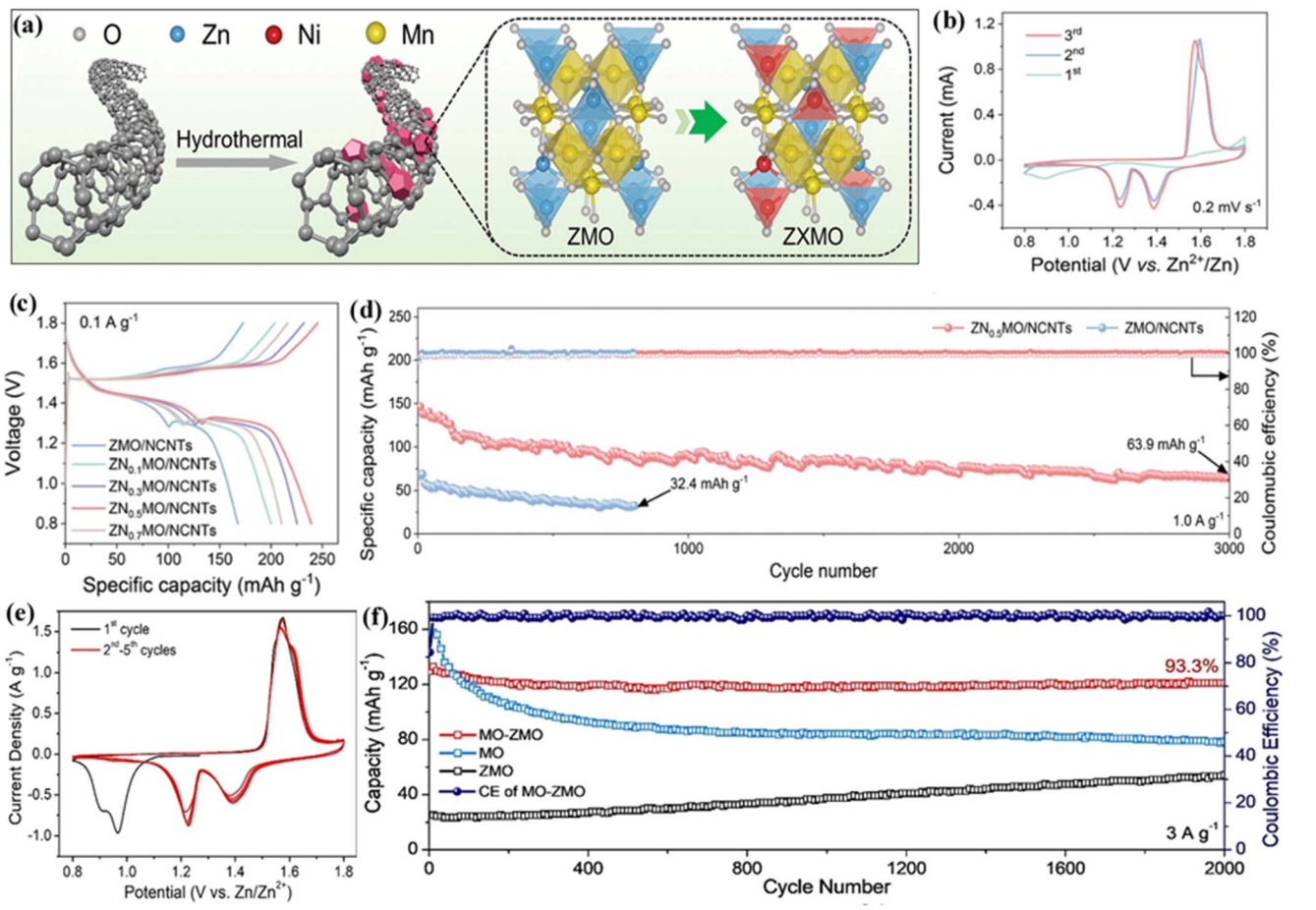

Fig. 14 (a) Diagram illustrating the synthesis process for ZMO/NCNTs and ZXMO/NCNTs; (b) CV curves of $ZN_{0.5}MO$/NCNTs during the first three cycles at a scan rate of 0.2 mV s^{-1}; (c) GCD profiles and (d) cycling stability comparison of ZMO/NCNTs and $ZN_{0.5}MO$/NCNTs at current densities of 0.2 and 1.0 A g^{-1}. Reproduced from ref. 177 with permission from Wiley Online Library, copyright 2024; (e) CV curves for the initial five cycles of the MO–ZMO HOs electrode at a scan rate of 0.2 mV s^{-1}; (f) long-term cycling performance of MO–ZMO HOs, MO HOs, and ZMO HOs electrodes at a current density of 3 A g^{-1}. Reproduced from ref. 61 with permission from Wiley Online Library, copyright 2021.

ZMO range from 10^{-9} to 10^{-11} cm^2 s^{-1}, significantly higher than the 10^{-13} cm^2 s^{-1} observed in pure ZMO. These Mn vacancies also hinder Mn^{3+} disproportionation into soluble Mn^{2+} by reducing Mn^{3+} concentration. Furthermore, Mn-deficient ZMO exhibits higher electronic conductivity compared to pure ZMO.[164]

Mallick *et al.*[176] synthesized defect-rich ZMO with Mn and Zn deficiencies and Ni doping, where Ni partially substituted Mn and Zn sites. This resulted in a cubic spinel structure, enhancing Zn^{2+} diffusion due to increased tunnel size. Ni doping transformed the semiconducting ZMO into a metallic one, improving electronic conductivity for Zn^{2+} ion storage. The introduction of Ni^{2+} led to the formation of stable $[MO_6]$ octahedra. Additionally, cationic doping promoted oxygen vacancies, further enhancing charge carrier mobility and electrical conductivity. These oxygen vacancies act as shallow donors, modifying the electronic configuration and increasing the specific capacity of the material. A high specific capacity of 265 mA h g^{-1} was achieved at 100 mA g^{-1}, with no capacity fading and a subsequent two-fold increase in the specific capacity noted after 5000 cycles.

In a similar vein, Wang *et al.*[177] employed a microstructure strain strategy, doping Ni into ZMO to enhance lattice stability for improved cycling performance. The introduction of Ni distorted the MnO_6 microstructure, creating asymmetrical pathways that facilitated Zn^{2+} ion transport and (de)intercalation. This led to enhanced reaction rates and structural reversibility. Temperature-dependent EIS spectral analysis using the Arrhenius equation revealed that Ni-doped ZMO exhibited lower activation energy and higher Zn^{2+} ion diffusion coefficients (confirmed *via* the GITT) compared to undoped ZMO. This demonstrates that Ni substitution facilitates the de-solvation of hydrated Zn ions, lowers the Zn ion transfer energy barrier, and improves ionic diffusion kinetics (Fig. 14(a–d)).

Yang *et al.*[33] and Yuan *et al.*[178] illustrated the advantages of sulfur doping in improving the efficacy of the ZMO material in ZIB applications. They demonstrated that the incorporation of sulfur into a ZMO/CNT composite enlarges the ZMO lattice and enhances Zn^{2+} ion transport. Strong Mn–S interactions, facilitated by electron density accumulation around Mn atoms, promote charge redistribution and improve structural stability. Density functional theory (DFT) simulations indicated that the Gibbs free energy for Zn^{2+}/H^+ adsorption near sulfur atoms in S-ZMO/CNT approaches thermal neutrality, signifying enhanced reversibility relative to undoped ZMO/CNT. Sulfur doping decreases the bandgap from 1.1844 eV to 0.7432 eV, enhancing electronic conductivity and diminishing Zn^{2+} interactions with the ZMO framework, leading to accelerated reaction kinetics, enhanced ion diffusion, facilitated desorption of adsorbed Zn^{2+}/H^+ ions, a greater electrochemically active surface area, and increased capacity.[71] Furthermore, Yuan *et al.*[178] performed theoretical and experimental investigations to enhance sulfur substitution in the ZMO lattice, based on the principle of minimizing electrostatic repulsion during Zn^{2+} diffusion leading to sluggish kinetics. Sulfur establishes covalent connections with Zn and Mn, resulting in charge density accumulation within these bonds and facilitating charge transfer between Zn/Mn and coordinating atoms. These modifications markedly enhance the electronic structure and stability of the material, further illustrating the substantial influence of sulfur on ZMO's electrochemical performance.

Wu *et al.*[107] investigated the influence of structural water in ZMO on Zn^{2+} intercalation energy barriers. Structural water plays a crucial role in Zn^{2+} insertion kinetics by (1) enlarging interlayer spacing and stabilizing the host material, (2) acting as a charge shield for metal ions, facilitating Zn^{2+} transport, and (3) lowering the Zn^{2+} diffusion energy barrier, promoting fast interfacial kinetics and preventing irreversible structural changes during cycling. This is supported by the calculated Zn^{2+} diffusivity in ZMO, which is significantly higher with structural water (1.51×10^{-11} cm^2 s^{-1}) compared to ZMO without structural water (8.99×10^{-13} cm^2 s^{-1}). This highlights the importance of considering structural water in the design of ZMO cathodes for enhanced performance.

6.3.1.3 ZMO-based composites and nanostructures. Although Mn_2O_3 offers high theoretical capacity, its practical application is limited by reversible phase transitions during cycling, leading to decreased cycle life. ZMO, though exhibiting lower capacity, maintains its spinel phase during cycling. To combine the advantages of both, Saadi-motaallegh *et al.*[179] synthesized a ZMO/Mn_2O_3 nanocomposite. By optimizing crystallite size and introducing Ni doping, they achieved a specific capacity of 235 mA h g^{-1} (0.2 A g^{-1}), exceeding that of the undoped nanocomposite (215 mA h g^{-1}). The Ni-doped nanocomposite also demonstrated superior capacity retention (91.32% after 3000 cycles at 2 A g^{-1}) compared to the undoped composite (64.54% retention under the same conditions). This improvement is attributed to enhanced conductivity and specific surface area facilitated by Ni^{2+} doping. Furthermore, the heterostructure formed at the ZMO/Mn_2O_3 interface creates a built-in electric field, accelerating interfacial reactions and charge transport. Similarly, Qin *et al.*,[180] utilized a CuO coating on ZMO to suppress Mn dissolution and improve cycle life. The CuO coating also actively contributes to Zn^{2+} storage through a conversion reaction mechanism, enhancing conductivity and capacity. Zeng *et al.*[61] utilized MOFs, known for their tunable structures and chemical versatility, as templates to synthesize Mn_2O_3–ZMO hollow octahedra. This strategy effectively tackled the challenges of limited cycling stability and rate capability in Mn-based oxides. The hollow architecture provided space to accommodate volume changes during Zn^{2+} insertion and extraction, preventing structural damage. Additionally, the synergistic effects at the Mn_2O_3–ZMO interface enhanced ion transport and facilitated highly reversible electrochemical reactions (Fig. 14(e and f)).

Very recently, Katsuyama *et al.*[181] developed 5 nm ZMO nanoparticles integrated with graphene, inhibiting nanoparticle aggregation and enabling a two-electron redox process. This resulted in a near-theoretical capacity of 406 mA h g^{-1} at 2000 mA g^{-1} and excellent rate performance. With a stoichiometrically equivalent zinc anode, the ZMO/G cathode achieved an energy density of 371 W h kg^{-1}, potentially reaching 504 W h kg^{-1} with increased active material loading, making ZIBs competitive with LIBs. This highlights the potential of ZIBs as

a cost-effective, safe, and environmentally friendly alternative to LIBs.

6.3.2 Organic/hybrid and quasi-solid-state electrolytes. Aqueous electrolytes are widely used in ZIBs, but they present challenges such as a narrow electrochemical stability window, a limited operating temperature range (0.0–100 °C), and cathode dissolution. Zinc anode corrosion, exacerbated by H_3O^+ ions and the self-ionization of water, further hinders performance. Dissolution of zinc salts lowers the pH, and Zn^{2+} interactions with water weaken O–H bonds, promoting hydrogen evolution and accelerating corrosion. To address these issues, "water-in-salt" electrolytes have been explored, confining water molecules and minimizing Zn^{2+}–H_2O interactions. Hybrid electrolytes, combining aqueous and organic components, offer another promising approach. For example, Wang *et al.*[182] demonstrated that polar solvents such as DMAC and TMP in a hybrid electrolyte enhance dipole–dipole interactions with water, stabilizing O–H bonds and mitigating zinc corrosion.

6.3.2.1 Organic and hybrid electrolytes. While organic electrolytes offer advantages such as a wider electrochemical stability window (ESW) and operational temperature range compared to aqueous electrolytes, they suffer from slow Zn^{2+} migration kinetics due to strong Coulomb interactions with the solvent. This limits charge/discharge capability. Although non-aqueous electrolytes can prevent water-induced side reactions, high desolvation energies and low ionic conductivity hinder reaction kinetics. Hybrid electrolytes have shown promise in mitigating these issues, improving Zn anode compatibility by suppressing hydrogen evolution and dendrite formation. However, research on hybrid electrolytes for ZMO cathodes remains limited.

Zhang *et al.*[110] pioneered the use of a 3 M $Zn(CF_3SO_3)_2$ acetonitrile–water hybrid electrolyte with a cation-deficient ZMO/C cathode, achieving a high reversible capacity (150 mA h g^{-1} at 50 mA g^{-1}) and excellent cycling stability. This performance is attributed to the synergistic effects of the cation-deficient ZMO and the $Zn(CF_3SO_3)_2$ electrolyte, which provides a wide ESW and high Zn plating/stripping efficiency (Fig. 15). Similarly, Cai *et al.*[183] demonstrated the effectiveness of 0.5 M $Zn(CF_3SO_3)_2$ in AN : H_2O (8 : 2) hybrid electrolyte with an Al-doped ZMO cathode. Al^{3+} doping increased the (101) crystal plane spacing, facilitating Zn^{2+} diffusion. Despite the relatively modest capacity compared to aqueous systems, organic/hybrid electrolytes offer improved thermodynamic stability and reduced dendrite formation, warranting further investigation for ZMO-based ZIBs.

6.3.2.2 Gel and quasi-solid-state electrolytes. Gel and quasi-solid electrolytes offer enhanced safety and are particularly suitable for flexible ZIBs. However, research has explored ZMO in solid-state or quasi-solid-state configurations using oxygen-deficient ZMO (OD-ZMO). Zhang *et al.*[34] fabricated the first quasi-solid-state ZIB using oxygen-deficient OD-ZMO which exhibited p-type semiconductor characteristics with increased carrier density. While Zn^{2+} diffusion in OD-ZMO was slightly lower than in pristine ZMO, DFT calculations revealed a lower energy barrier (0.24 eV) for Zn atom mobility near oxygen vacancies. OD-ZMO displayed a two-step intercalation process, attributed to H^+ and Zn^{2+} intercalation, leading to a higher capacity (174 mA h g^{-1}) compared to ZMO (98 mA h g^{-1}).

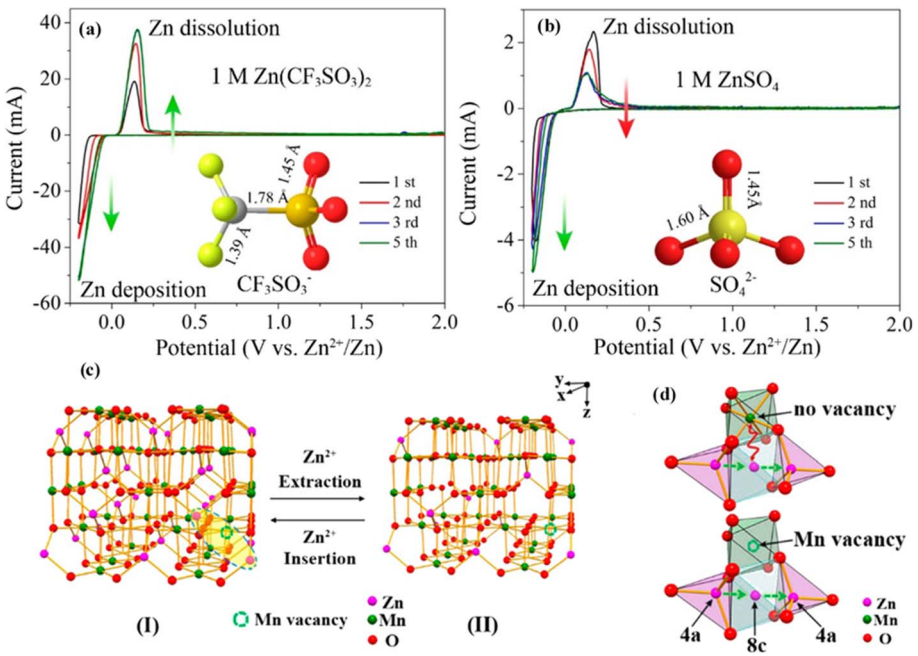

Fig. 15 (a) CV curves of the Zn electrode in an aqueous solution of 1 M $Zn(CF_3SO_3)_2$; (b) CV curves of the Zn electrode in 1 M $ZnSO_4$ solution, both obtained at a scan rate of 0.5 mV s^{-1} within the voltage range of −0.2 to 2.0 V; (c) schematic representation of Zn^{2+} insertion and extraction mechanisms in the extended three-dimensional ZMO spinel structure; (d) conceptual illustration of Zn^{2+} diffusion pathways in the ZMO spinel lattice, comparing scenarios with and without Mn vacancies. Reproduced from ref. 110 with permission from ACS, copyright 2016.

Table 9 Electrochemical performance of various ZMO-based cathodes for ZIBs

Material composition	Specific capacity (mA h g^{-1})	Capacity retention (cycles)	Reference
Zn/ZMO QD@C	320 at 0.1 A g^{-1}	86% (1500) at 1 A g^{-1}	109
ZMO/C	150 at 0.05 A g^{-1}	94% (500) at 0.5 A g^{-1}	110
$Zn_{0.65}Ni_{0.58}Mn_{1.75}O_4$	265 at 0.1 A g^{-1}	100% (5000) at 2 A g^{-1}	176
$ZMO_{0.94}H_2O$	230 at 0.5 A g^{-1}	75% (2000) at 4 A g^{-1}	107
OD-ZMO@PEDOT	221 at 0.08 A g^{-1}	93.8% (300) at 1.29 A g^{-1}	34
N-ZMO NTAs	223 at 0.1 A g^{-1}	92.1% (1500) at 2 A g^{-1}	162
ZMO/CNT	220 at 0.1 A g^{-1}	97% (2000) at 3 A g^{-1}	143
S-ZMO/CNTs	175 at 0.5 A g^{-1}	94.1% (800) at 1.5 A g^{-1}	33
ZMO–CNT/C	209 at 0.5 A g^{-1}	48% (1000) at 1 A g^{-1}	169
N-ZMO	225 at 0.3 A g^{-1}	~40% (1000) at 3 A g^{-1}	97
Zn/Mn-d-ZMO@C	194 at 0.1 A g^{-1}	84% (2000) at 3 A g^{-1}	164
Mn_2O_3 + ZMO	247 at 0.1 A g^{-1}	93.3% (2000) at 3 A g^{-1}	61
$ZN_{0.5}MO$/NCNT	239 at 0.1 A g^{-1}	78.5% (100) at 0.2 A g^{-1}	177
ZMO/CuO	150 at 0.3 A g^{-1}	~52% (1000) at 0.2 A g^{-1}	180
ZMO@$Ti_3C_2T_x$	126 at 0.1 A g^{-1}	92.4 (5000) at 1 A g^{-1}	75
ZMO@PCP	176 at 0.1 A g^{-1}	90.3 (2000) at 1 A g^{-1}	184
ZMO-MnOOH/C	336 at 0.1 A g^{-1}	79.1% (1000) at 1 A g^{-1}	185
ZMO/Mn_2O_3	216 at 0.2 A g^{-1}	97.8% (2000) at 2 A g^{-1}	186
ZMO/Mn_2O_3	82 at 0.5 A g^{-1}	~135% (300) at 0.5 A g^{-1}	187
Ni-doped ZMO/Mn_2O_3	235 at 0.2 A g^{-1}	91.3% (3000) at 2 A g^{-1}	179

Coating with PEDOT further enhanced Zn^{2+} intercalation, resulting in a total capacity of 221 mA h g^{-1}. Shi *et al.*[75] reported detailed *in situ* and *ex situ* experiments on 3D assembly of ZMO@Ti-MXene ($Ti_3C_2T_x$) with a gelatin-based electrolyte. The conductive MXene improved structural stability by inhibiting ZMO aggregation and dissolution. This cathode achieved a high specific capacity (172 mA h g^{-1}) and excellent cycling stability (~92.4% after 5000 cycles). Post-mortem analysis revealed that capacity fading was primarily due to the formation of the irreversible ZnO byproduct.

Qiu *et al.* developed flexible quasi-solid-state ZIBs utilizing modulated N-doped coupled oxygen vacancies as the cathode, enhancing conductivity, ion transport, active sites, and surface capacitive contribution. The quasi-solid-state device exhibited similar electrochemical behavior to aqueous systems, indicating good Zn^{2+} insertion/extraction kinetics. The PVA/LiCl–$ZnCl_2$–$MnSO_4$ gel electrolyte played a critical role, with LiCl enhancing conductivity, $MnSO_4$ mitigating ZMO dissolution, and $ZnCl_2$ improving discharge voltage, resulting in improved energy and power densities. Moreover, the one-dimensional (1D) hollow NTA nanoarchitecture facilitated rapid zinc ion diffusion, yielding a high specific capacity (223 mA h g^{-1} at 0.1 A g^{-1}) and favorable rate capability (133 mA h g^{-1} at 4 A g^{-1}). Additionally, the 1D hollow structure alleviates mechanical stress from zinc ion cycling, leading to exceptional long-term durability (92.1% retention after 1500 cycles). Significantly, the quasi-solid-state N-ZMO NTAs//Zn device was successfully fabricated, achieving an impressive energy density of 214.6 W h kg^{-1} and a peak power density of 4 kW kg^{-1}.[162] Huang *et al.*[97] synthesized N-doped mesoporous ZMO nanocages with abundant oxygen vacancies to overcome the inherent sluggish rate capacitance. N-doped ZMO exhibits excellent ability to store Zn^{2+} with high specific capacity (225 mA h g^{-1} at 0.3 A g^{-1}), good rate performance, and cycling stability (85.7% after 1000 cycles at 3 A g^{-1}). A flexible quasi-solid-state device was constructed with a high energy density of 261.6 W h kg^{-1}, demonstrating long-lasting durability.

Table 9 presents a comprehensive overview of various ZMO-based cathode materials for ZIBs, highlighting their specific capacities, capacity retention, and corresponding references. The table showcases the diverse approaches employed to enhance the performance of ZMO in ZIBs, including the incorporation of conductive materials, doping, and the creation of cationic vacancies.

Table 10 compares the impact of aqueous and organic electrolytes on ZMO performance in ZIBs. Aqueous electrolytes offer

Table 10 Impact of electrolyte on ZMO performance in ZIBs

Electrolyte type	Advantages	Disadvantages
Aqueous	- High ionic conductivity - Cost-effective	- Mn dissolution - Dendrite formation - Limited electrochemical window
Organic	- Wider electrochemical window - Improved stability - Reduced dendrite formation	- Lower ionic conductivity - Higher cost - Sluggish Zn^{2+} migration kinetics

Table 11 Strategies to overcome challenges in ZMO battery applications

Challenge	Battery type	Modification strategy	Key benefits
Low electrical conductivity	LIBs, SIBs, and ZIBs	- Composite with conductive materials (CNTs, graphene, MXenes, *etc.*)	- Enhanced charge transfer
		- Doping (Ni, S, N, *etc.*)	- Improved rate capability
		- Introduce oxygen vacancies	- Increased capacity
Volume changes during cycling	LIBs and ZIBs	- Nanostructured ZMO	- Accommodate volume expansion/contraction
		- Porous/hollow architectures	- Maintain structural integrity
		- Core–shell structures	- Improve cycling stability
Mn dissolution	ZIBs	- Mn^{2+} additives in electrolyte	- Suppress Mn dissolution
		- Mn–O–C bond formation	- Improve cycling stability
		- Cation-deficient ZMO	
		- pH modification	
Zn^{2+} diffusion limitations	ZIBs	- Cation-deficient ZMO	- Enhanced Zn^{2+} diffusion kinetics
		- Lattice expansion through doping	- Improved rate capability and capacity
		- Lattice expansion through S doping	
		- Structural water incorporation	
		- Al^{3+} doping to increase interlayer spacing	
Electrolyte limitations	LIBs and ZIBs	- "Water-in-salt" electrolytes	- Enhance ion desolvation
		- Optimize Li-based electrolytes (LiTFSI in EC-DMC)	- Improve ionic conductivity
		- Explore Zn-based bulky-anion electrolytes ($Zn(CF_3SO_3)_2$)	- Widen the electrochemical stability window
		- Hybrid electrolytes (aqueous/organic)	- Suppress dendrite formation and corrosion
		- Gel and quasi-solid-state electrolytes	- Enhance safety and flexibility
		- Additives to suppress Zn dendrite growth	- Improve Zn^{2+} migration kinetics

high ionic conductivity but can lead to Mn dissolution and dendrite formation. Organic electrolytes provide wider electrochemical windows and improved stability but have lower ionic conductivity. Despite these promising results, gel electrolytes still face stability challenges and often exhibit low ionic conductivity. Further research is needed to improve their performance and enable the development of efficient, flexible ZIBs for wearable technologies.

Although ZMO is a promising cathode material for ZIBs due to its cost-effectiveness and high theoretical capacity, several challenges hinder its practical application. Table 11 outlines the major challenges encountered in utilizing ZMO as a battery material and the corresponding modification strategies employed to address these limitations.

To sum up the battery section, ZMO has shown promise as an electrode material in various battery systems, including LIBs,

Table 12 ZMO in different battery systems: advantages, disadvantages, and mitigation strategies

Battery type	Advantages	Drawbacks	Mitigation strategies
LIBs	- High theoretical capacity	- Low electrical conductivity	- Composite with conductive materials (CNTs and graphene)
	- Low working voltage	- Volume changes during cycling	- Design unique nanostructures (such as hollow spheres and core–shell)
	- Abundant		- Optimize electrolyte formulations
SIBs	- Environmentally friendly	- Larger ionic radius of Na^+ compared to Li^+	- Develop suitable anode materials
		- Fewer studies and less mature technology compared to LIBs	- Composite with conductive materials
			- Design 3D hierarchical architectures
ZIBs		- Irreversible structural transformation and Mn^{3+} disproportionation reaction	- Create cation-deficient structures
		- Low electrical conductivity	- Introduce elemental doping
			- Composite with conductive materials (CNTs and MXenes)
			- Explore organic/water cosolvent electrolytes

Table 13 Summary of ZMO applications in various battery systems

Battery type	ZMO role	Modification strategy	Key benefits observed
LIBs and SIBs	Anode	- Nanostructured ZMO - Porous/hollow architectures - ZMO/carbon composites - Defect engineering and doping - Electrolyte optimization - ZMO/nitrogen-doped graphene composites - ZMO microtubules	- High capacity (exceeding the theoretical value in some cases) - Improved cycling stability and rate capability - Enhanced conductivity and Li^+ diffusion - Mitigated volume changes - High capacity and cycling stability - Good rate capability
ZIBs	Cathode	- Conductive additives (CNTs and graphene) - Mn dissolution suppression strategies - Electrolyte optimization - Cation-deficient ZMO - ZMO-based composites and nanostructures - Organic/hybrid and quasi-solid-state electrolytes	- Improved capacity and cycling stability - Enhanced Zn^{2+} diffusion and conductivity - Mitigated Zn dendrite growth and corrosion - Wider electrochemical stability window

Table 14 Summary of ZMO performance in energy storage applications

Application	Key findings	Challenges
Supercapacitors	- ZMO/carbon composites show promise - Synergy between ZMO and the composite material is crucial - High specific capacitance achieved with cost-effective porous ZMO	- Achieving synergy in ZMO/carbon composites - Balancing conductivity and active sites
LIBs	- ZMO/carbon composites show promise as anode materials - High specific capacity and long-term cyclability achieved	- Low electrical conductivity - Volume changes during cycling
SIBs	- ZMO with microtubular morphology shows potential - Carbon-based materials help mitigate stress during cycling	- Poor cyclability
ZIBs	- ZMO shows potential as a cathode material - Further exploration needed to achieve higher specific capacities	- Low specific capacity

SIBs, and ZIBs. Its properties, such as high theoretical capacity, low cost, and environmental friendliness, make it an attractive option for next-generation energy storage. However, ZMO also presents challenges such as low electrical conductivity and volume changes during cycling, which can affect its performance and long-term stability. To address these issues, researchers have explored various strategies, including compositing ZMO with conductive materials such as CNTs and graphene, and designing unique nanostructures to accommodate volume changes and enhance ion diffusion. Table 12 summarizes the advantages and disadvantages of using ZMO in different battery types. As the table illustrates, ZMO offers distinct advantages and faces specific challenges depending on the battery type. In LIBs, the focus is on enhancing conductivity and mitigating volume changes, while in SIBs, the research aims to address the limitations associated with sodium-ion size and advance the technology's maturity. For ZIBs, the emphasis is on improving structural stability, preventing manganese dissolution, and enhancing Zn^{2+} diffusion kinetics. By understanding these nuances, researchers can tailor their strategies to optimize ZMO's performance in each battery system, paving the way for its successful integration into next-generation energy storage devices.

7 Conclusion and perspectives

This review has explored the extensive research on ZMO, focusing on its use in energy storage devices. ZMO/carbon composites have garnered significant attention, showing promise for supercapacitor applications despite complex synthesis and high costs. A notable breakthrough is the cost-effective porous ZMO with high specific capacitance. However, achieving synergy in ZMO/carbon composites for supercapacitors remains a challenge, as carbon can reduce active sites while improving cycling stability.

Beyond supercapacitors, ZMO demonstrates versatility in various battery types. ZMO/carbon composites show promise as anode materials in LIBs and SIBs, exhibiting high specific capacity and long-term cyclability. ZMO also shows potential in ZIBs, though further exploration is needed to achieve higher specific capacities. This versatility makes ZMO a compelling solution for energy storage, contributing to the development of sustainable and cost-effective energy solutions. Table 13 provides a concise overview of ZMO's applications in different battery types, highlighting the key modification strategies employed and the resulting benefits.

7.1 Key findings and challenges

In supercapacitors, ZMO exhibits pseudocapacitive behavior, offering high energy density and power density. The electrochemical performance is strongly influenced by factors such as morphology, surface area, and the incorporation of conductive additives or dopants. HT and ST synthesis methods have been widely employed to control these parameters, leading to the fabrication of ZMO with diverse morphologies, including nanowires, nanosheets, and hollow microspheres. While

significant progress has been made, challenges remain in achieving high cycling stability and rate capability, particularly at high current densities. Future research should focus on developing strategies to enhance the electrical conductivity and structural integrity of ZMO-based electrodes, such as optimizing synthesis conditions, surface modifications, and the formation of robust composites with conductive materials such as graphene and carbon nanotubes.

In batteries, ZMO has been investigated as an electrode material for LIBs, SIBs, and ZIBs. Its high theoretical capacity, low cost, and environmental friendliness make it an attractive alternative to conventional electrode materials. However, challenges such as low electrical conductivity and volume changes during cycling need to be addressed to realize its full potential. Table 14 summarizes the key findings and challenges for ZMO in various energy storage applications, highlighting the need for further research to fully realize its potential.

7.2 Outlooks and future directions

To further advance ZMO research and its practical applications in energy storage, several key areas warrant attention:

• Emerging energy storage technologies such as hybrid supercapacitors and metal–air batteries, warrant further investigation. In hybrid supercapacitors, ZMO can be combined with high-surface-area carbon materials to enhance energy and power density, necessitating research focused on optimizing electrode design and electrolyte to balance these characteristics. For metal–air batteries, ZMO holds promise as a bifunctional catalyst for oxygen reduction and evolution reactions, requiring efforts to enhance its catalytic activity and stability.

• Advanced characterization: employing advanced characterization techniques, such as *in situ* X-ray diffraction (XRD), X-ray absorption spectroscopy (XAS), and electron microscopy, can provide deeper insights into the structural evolution of ZMO during electrochemical processes. This understanding is crucial for optimizing material design and synthesis strategies to enhance performance and stability.

• Electrolyte optimization: the development of electrolytes tailored to specific battery systems is essential. For LIBs and SIBs, research should focus on electrolytes that form stable SEIs to minimize capacity fading and enhance cycling stability. In ZIBs, the focus should be on electrolytes that suppress Mn dissolution and dendrite formation, which are major contributors to performance degradation. Exploring novel electrolyte additives and organic/water cosolvent systems can lead to significant improvements in battery performance and longevity.

• Solid-state batteries (SSBs): investigating the application of ZMO in SSBs is a promising direction. SSBs offer advantages in terms of safety and stability compared to liquid electrolytes. However, challenges such as interfacial resistance and ion transport need to be addressed. Research efforts should focus on developing compatible solid-state electrolytes and optimizing electrode/electrolyte interfaces to enable efficient ion transport and enhance the performance of ZMO-based SSBs.

• Anode-free application: anode-free batteries are a promising technology for next-generation energy storage due to their potential for higher energy density and reduced reliance on critical materials like lithium.[188–190] For ZMO cathodes in ZIBs, anode-free configurations present unique opportunities and challenges. Research should focus on mitigating issues such as zinc dendrite formation and uneven deposition, which can lead to battery failure. Strategies may include electrolyte optimization, surface modification of the current collector, and advanced characterization techniques to understand the mechanisms of zinc deposition in anode-free systems. This could unlock ZMO's full potential in applications ranging from portable electronics to grid-scale energy storage.

• Flexible and wearable devices: the development of flexible and wearable energy storage devices is a rapidly growing area. ZMO, with its potential for fabrication into thin films and nanostructures, can be integrated into flexible substrates for applications in wearable electronics, sensors, and implantable medical devices. Research should focus on developing scalable fabrication methods for ZMO-based flexible electrodes and optimizing device design for flexibility, durability, and high energy density.

• Theoretical modeling and simulation: utilizing DFT calculations and other computational methods can provide valuable insights into the electronic structure, charge transfer mechanisms, and ion diffusion pathways in ZMO. This theoretical understanding can guide material design and optimization, leading to the development of ZMO with enhanced electrochemical properties.

• Machine learning and artificial intelligence: the application of machine learning (ML) and artificial intelligence (AI) can accelerate the discovery and optimization of ZMO-based materials for energy storage. AI algorithms can analyze large datasets from experiments and simulations to identify patterns and predict the performance of new materials, guiding the design of high-performance electrodes and devices.

• Sustainability and life cycle assessment: as the demand for energy storage technologies grows, it is essential to consider the sustainability and environmental impact of material production and disposal. Research should focus on developing environmentally friendly synthesis methods for ZMO, utilizing abundant and non-toxic precursors, and minimizing waste generation. Life cycle assessments can help evaluate the environmental impact of ZMO-based energy storage devices, guiding the development of sustainable and responsible manufacturing practices.

By pursuing these research directions, we can unlock the full potential of ZMO, contributing to the development of high-performance, sustainable, and cost-effective energy storage solutions for a wide range of applications. The future of ZMO in the energy storage landscape is promising, and continued research efforts will undoubtedly lead to further breakthroughs and innovations in this field.

Data availability

No primary research results, software or code have been included and no new data were generated or analysed as part of this review.

Author contributions

Joel Kingston Ramesh and Sasan Rostami: investigation, visualization, writing – original draft, writing – review & editing. Rajesh Jayaprakasan and R. Margrate Bhackiyavathi Princess: investigation, writing – original draft. Radhika Govindaraju: investigation, writing – original draft, writing – review & editing. Jinho Kim: funding acquisition, project administration, writing – review & editing. Rainer Adelung: funding acquisition, project administration, writing – review & editing. Palanisamy Rajkumar: investigation, visualization, writing – original draft, writing – review & editing. Mozaffar Abdollahifar: conceptualization, investigation, visualization, writing – original draft, writing – review & editing, project administration, supervision.

Conflicts of interest

The authors declare that they have no known competing financial interests or personal relationships that could have appeared to influence the work reported in this paper.

Acknowledgements

Funding for this work was provided by the German Federal Ministry for Education and Research (BMBF) for the funding of the research project of SiLiNE (Reference No. 03XP0419B) and by the Deutsche Forschungsgemeinschaft (DFG, Project No. 546658628). Also, this research was supported by the "Korea Medical Device Development Fund (KMDF) grant funded by the Korea government (KMDF_PR_20200901_0154)".

References

1 M. Chen, Y. Zhang, G. Xing, S.-L. Chou and Y. Tang, *Energy Environ. Sci.*, 2021, **14**, 3323–3351.
2 L. Zu, W. Zhang, L. Qu, L. Liu, W. Li, A. Yu and D. Zhao, *Adv. Energy Mater.*, 2020, **10**, 2002152.
3 K. Zou, W. Deng, D. S. Silvester, G. Zou, H. Hou, C. E. Banks, L. Li, J. Hu and X. Ji, *ACS Nano*, 2024, **18**, 19950–20000.
4 M. Girirajan, A. K. Bojarajan, I. N. Pulidindi, K. N. Hui and S. Sangaraju, *Coord. Chem. Rev.*, 2024, **518**, 216080.
5 K. Zuo, S. Garcia-Segura, G. A. Cerrón-Calle, F.-Y. Chen, X. Tian, X. Wang, X. Huang, H. Wang, P. J. J. Alvarez, J. Lou, M. Elimelech and Q. Li, *Nat. Rev. Mater.*, 2023, **8**, 472–490.
6 C. Liu, F. Li, L. P. Ma and H. M. Cheng, *Adv. Mater.*, 2010, **22**, E28–E62.
7 M. K. Khan, M. Raza, M. Shahbaz, U. Farooq and M. U. Akram, *J. Energy Storage*, 2024, **92**, 112112.
8 J. B. Goodenough, *Chem. Mater.*, 2014, **26**, 820–829.
9 S. Yuan, X. Duan, J. Liu, Y. Ye, F. Lv, T. Liu, Q. Wang and X. Zhang, *Energy Storage Mater.*, 2021, **42**, 317–369.
10 H. Cavers, P. Molaiyan, M. Abdollahifar, U. Lassi and A. Kwade, *Adv. Energy Mater.*, 2022, **12**, 2200147.
11 A. Z. Al Shaqsi, K. Sopian and A. Al-Hinai, *Energy Rep.*, 2020, **6**, 288–306.
12 J. Baneshi, M. Haghighi, N. Jodeiri, M. Abdollahifar and H. Ajamein, *Energy Convers. Manage.*, 2014, **87**, 928–937.
13 M. Abdollahifar, M. Haghighi and A. A. Babaluo, *J. Ind. Eng. Chem.*, 2014, **20**, 1845–1851.
14 M. Abdollahifar, M. Haghighi, A. A. Babaluo and S. K. Talkhoncheh, *Ultrason. Sonochem.*, 2016, **31**, 173–183.
15 S. K. Talkhoncheh, M. Haghighi, S. Minaei, H. Ajamein and M. Abdollahifar, *RSC Adv.*, 2016, **6**, 57199–57209.
16 N. Nitta, F. Wu, J. T. Lee and G. Yushin, *Mater. Today*, 2015, **18**, 252–264.
17 S.-M. Chen, R. Ramachandran, V. Mani and R. Saraswathi, *Int. J. Electrochem. Sci.*, 2014, **9**, 4072–4085.
18 M. Abdollahifar, H.-W. Liu, C.-H. Lin, Y.-T. Weng, H.-S. Sheu, J.-F. Lee, M.-L. Lu, Y.-F. Liao and N.-L. Wu, *Energy Environ. Mater.*, 2020, **3**, 405–413.
19 M. Chiku, M. Abdollahifar, T. Brousse, G. Z. Chen, O. Crosnier, B. Dunn, K. Fic, C.-C. Hu, P. JeŻOwski, A. MaĆKowiak, K. Naoi, N. Ogihara, N. Okita, M. Okubo, W. Sugimoto and N.-L. Wu, *Electrochemistry*, 2024, **92**, 074002.
20 M. Abdollahifar, P. Lannelongue, H.-W. Liu, H. Chen, C.-H. Liao, H.-S. Sheu, J.-F. Lee, Y.-F. Liao and N.-L. Wu, *ACS Sustain. Chem. Eng.*, 2021, **9**, 13717–13725.
21 R. Sagar and A. S. Gandhi, *Appl. Phys. A*, 2021, **127**, 84.
22 J. Zia, E. S. Aazam and U. Riaz, *J. Mater. Res. Technol.*, 2020, **9**, 9709–9719.
23 L. Jiang, J. Hu, S. Yan, Y. Xue, S. Tang, L. Zhang and Y. Lv, *Microchem. J.*, 2022, **172**, 106990.
24 S. Agrohiya, S. Dahiya, I. Rawal, P. K. Goyal, A. Ohlan, R. Punia and A. S. Maan, *J. Mater. Sci.: Mater. Electron.*, 2023, **34**, 514.
25 P. Gaikwad, N. Tiwari, R. Kamat, S. M. Mane and S. B. Kulkarni, *J. Mater. Sci. Eng. B*, 2024, **307**, 117544.
26 L. Becker, 2024, **http://www.leonland.de/elements_by_price/en/list**.
27 M. Robbins and P. K. Baltzer, *J. Appl. Phys.*, 1965, **36**, 1039–1040.
28 X.-D. Zhang, Z.-S. Wu, J. Zang, D. Li and Z.-D. Zhang, *J. Phys. Chem. Solids*, 2007, **68**, 1583–1590.
29 Y. Bessekhouad, D. Robert and J. V. Weber, *Catal. Today*, 2005, **101**, 315–321.
30 H. J. Kim, I. C. Song, J. H. Sim, H. Kim, D. Kim, Y. E. Ihm and W. K. Choo, *J. Appl. Phys.*, 2004, **95**, 7387–7389.
31 Y. Yang, Y. Zhao, L. Xiao and L. Zhang, *Electrochem. Commun.*, 2008, **10**, 1117–1120.
32 L. Luo, H. Qiao, K. Chen, Y. Fei and Q. Wei, *Electrochim. Acta*, 2015, **177**, 283–289.
33 Y. Yang, T. Shao, Y. Zhang, Y. Lu, M. Li, H. Liu, Q. Xu and Y. Xia, *J. Power Sources*, 2023, **564**, 232863.
34 H. Zhang, J. Wang, Q. Liu, W. He, Z. Lai, X. Zhang, M. Yu, Y. Tong and X. Lu, *Energy Storage Mater.*, 2019, **21**, 154–161.
35 G. S. Kumar, D. S. Baji, S. Nair and D. Santhanagopalan, *Energy Fuels*, 2023, **37**, 12436–12444.
36 K. Sasidharachari, K. Y. Cho and S. Yoon, *ACS Appl. Energy Mater.*, 2020, **3**, 3293–3301.
37 J. G. Kim, S. H. Lee, Y. Kim and W. B. Kim, *ACS Appl. Mater. Interfaces*, 2013, **5**, 11321–11328.

38 M. Abdollahifar, S.-S. Huang, Y.-H. Lin, H.-S. Sheu, J.-F. Lee, M.-L. Lu, Y.-F. Liao and N.-L. Wu, *J. Power Sources*, 2019, **412**, 545–551.
39 J. Xu, H. Zhang, R. Wang, P. Xu, Y. Tong, Q. Lu and F. Gao, *Langmuir*, 2018, **34**, 1242–1248.
40 L. I. Granone, R. Dillert, P. Heitjans and D. W. Bahnemann, *ChemistrySelect*, 2019, **4**, 1232–1239.
41 K. E. Sickafus, J. M. Wills and N. W. Grimes, *J. Am. Ceram. Soc.*, 1999, **82**, 3279–3292.
42 K. Cai, S.-h. Luo, J. Feng, J. Wang, Y. Zhan, Q. Wang, Y. Zhang and X. Liu, *Chem. Rec.*, 2022, **22**, e202100169.
43 W. Du, J. Liu, A. Zeb and X. Lin, *ACS Appl. Mater. Interfaces*, 2022, **14**, 37652–37666.
44 Y. Tang, Z. Zhang, Y. Jin, S. Gao, D. Huang, S. Xu and R. Zou, *Chem. Mater.*, 2022, **34**, 10338–10346.
45 T. Garibaldi Brian, M. Reimers, N. Ernst, G. Bova, E. Nowakowski, J. Bukowski, C. Ellis Brandon, C. Smith, L. Sauer, K. Dionne, C. Carroll Karen, L. Maragakis Lisa and M. Parrish Nicole, *J. Clin. Microbiol.*, 2017, **55**, 545–551.
46 N. Mariotti, M. Bonomo, L. Fagiolari, N. Barbero, C. Gerbaldi, F. Bella and C. Barolo, *Green Chem.*, 2020, **22**, 7168–7218.
47 A. R. Upadhya, G. N. Dayananda, G. M. Kamalakannan, J. Ramaswamy Setty and J. Christopher Daniel, *Int. J. Aero. Eng.*, 2011, **2011**, 985871.
48 S. H. Feng and G. H. Li, *Modern Inorganic Synthetic Chemistry*, 2nd edn, 2017, pp. 73–104.
49 A. T. Adeleye, K. I. John, P. G. Adeleye, A. A. Akande and O. O. Banjoko, *J. Mater. Sci.*, 2021, **56**, 18391–18416.
50 F. Salimi, M. Abdollahifar, P. Jafari and M. Hidaryan, *J. Serb. Chem. Soc.*, 2017, **82**, 203–213.
51 M. Abdollahifar, R. M. Zamani, E. Beiygie and H. Nekouei, *J. Serb. Chem. Soc.*, 2014, **79**, 1007–1017.
52 M. Abdollahifar, *J. Chem. Res.*, 2014, **38**, 154–158.
53 Y. Zhang, Y. Zhang, C. Guo, B. Tang, X. Wang and Z. Bai, *Electrochim. Acta*, 2015, **182**, 1140–1144.
54 C. Park, E. Samuel, B.-Y. Kim, S. An, H.-S. Lee and S. S. Yoon, *J. Mater. Sci. Technol.*, 2023, **137**, 193–204.
55 N. Ren, H. Jiu, L. Jiang, Q. Zhang, S. Yu, Y. Gao, Z. Gao and L. Zhang, *J. Alloys Compd.*, 2018, **740**, 28–35.
56 X. Zhu, Z. Wei, W. Zhao, X. Zhang, L. Zhang and X. Wang, *J. Electron. Mater.*, 2018, **47**, 6428–6436.
57 Q. B. Le, E. Vargun, H. Fei, Q. Cheng, C. Bubulinca, R. Moučka, I. Sapurina, T. D. Tran, N. E. Kazantseva and P. Saha, *J. Electron. Mater.*, 2020, **49**, 4697–4706.
58 Y. Guan, Y. Feng, Y. Mu, L. Fang, H. Zhang and Y. Wang, *Nanotechnology*, 2016, **27**, 475402.
59 J. Chen, W. Liu, S. Liu, H. Wang, Y. Zhang and S. Chen, *Chem. Eng. J.*, 2017, **308**, 1200–1208.
60 Y. Lin, L. Zhang and H. Liu, *Int. J. Hydrogen Energy*, 2020, **45**, 6874–6884.
61 Y. Zeng, Y. Wang, Q. Jin, Z. Pei, D. Luan, X. Zhang and X. W. Lou, *Angew. Chem., Int. Ed.*, 2021, **60**, 25793–25798.
62 K. Cai, S.-h. Luo, J. Cong, K. Li, S.-x. Yan, P.-q. Hou, Y. Song, Q. Wang, Y. Zhang, X. Liu, X. Lei, W. Mu and J. Gao, *J. Alloys Compd.*, 2022, **909**, 164882.
63 P. Rosaiah, N. Maaouni, M. Goddati, J. Lee, S. Sambasivam, M. R. Karim, I. A. Alnaser, V. R. M. Reddy and W. K. Kim, *J. Energy Storage*, 2024, **76**, 109636.
64 H. Jiu, Q. Zhang, L. Zhang, Q. Xu and C. Wang, *Microporous Mesoporous Mater.*, 2022, **339**, 111998.
65 N. Wang, X. Ma, H. Xu, L. Chen, J. Yue, F. Niu, J. Yang and Y. Qian, *Nano Energy*, 2014, **6**, 193–199.
66 C. Yuan, J. Li, L. Hou, L. Zhang and X. Zhang, *Part. Part. Syst. Charact.*, 2014, **31**, 657–663.
67 G. Zhang, L. Yu, H. B. Wu, H. E. Hoster and X. W. Lou, *Adv. Mater.*, 2012, **24**, 4609–4613.
68 H. Rong, G. Xie, S. Cheng, Z. Zhen, Z. Jiang, J. Huang, Y. Jiang, B. Chen and Z.-J. Jiang, *J. Alloys Compd.*, 2016, **679**, 231–238.
69 M. P. Mani, V. Venkatachalam, K. Thamizharasan and M. Jothibas, *J. Electron. Mater.*, 2021, **50**, 4381–4387.
70 J. Zou, B. Liu, H. Liu, Y. Ding, T. Xin and Y. Wang, *Mater. Res. Bull.*, 2018, **107**, 468–476.
71 S. Deepika, N. Sivakumar, T. Jothilakshmi, R. Viji and R. Ramesh, *Ionics*, 2024, **31**, 945–952.
72 N. Guo, X. Q. Wei, X. L. Deng and X. J. Xu, *Appl. Surf. Sci.*, 2015, **356**, 1127–1134.
73 L. Lyu, C. W. Kim, K.-d. Seong, J. Kang, S. Liu, Y. Yamauchi and Y. Piao, *Chem. Eng. J.*, 2022, **430**, 133115.
74 A. E. Reddy, T. Anitha, C. V. V. Muralee Gopi, I. K. Durga and H.-J. Kim, *New J. Chem.*, 2018, **42**, 2964–2969.
75 M. Shi, B. Wang, Y. Shen, J. Jiang, W. Zhu, Y. Su, M. Narayanasamy, S. Angaiah, C. Yan and Q. Peng, *Chem. Eng. J.*, 2020, **399**, 125627.
76 V. Sannasi and K. Subbian, *Ceram. Int.*, 2021, **47**, 12300–12309.
77 M. Islam, G. Ali, M. Akbar, B. Ali, M.-G. Jeong, J.-Y. Kim, K. Y. Chung, K.-W. Nam and H.-G. Jung, *Int. J. Energy Res.*, 2022, **46**, 6444–6456.
78 Y. Zhang, P. Zhang, Y. Xu, X. Song, H. Wang and T. Ma, *J. Materiomics*, 2021, **7**, 699–707.
79 S. Khaja Hussain and J. Su Yu, *Chem. Eng. J.*, 2019, **361**, 1030–1042.
80 V. Soundharrajan, B. Sambandam, S. Kim, S. Islam, J. Jo, S. Kim, V. Mathew, Y.-k. Sun and J. Kim, *Energy Storage Mater.*, 2020, **28**, 407–417.
81 T. Zhang, H. Liang, C. Xie, H. Qiu, Z. Fang, L. Wang, H. Yue, G. Chen, Y. Wei, C. Wang and D. Zhang, *Chem. Eng. J.*, 2017, **326**, 820–830.
82 T. Zhang, H. Yue, H. Qiu, Y. Wei, C. Wang, G. Chen and D. Zhang, *Nanotechnology*, 2017, **28**, 105403.
83 C. Chen, Y. Huang, Q. Fang and G. Qian, *J. Alloys Compd.*, 2021, **877**, 160218.
84 C. Chen, Y. Huang, Q. Fang and S. Wang, *J. Alloys Compd.*, 2021, **889**, 161654.
85 P. Zhou, L. Zhong, Z. Liu, M. Liu, T. Zhou, Y. Zhao, X. Lai, J. Bi and D. Gao, *Appl. Surf. Sci.*, 2022, **578**, 152087.
86 F.-t. Li, J. Ran, M. Jaroniec and S. Z. Qiao, *Nanoscale*, 2015, **7**, 17590–17610.
87 T. Huang, C. Zhao, Z. Qiu, J. Luo and Z. Hu, *Ionics*, 2017, **23**, 139–146.

88 P. Kommu, G. P. Singh, C. S. Chakra, S. Jana, V. Kumar and A. S. Bhattacharyya, *J. Mater. Sci. Eng. B*, 2020, **261**, 114647.
89 C.-K. Sim, S. R. Majid and N. Z. Mahmood, *J. Alloys Compd.*, 2019, **803**, 424–433.
90 C.-K. Sim, S. A. Razali, S. R. Majid and N. Z. Mahmood, *J. Electron. Mater.*, 2020, **49**, 1024–1035.
91 M. Hasan, S. Zawar, G. M. Mustafa, A. Ghaffar, A. Razaq and S. Atiq, *Phys. B*, 2022, **633**, 413767.
92 M. Abdollahifar, S.-S. Huang, Y.-H. Lin, Y.-C. Lin, B.-Y. Shih, H.-S. Sheu, Y.-F. Liao and N.-L. Wu, *J. Power Sources*, 2018, **378**, 90–97.
93 B. Joshi, E. Samuel, Y. Kim, T. Kim, M. El-Newehy, A. Aldalbahi and S. S. Yoon, *Int. J. Energy Res.*, 2022, **46**, 22100–22112.
94 A. V. Radhamani, M. Krishna Surendra and M. S. Ramachandra Rao, *Mater. Des.*, 2018, **139**, 162–171.
95 X. Luo, X. Zhang, L. Chen, L. Li, G. Zhu, G. Chen, D. Yan, H. Xu and A. Yu, *ACS Appl. Mater. Interfaces*, 2018, **10**, 33170–33178.
96 A. O. M. Alzahrani, H. Hassan, M. W. Iqbal, A. O. Alosaimi, S. Alghamdi, A. A. Melaibari, S. A. Al-Ghamdi, T. S. Almoneef, R. M. Alzahrani and Y. Al-Hadeethi, *Int. J. Hydrogen Energy*, 2024, **66**, 415–429.
97 C. Huang, Q. Wang, D. Zhang and G. Shen, *Nano Res.*, 2022, **15**, 8118–8127.
98 L. Yin, Z. Zhang, Z. Li, F. Hao, Q. Li, C. Wang, R. Fan and Y. Qi, *Adv. Funct. Mater.*, 2014, **24**, 4176–4185.
99 F. Pang, S. Hou, P. Wang, M. Liu, Y. Luo and L. Zhao, *Chem.–Eur. J.*, 2019, **25**, 5043–5050.
100 H. Jiu, N. Ren, L. Zhang, Q. Zhang, Y. Gao and Y. Meng, *J. Phys. Chem. Solids*, 2019, **135**, 109090.
101 S. Aouini, A. Bardaoui, A. M. Ferraria, D. M. F. Santos and R. Chtourou, *Energies*, 2022, **15**, 9352.
102 P. Li, J. Liu, Y. Liu, Y. Wang, Z. Li, W. Wu, Y. Wang, L. Yin, H. Xie, M. Wu, X. He and J. Qiu, *Electrochim. Acta*, 2015, **180**, 164–172.
103 K. Yu, M. Chang, L. Yue, X. Wang, J. Chen and C. Liang, *J. Alloys Compd.*, 2024, **971**, 172769.
104 H. Yun, X. Zhou, H. Zhu and M. Zhang, *J. Colloid Interface Sci.*, 2021, **585**, 138–147.
105 S. Cheng, Q. Ru, Y. Gao, M. Zhen, F. Chen, L. Wei and F. C.-C. Ling, *Chem. Eng. J.*, 2021, **406**, 126133.
106 Y. Tian, Z. Chen, W. Tang, Z. Yang, W. Zhang, S. Li, K. Wang, Y. Sun, Q. Xia and B. Guo, *J. Alloys Compd.*, 2017, **720**, 376–382.
107 T.-H. Wu and W.-Y. Liang, *ACS Appl. Mater. Interfaces*, 2021, **13**, 23822–23832.
108 J. Chen, H. Zuo, C. Q. Wang, Y.-C. Zhang, W. W. Gao, N. Zhao, Y. Huang and S. Xiao, *Electrochim. Acta*, 2022, **426**, 140780.
109 S. Deng, Z. Tie, F. Yue, H. Cao, M. Yao and Z. Niu, *Angew. Chem., Int. Ed.*, 2022, **61**, e202115877.
110 N. Zhang, F. Cheng, Y. Liu, Q. Zhao, K. Lei, C. Chen, X. Liu and J. Chen, *J. Am. Chem. Soc.*, 2016, **138**, 12894–12901.
111 Y. L. Wang, X. Q. Wei, N. Guo, X. L. Deng and X. J. Xu, *J. Mater. Sci.: Mater. Electron.*, 2017, **28**, 1223–1228.
112 A. Bera, L. Halder, S. Kumar Si, A. De, S. Ojha, S. Bera, P. Maity, A. Mondal and B. Bhusan Khatua, *Results Chem.*, 2022, **4**, 100404.
113 N. Senthilkumar, V. Venkatachalam, M. Kandiban, P. Vigneshwaran, R. Jayavel and I. Vetha Potheher, *Phys. E Low-dimens. Syst. Nanostruct.*, 2019, **106**, 121–126.
114 Y. Li, Z. Wei, M. Ding, L. Ma, X. Zhu and J. Liang, *J. Ceram. Soc. Jpn.*, 2019, **127**, 747–753.
115 K. Aruchamy, R. Nagaraj, H. M. Manohara, M. R. Nidhi, D. Mondal, D. Ghosh and S. K. Nataraj, *J. Mater. Sci. Eng. B*, 2020, **252**, 114481.
116 C. L. Pearline, P. Anbalagan, M. Balasingh Moses and J. Joseph Prince, *Mater. Res. Express*, 2019, **6**, 1150c7.
117 Q. Fang, C. Chen, Z. Yang, X. a. Chen, X. Chen and T. Liu, *J. Alloys Compd.*, 2020, **826**, 154084.
118 J. Bhagwan and J. I. Han, *J. Alloys Compd.*, 2024, **976**, 173133.
119 Y. Gao, M. Zheng and H. Pang, *Energy Technol.*, 2015, **3**, 820–824.
120 P. Gao, B. Shen, P. Zhao, G. Shi and X. Zhao, *J. Power Sources*, 2023, **577**, 233231.
121 J. Bhagwan, N. Kumar, K. L. Yadav and Y. Sharma, *Solid State Ionics*, 2018, **321**, 75–82.
122 Z. K. Heiba, M. A. Deyab, A. M. El-naggar and M. B. Mohamed, *Ceram. Int.*, 2021, **47**, 7475–7486.
123 H. Barkhordari, H. Heydari, A. Nosrati and J. B. J. I. Mohammadi, *Ionics*, 2018, **25**, 275–285.
124 B. Ameri, S. S. H. Davarani, H. R. Moazami and H. Darjazi, *J. Alloys Compd.*, 2017, **720**, 408–416.
125 A. Sahoo and Y. Sharma, *Mater. Chem. Phys.*, 2015, **149**, 721–727.
126 D. Boonpakdee, C. F. Guajardo Yévenes, W. Surareungchai and C. La-o-vorakiat, *J. Mater. Chem. A*, 2018, **6**, 7162–7167.
127 V. Augustyn, P. Simon and B. Dunn, *Energy Environ. Sci.*, 2014, **7**, 1597–1614.
128 Y. Jiang and J. Liu, *Energy Environ. Mater.*, 2019, **2**, 30–37.
129 P. Krishnan and V. Biju, *Bull. Mater. Sci.*, 2021, **44**, 288.
130 G. Sivaguru, U. K. Ghorui, M. Girirajan, G. K. Dalapati, P. S. Maram, S. Ghosh, S. Sangaraju and S. Chakrabortty, *ACS Appl. Energy Mater.*, 2024, **7**, 7205–7219.
131 A. Samage, P. Kuppe, M. Halakarni, B. K. Ganesan, S. V. Kamath, H. Yoon and N. S. Kotrappanavar, *J. Energy Storage*, 2024, **97**, 112934.
132 Z. Zhu, Z. Wang, Z. Yan, R. Zhou, Z. Wang and C. Chen, *Ceram. Int.*, 2018, **44**, 20163–20169.
133 Y. Zhao, K. S. Kumar, M. A. Ghanem, N. Roy, J. S. Kim and S. W. Joo, *Ceram. Int.*, 2024, **50**, 49834–49845.
134 Z. Chen, Z. Du, L. Li, K. Jiang, D. Chen and G. Shen, *Energy Environ. Mater.*, 2024, **7**, e12756.
135 M. Abdollahifar, S. Doose, H. Cavers and A. Kwade, *Adv. Mater. Technol.*, 2023, **8**, 2200368.
136 M. Abdollahifar, A. Vinograd, C.-Y. Lu, S.-J. Chang, J. Müller, L. Frankenstein, T. Placke, A. Kwade, M. Winter, C.-Y. Chao and N.-L. Wu, *ACS Appl. Mater. Interfaces*, 2022, **14**, 38824–38834.
137 J. Müller, M. Abdollahifar, A. Vinograd, M. Nöske, C. Nowak, S.-J. Chang, T. Placke, W. Haselrieder,

M. Winter, A. Kwade and N.-L. Wu, *Chem. Eng. J.*, 2021, **407**, 126603.
138 J. Müller, M. Abdollahifar, S. Doose, P. Michalowski, N.-L. Wu and A. Kwade, *J. Power Sources*, 2022, **548**, 232000.
139 S. Bolloju, M. Abdollahifar, S.-K. Parthasarathi, Y.-C. Chen, Y.-T. Weng, C.-Y. Chao and N.-L. Wu, *ACS Sustain. Chem. Eng.*, 2023, **11**, 2623–2633.
140 Y. Zhao, X. Li, B. Yan, D. Xiong, D. Li, S. Lawes and X. Sun, *Adv. Energy Mater.*, 2016, **6**, 1502175.
141 C. Zhao, S. Yao, C. Li, Y. An, S. Zhao, X. Sun, K. Wang, X. Zhang and Y. Ma, *Chem. Eng. J.*, 2024, **497**, 154535.
142 Y. Chen, Y. Xu, Z. Li, W. Zhang, M. Zheng and H. Zhang, *Colloids Surf., A*, 2020, **600**, 124941.
143 F. Gao, B. Mei, X. Xu, J. Ren, D. Zhao, Z. Zhang, Z. Wang, Y. Wu, X. Liu and Y. Zhang, *Chem. Eng. J.*, 2022, **448**, 137742.
144 Z. Tang, S. Zhou, Y. Huang, H. Wang, R. Zhang, Q. Wang, D. Sun, Y. Tang and H. Wang, *Electrochem. Energy Rev.*, 2023, **6**, 8.
145 C. Yuan, L. Zhang, S. Zhu, H. Cao, J. Lin and L. Hou, *Nanotechnology*, 2015, **26**, 145401.
146 P. Xiong, B. Liu, V. Teran, Y. Zhao, L. Peng, X. Wang and G. Yu, *ACS Nano*, 2014, **8**, 8610–8616.
147 T. Zhang, H. Qiu, M. Zhang, Z. Fang, X. Zhao, L. Wang, G. Chen, Y. Wei, H. Yue, C. Wang and D. Zhang, *Carbon*, 2017, **123**, 717–725.
148 Z. Zhao, G. Tian, A. Sarapulova, G. Melinte, J. L. Gómez-Urbano, C. Li, S. Liu, E. Welter, M. Etter and S. Dsoke, *ACS Appl. Mater. Interfaces*, 2019, **11**, 29888–29900.
149 G. Liu, Q. Han and K. Liu, *Ionics*, 2024, **30**, 4509–4518.
150 S. Karimzadeh, B. Safaei, C. Yuan and T.-C. Jen, *Electrochem. Energy Rev.*, 2023, **6**, 24.
151 C. Liang, J. Chen, K. Yu and W. Jin, *J. Alloys Compd.*, 2021, **878**, 160445.
152 K. Cai, S.-h. Luo, J. Cong, K. Li, S.-x. Yan, P.-q. Hou, Q. Wang, Y. Zhang, X. Liu and X. Lei, *J. Electroanal. Chem.*, 2022, **912**, 116237.
153 B. Chandra Sekhar, P. Packiyalakshmi and N. Kalaiselvi, *RSC Adv.*, 2017, **7**, 20057–20061.
154 R. Muruganantham, I. V. B. Maggay, J.-Y. Huang, Y.-G. Lin, C.-C. Yang and W.-R. Liu, *J. Alloys Compd.*, 2020, **844**, 156018.
155 Y. Xu, M. Zhou, X. Wang, C. Wang, L. Liang, F. Grote, M. Wu, Y. Mi and Y. Lei, *Angew. Chem., Int. Ed.*, 2015, **54**, 8768–8771.
156 J. Mei, T. Wang, D. Qi, J. Liu, T. Liao, Y. Yamauchi and Z. Sun, *ACS Nano*, 2021, **15**, 13604–13615.
157 J. Jin, Y. Liu and J. Chen, *Batteries Supercaps*, 2023, **6**, e202300347.
158 Y. Tian, Y. Cai, Y. Chen, M. Jia, H. Hu, W. Xie, D. Li, H. Song, S. Guo and X. Zhang, *Adv. Funct. Mater.*, 2024, **34**, 2316342.
159 O. M. Sousa, L. V. C. Assali, M. V. Lalic, C. M. Araujo, O. Eriksson, H. M. Petrilli and A. B. Klautau, *J. Phys.: Energy*, 2024, **6**, 025025.
160 D. Petersen, M. Gronenberg, G. Lener, E. P. M. Leiva, G. L. Luque, S. Rostami, A. Paolella, B. J. Hwang, R. Adelung and M. Abdollahifar, *Mater. Horiz.*, 2024, **11**, 5914–5945.
161 C. Zhu, G. Fang, S. Liang, Z. Chen, Z. Wang, J. Ma, H. Wang, B. Tang, X. Zheng and J. Zhou, *Energy Storage Mater.*, 2020, **24**, 394–401.
162 W. Qiu, H. Xiao, H. Feng, Z. Lin, H. Gao, W. He and X. Lu, *Chem. Eng. J.*, 2021, **422**, 129890.
163 S. C. Kang, C.-W. Hyeon, S.-Y. Yoo, J. Y. Park, Y. J. Kim, C.-Y. Chung and S.-E. Chun, *J. Alloys Compd.*, 2025, **1010**, 177165.
164 S. Islam, M. H. Alfaruqi, D. Y. Putro, S. Park, S. Kim, S. Lee, M. S. Ahmed, V. Mathew, Y.-K. Sun, J.-Y. Hwang and J. Kim, *Adv. Sci.*, 2021, **8**, 2002636.
165 T. Shao, Y. Zhang, T. Cao, Y. Yang, Z. Li, H. Liu and Y. Wang and YongyaoXia, *Chem. Eng. J.*, 2022, **431**, 133735.
166 R. Gherbi, Y. Bessekhouad and M. Trari, *J. Alloys Compd.*, 2016, **655**, 188–197.
167 S. Aman, N. Ahmad, S. Manzoor, M. M. Alanazi, S. A. M. Abdelmohsen, R. Y. Khosa, A. G. Al-Sehemi, R. Hua, H. A. Alzahrani and A. H. Chughtai, *Catal. Surv. Asia*, 2023, **27**, 165–179.
168 N. H. Hawari, A. Prayogi, Y. Irmawati, P. B. Persada, T. A. Ivandini, A. Zulfia, H. Judawisastra, Q. Yan and A. Sumboja, *J. Energy Storage*, 2024, **100**, 113715.
169 F. Chen, Q. Wang, X. Yang, C. Wang, H. Zang, Y. Tang, T. Li and B. Geng, *Nano Res.*, 2023, **16**, 1726–1732.
170 M. Sharma and R. Sharma, *Mater. Today: Proc.*, 2020, **26**, 3378–3385.
171 Z. Li, C. Wei, C. Niu and R. Zhang, *J. Energy Storage*, 2024, **101**, 113993.
172 R. Durena and A. Zukuls, *Batteries*, 2023, **9**, 311.
173 C. F. Bischoff, O. S. Fitz, J. Burns, M. Bauer, H. Gentischer, K. P. Birke, H.-M. Henning and D. Biro, *J. Electrochem. Soc.*, 2020, **167**, 020545.
174 Y. Liu, Y. X. Liu, R. Lv, M. Han, Y. Chang, Z. Zhao, Y. Sun, T. K. A. Hoang and R. Xing, *ChemPlusChem*, 2023, **88**, e202300044.
175 J. C. Knight, S. Therese and A. Manthiram, *J. Mater. Chem. A*, 2015, **3**, 21077–21082.
176 S. Mallick, V. S. K. Choutipalli, S. Bag, V. Subramanian and C. R. Raj, *ACS Appl. Mater. Interfaces*, 2022, **14**, 37577–37586.
177 C. Wang, B.-H. Xiao, J. Huang, K. Xiao and Z. Q. Liu, *Adv. Funct. Mater.*, 2024, **34**, 2405680.
178 J. Yuan, W. Xi, Y. Qiao, Y. Zhou, Y. Ruan, H. Xu, Y. Li, J. He, G. He and H. Chen, *J. Electroanal. Chem.*, 2024, **974**, 118703.
179 S. Saadi-motaallegh, M. Javanbakht, H. Omidvar and S. Habibzadeh, *J. Alloys Compd.*, 2023, **963**, 171119.
180 L. Qin, Q. Zhu, L. Li, G. Fang, S. Li, H. Cheng, W. Guo and H. Gao, *Ionics*, 2021, **27**, 4783–4792.
181 Y. Katsuyama, C. Ooka, R. Zhu, R. Iimura, M. Matsui, R. B. Kaner, I. Honma and H. Kobayashi, *Adv. Funct. Mater.*, 2024, **34**, 2405551.
182 Y. Wang, Z. Wang, W. K. Pang, W. Lie, J. A. Yuwono, G. Liang, S. Liu, A. M. D. Angelo, J. Deng, Y. Fan, K. Davey, B. Li and Z. Guo, *Nat. Commun.*, 2023, **14**, 2720.

183 K. Cai, S.-h. Luo, J. Cong, K. Li, S.-x. Yan, P.-q. Hou, Q. Wang, Y. Zhang, X. Liu and X. Lei, *J. Electrochem. Soc.*, 2022, **169**, 030531.
184 C. Yang, M. Han, H. Yan, F. Li, M. Shi and L. Zhao, *J. Power Sources*, 2020, **452**, 227826.
185 H. Jia, Y. Li, U. Ali, Y. Li, Y. Hao, B. Liu, C. Wang, L. Li and H.-g. Wang, *Appl. Surf. Sci.*, 2022, **592**, 153279.
186 S. Saadi-motaallegh, M. Javanbakht, H. Omidvar and S. Habibzadeh, *J. Alloys Compd.*, 2022, **914**, 165249.
187 S. Yang, M. Zhang, X. Wu, X. Wu, F. Zeng, Y. Li, S. Duan, D. Fan, Y. Yang and X. Wu, *J. Electroanal. Chem.*, 2019, **832**, 69–74.
188 P. Molaiyan, M. Abdollahifar, B. Boz, A. Beutl, M. Krammer, N. Zhang, A. Tron, M. Romio, M. Ricci, R. Adelung, A. Kwade, U. Lassi and A. Paolella, *Adv. Funct. Mater.*, 2024, **34**, 2311301.
189 M. Abdollahifar, *Carbon*, 2025, 119914.
190 J. Offermann, A. Paolella, R. Adelung and M. Abdollahifar, *Chem. Eng. J.*, 2024, **502**, 157920.